



저작자표시-비영리-변경금지 2.0 대한민국

이용자는 아래의 조건을 따르는 경우에 한하여 자유롭게

- 이 저작물을 복제, 배포, 전송, 전시, 공연 및 방송할 수 있습니다.

다음과 같은 조건을 따라야 합니다:



저작자표시. 귀하는 원저작자를 표시하여야 합니다.



비영리. 귀하는 이 저작물을 영리 목적으로 이용할 수 없습니다.



변경금지. 귀하는 이 저작물을 개작, 변형 또는 가공할 수 없습니다.

- 귀하는, 이 저작물의 재이용이나 배포의 경우, 이 저작물에 적용된 이용허락조건을 명확하게 나타내어야 합니다.
- 저작권자로부터 별도의 허가를 받으면 이러한 조건들은 적용되지 않습니다.

저작권법에 따른 이용자의 권리는 위의 내용에 의하여 영향을 받지 않습니다.

이것은 [이용허락규약\(Legal Code\)](#)을 이해하기 쉽게 요약한 것입니다.

[Disclaimer](#)

공학박사 학위논문

**Low temperature NO adsorption over
Pd-based catalysts for
cold start application**

냉시동 적용을 위한 Pd 기반 촉매의 저온
NO흡장 능력

2018년 8월

서울대학교 대학원

화학생물공학부

유영석

Abstract

Low temperature NO adsorption over Pd-based catalysts for cold start application

Youngseok Ryou

School of Chemical and Biological Engineering

The Graduate School

Seoul National University

The abatement of NO_x arising from automobiles becomes an important societal problem due to detrimental effect on human health and environment. Therefore, global regulations on NO_x emission have been continuously issued and reinforced. To fulfill the legislations, various NO_x reduction technologies such as three-way catalysis (TWC), selective catalytic reduction (SCR), and NO_x storage reduction (NSR) systems have been successfully developed and applied. Among them, SCR and NSR have been adapted to address NO_x emission in diesel engines. However, both systems require high temperature (above 200 °C) to acquire proper NO_x reduction efficiency. Recently, in order to control the NO_x emission during cold start, low temperature NO adsorption materials, namely, cold start catalysts (CSC) or passive NO_x adsorbers (PNA)

having the ability of storing NO_x at low temperature and releasing them at high temperature where SCR and NSR properly operate draw significant attention.

To have proper function as the low temperature NO adsorption catalyst, it must have not only catalytic ability (such as high NO storage capacity and proper NO_x desorption temperature) but also durability under diesel exhaust conditions. In this work, various materials such as PGM(active metal), metal-oxide and zeolite(support) were investigated to identify the possibility for the low temperature NO adsorption catalyst. Especially, to evaluate the potential for the practical application of catalyst, exhaust gas conditions (such as hydrothermal aging and sulfur aging) causing catalytic deactivation were applied.

At first, hydrothermally aged Pd/CeO₂ was employed for NO adsorption at low temperature (80 – 160 °C). For comparison, Pt or Pt-Pd supported on CeO₂ or Al₂O₃ catalysts were also evaluated. Analysis of the hydrothermally aged catalysts clearly demonstrate that Pt and/or Pd on CeO₂ is more resistant to sintering than that on Al₂O₃ support. NO adsorption/desorption results indicate that CeO₂-based catalysts have superior NO adsorption ability than Al₂O₃-based catalysts. In addition, PGM/CeO₂ catalysts exhibit the desirable desorption temperature for cold start application. DRIFT spectra of adsorbed NO_x species on Pd/CeO₂ during NO adsorption/desorption demonstrate that NO_x desorption peaks at 250, 300, and 450 °C derive from weakly bound nitrite, nitro-nitrito species, and nitrate species, respectively. Based on the activity test and

characterization, it can be mentioned that Pd in Pd/CeO₂ plays an important role in generating additional NO adsorption site arising from the interaction between Pd and CeO₂ and helping the oxidation from adsorbed nitrite to nitrate. Therefore, Pd/CeO₂ can be a good candidate as low temperature NO adsorption catalyst for cold start application.

Next, to investigate the effect of sulfur aging (SA) and regeneration (DeSO_x) on the changes in NO adsorption ability and physicochemical properties of catalysts, both treatments were applied to Pd/CeO₂ and Pd/Ce_{0.58}Zr_{0.42}O₂ (Pd/Ce58) catalysts. SA treatment on both catalysts leads to the negligible NO adsorption ability since it gives rise to form thermodynamically more stable Ce(SO₄)₂ than adsorbed NO_x species. Structural and textural analysis after regeneration treatment exhibits that Pd/Ce58 maintains the crystalline size with similar pore size distribution, while Pd/CeO₂ does not. In addition, the former sample recovers its own Pd distribution after regeneration, although the latter does not. However, the fact that both regenerated catalysts do not restore the NO adsorption ability to the level of HTA ones indicates that either textural property or Pd dispersion cannot account for the deterioration of NO adsorption ability after sulfur aging and regeneration. Instead, H₂-TPR analysis on both samples indicates that the intimate interaction between Pd and ceria is disappear after regeneration, as proved by the absence of the simultaneous reduction of CeO₂ and PdO below 20 °C. Hence, it can be concluded that the sulfur aging and the subsequent regeneration has negative effect on the interaction between

PdO and CeO₂, resulting in the irreversible degradation in the NO adsorption ability at low temperature. This result implies that the application of Pd/Ce-based catalyst to practical condition is difficult.

To obtain the hydrothermal stability and sulfur resistance, zeolite-based catalyst was employed. Fresh Pd/SSZ-13 did not possess good NO adsorption capacity irrespective of the preparation methods such as incipient wetness impregnation, wet impregnation, ion-exchange, and solid state ion exchange. However, after hydrothermal aging (HTA) treatment, Pd/SSZ-13 could obtain enhanced NO adsorption ability at low temperature, which will be suitable for the application of cold start catalyst. H₂-TPR and XAFS results clearly indicate that PdO mainly existed over the fresh sample, while HTA treated sample contained ionic Pd species, demonstrating the redistribution of PdO into highly dispersed ionic Pd species within the SSZ-13 structure arising from HTA treatment. DRIFT results display the formation of two nitrosyl complexes adsorbed on Pd²⁺ ions, which are directly related to two desorption peaks of NO_x at 250 and 400 °C. All combined results provide the unambiguous evidence about the generation of Pd ions in SSZ-13 zeolite induced by HTA treatment, which play as the active sites for NO adsorption at low temperature.

Keywords: Low temperature NO adsorption, Pd, CeO₂, SSZ-13, hydrothermal aging, sulfur aging, cold start

Student Number: 2014-31091

Contents

Abstract.....	i
List of Tables	viii
List of Figures	ix
Chapter 1. Introduction	1
1.1. Diesel vehicle exhaust and exhaust gas purification system.....	1
1.2. Cold start catalyst for low temperature NO adsorption	4
1.3. Objectives.....	7
Chapter 2. Low temperature NO adsorption ability over hydrothermally aged PGM/metal-oxide catalysts for cold start application	9
2.1. Introduction	9
2.2. Experimental.....	12
2.2.1. Catalysts preparation	12
2.2.2. Catalyst characterizations	12
2.2.3. Activity measurement for the adsorption/desorption of NO	14
2.3. Result & discussion.....	16
2.3.1. Structural properties and CO-chemisorption	16
2.3.2. Low temperature NO adsorption	21
2.3.2.1. Adsorption/desorption of NO on various catalysts	21
2.3.2.2. Effect of adsorption time on the adsorption/desorption of NO on Pd/CeO₂	30
2.3.2.3. Effect of gas mixture on the adsorption/desorption of NO on Pd/CeO₂	33
2.3.3. DRIFT results during the adsorption/desorption of NO on Pd/CeO₂	36
Chapter 3. Effect of sulfur poisoning and regeneration on NO adsorption ability over Pd/Ce-based catalysts.....	44
3.1. Introduction	44
3.2. Experimental.....	46

3.2.1. Catalysts preparation	46
3.2.2. Catalysts characterizations	47
3.2.2. NO adsorption/desorption activity	49
3.3. Result & discussion.....	50
3.3.1. Low temperature NO adsorption/desorption activity of Pd/CeO ₂ and Pd/Ce58.....	50
3.3.2. Characterization of Pd/CeO ₂ and Pd/Ce58 with various treatments .	58
3.3.2.1. XPS and FTIR analysis	58
3.3.2.2. XRD and BET	62
3.3.2.3. CO-chemisorption and H ₂ -TPR	67
Chapter 4. Activation of Pd/SSZ-13 by hydrothermal aging treatment for low temperature NO adsorption.....	73
4.1. Introduction	73
4.2. Experimental.....	76
4.2.1. Catalysts preparation	76
4.2.2. Catalysts characterizations	77
4.2.3. NO adsorption activity	80
4.3. Results.....	82
4.3.1. Low temperature NO adsorption over various Pd/SSZ-13 catalysts .	82
4.3.2. XRD and NMR	89
4.3.3. H ₂ -TPR and XPS	94
4.3.4. XAFS and STEM	99
4.3.5. DRIFT result during NO adsorption/desorption of HTA Pd(2)/SSZ-13	106
4.3.6. CO-DRIFT results for fresh and HTA samples.....	109
4.3.7. Sulfur aging effect on NO adsorption ability over HTA Pd/SSZ-13 ..	111
4.4. Discussion	114
4.4.1. The change in Pd species during HTA treatment.....	114

4.4.2. The effect of Pd ion exchange methods on the physicochemical state of Pd/SSZ-13	116
4.4.3. The limit of Pd ion exchange in SSZ-13 by HTA treatment	118
4.4.4. The effect of hydrothermal treatment on Pd/SSZ-13	121
Summary and Conclusions	124
Bibliography	127
국 문 초 록	136

List of Tables

Table 2-1. The average particle size of PGM and the N ₂ physisorption results of various catalysts.	20
Table 2-2. NO _x storage capacity of various catalysts measured by NO adsorption/desorption.	28
Table 3-1. Sulfur amount, structural and textural properties, and Pd dispersion of HTA, SA and DeSO _x samples.	57
Table 4-1. Pd loadings (as synthesis) and NO adsorption capacity (after HTA) of Pd/SSZ-13 catalysts measured by ICP and NO adsorption/desorption experiment, respectively.	85
Table 4-2. Results of curve fit of EXAFS data for Pd/SSZ-13 collected at Pd <i>K</i> edge.	104

List of Figures

Figure 1-1. EPA and EU nonroad emissions regulations: 37 – 560 kW (50 – 750 hp) [43].	3
Figure 1-2. Cumulative THC and NO _x tailpipe emissions over bag 1 of the FTP75 chassis dynamometer drive cycle for the Ford Expedition with the EXP3 exhaust system, retarded spark timing at cold-start conditions, modified EGR control and OEM cast exhaust manifolds [53].	6
Figure 1-3. The function of cold start NO _x adsorption catalyst.	6
Figure 2-1. The scheme of NO adsorption/desorption process. 9.5 % O ₂ , 5 % H ₂ O, and 5 % CO ₂ always exist in all steps.	15
Figure 2-2. XRD patterns of various CeO ₂ supported catalysts: (a) fresh and (b) HTA.	18
Figure 2-3. XRD patterns of various Al ₂ O ₃ supported catalysts: (a) fresh and (b) HTA.	19
Figure 2-4. NO _x concentration and amount (insertion, μmol) of NO adsorption/desorption experiment with or without catalyst. *Blank: the measurement of NO pulse without catalyst, Bypass: Unadsorbed NO _x amount in the presence of catalyst, TPD: NO _x concentration during desorption process.	25
Figure 2-5. NO, NO ₂ , and NO _x desorption curves of HTA Pd/CeO ₂ catalyst. (NO adsorption temperature: 80 °C, ramping rate: 10 °C/min).	26
Figure 2-6. NO _x desorption curve of HTA CeO ₂ support and Pt, Pt-Pd, and Pd supported on CeO ₂ catalysts.	27
Figure 2-7. NO _x desorption curve of HTA Pd, Pt-Pd, Pt/Al ₂ O ₃ and Pd/CeO ₂ catalyst.	29
Figure 2-8. (a) NO _x and (b) NO ₂ desorption curves of HTA Pd/CeO ₂ with the NO adsorption time for 50, 100, 200, 500 sec, 1 and 3 hr.	32
Figure 2-9. NO _x desorption curves of HTA Pd/CeO ₂ catalyst under various gas mixture: O ₂ + H ₂ O + CO ₂ (standard), O ₂ + H ₂ O, O ₂ + CO ₂ , and only O ₂ .	35

Figure 2-10. DRIFT spectra during NO+O ₂ +H ₂ O adsorption as a function of adsorption time (min) over HTA Pd/CeO ₂ in the range of (a) 1800 – 800 and (b) 3800 – 3000 cm ⁻¹	42
Figure 2-11. DRIFT spectra during desorption as a function of temperature (°C) over HTA Pd/CeO ₂ with the range of 1800 – 800 cm ⁻¹	43
Figure 3-1. NO _x desorption curves of HTA, SA and DeSO _x (a) Pd/CeO ₂ and (b) Pd/Ce58 catalysts with HTA CeO ₂	54
Figure 3-2. Evolution of NO and SO ₂ after the introduction of SO ₂ to NO pre-adsorbed on HTA Pd/CeO ₂ at 300 °C.....	55
Figure 3-3. SO ₂ -TPD of SA Pd/CeO ₂ and Pd/Ce58 catalysts.	56
Figure 3-4. Pd 3d XPS spectra of HTA, SA, and DeSO _x Pd/CeO ₂ catalysts..	60
Figure 3-5. FT-IR spectra of SA and DeSO _x Pd/CeO ₂ and Pd/Ce58 in the range of 3000 – 950 cm ⁻¹ . Ce(SO ₄) ₂ is shown as a reference.	61
Figure 3-6. XRD patterns of HTA, SA and DeSO _x (a) Pd/CeO ₂ and (b) Pd/Ce58 catalysts.	65
Figure 3-7. Pore size distribution of HTA, SA, and DeSO _x (a) Pd/CeO ₂ and (b) Pd/Ce58 catalysts.	66
Figure 3-8. H ₂ -TPR spectra of HTA and DeSO _x (a) Pd/CeO ₂ and (b) Pd/Ce58 with HTA CeO ₂	72
Figure 4-1. NO _x desorption curves of fresh and HTA Pd(2)/SSZ-13 IWI, WET, S-S, and ION catalysts. NO adsorption temperature = 120 °C, ramping rate = 10 °C/min.	86
Figure 4-2. NO, NO ₂ and NO _x concentration of HTA Pd(2)/SSZ-13 IWI during desorption.....	87
Figure 4-3. NO _x desorption (a) curves and (b) amount of Pd/SSZ-13 IWI catalyst (HTA) with various Pd loading.	88
Figure 4-4. XRD patterns of fresh and HTA Pd(2)/SSZ-13 IWI catalysts.	91
Figure 4-5. XRD patterns in the region of PdO of (a) fresh and (b) HTA Pd/SSZ-13 IWI catalyst with various Pd loading.	92
Figure 4-6. Solid-state ²⁷ Al-NMR spectra of fresh and HTA H-SSZ-13, and HTA Pd(1)/SSZ-13 IWI.....	93

Figure 4-7. H ₂ -TPR spectra of fresh and HTA Pd/SSZ-13 IWI catalysts.....	97
Figure 4-8. Difference of the amount of PdO reduced at around 0 °C between fresh and HTA samples calculated by H ₂ -TPR of Pd/SSZ-13 IWI catalyst.....	98
Figure 4-9. Pd <i>K</i> edge XANES of fresh and HTA Pd(0.5, 2, and 5)/SSZ-13 catalysts in addition to Pd foil and PdO.	102
Figure 4-10. Fourier transforms of <i>k</i> ³ -weighted Pd <i>K</i> edge EXAFS for Pd metal, PdO, and Pd/SSZ-13 IWI with different Pd loadings.....	103
Figure 4-11. (Left) EDS mapping analysis for Pd and (Right) Z-contrast STEM image of (a) fresh and (b) HTA Pd(1)/SSZ-13 IWI.	105
Figure 4-12. DRIFT spectra during NO (a) adsorption as a function of time (min) and (b) desorption as a function of temperature (°C) over HTA Pd(2)/SSZ-13 IWI.....	108
Figure 4-13. CO-DRIFT spectra for the (a) fresh and (b) HTA samples.....	110
Figure 4-14. NO _x desorption curves HTA Pd/SSZ-13 after sulfur aging and regeneration treatment.	113
Figure 4-15. NO _x desorption curves of HTA Pd(2)/SSZ-13 IWI with different NO adsorption time: 100 sec for cold start NO adsorption (black) and 1 hr for Pd ion titration (red).	120
Figure 4-16. Schematic model to represent the change in the nature of Pd (a) before and (b) after HTA treatment.	123

Chapter 1. Introduction

1.1. Diesel vehicle exhaust and exhaust gas purification system

In modern society, industrial development has required considerable dependence on internal combustion engines (IC). Especially, diesel engines which have advantages of efficiency, economy and durability have attracted significant attention due to new regulations on fuel economy [1-7]. However diesel engines release a variety of hazardous gases including carbon monoxide (CO), hydrocarbons (HCs), nitrogen oxides (NO_x) and particulate matter (PM) to the atmosphere [8-10]. Those emissions are heavy causes of environmental pollution and human diseases [11-16]. In order to reduce pollutant, emission regulations have been globally issued and reinforced [17-21]. Exhaust gas purification system adopting catalytic converter is one of the most promising method to eliminate pollutants in the exhaust gas. For example, in gasoline engine, three-way catalyst oxidizes CO and HCs to CO₂ and H₂O and reduces NO_x to N₂ simultaneously under specific air-to-fuel ratio (14.5) [22-25]. However, since the condition of diesel engine is lean (i.e. oxidative condition), it is difficult to reduce NO_x due to the abundant oxygen condition. [10, 26].

In order to purify harmful components of diesel exhaust, multiple catalysts were applied. The typical purification system for diesel vehicle consists of diesel oxidation catalyst (DOC), diesel particulate filter (DPF), and NO_x reduction catalyst such as selective catalytic reduction (SCR) and NO_x storage

reduction (NSR) [1, 27]. The main role of DOC which is located in the front of catalytic converter is the oxidation of CO and unburned HCs to CO₂ and H₂O [11, 28-30], and converts extra fuel to heat energy for the regeneration of DPF [31]. Furthermore, DOC oxidizes NO to NO₂ to help SCR performance [18]. The platinum group metal (PGM) is commonly used as an active site for oxidation. Pt-based catalysts are mostly adopted as DOC due to their high oxidation ability [32]. However, Pt is easily sintered in the high temperature condition of diesel exhaust, leading to the deactivation of its oxidation ability. [1, 33]. Although, Pd, another PGM, has lower oxidation activity, it is more thermally stable than Pt. [34-36]. In this regard, Pt-Pd bimetallic catalysts have been studied continuously to improve physicochemical properties of DOC. [26, 33]. Support material is also important to achieve proper catalytic activity. In DOC, Al₂O₃ [25, 26, 34] and SiO₂ [26, 37] are commonly employed because of its high surface area and stability. Particulate matter is filtered by DPF and it is burned and converted to harmless species during the DPF regeneration process [38]. In the case of NO_x species, NH₃-SCR catalysts are mainly applied to reduce NO_x to N₂. There are two types of NH₃-SCR catalysts. One is V-based catalysis, the other is zeolite-based one. However, since V-based catalysts such as V/TiO₂ are readily deactivated by high temperature in the diesel emission, it is mainly applied to plant and ship [39, 40]. On the other hand, zeolite-based SCR catalyst such as Cu-SSZ-13 has high thermal stability [41, 42]. Therefore, it is widely used as a SCR catalyst to reduce NO_x in diesel exhaust.

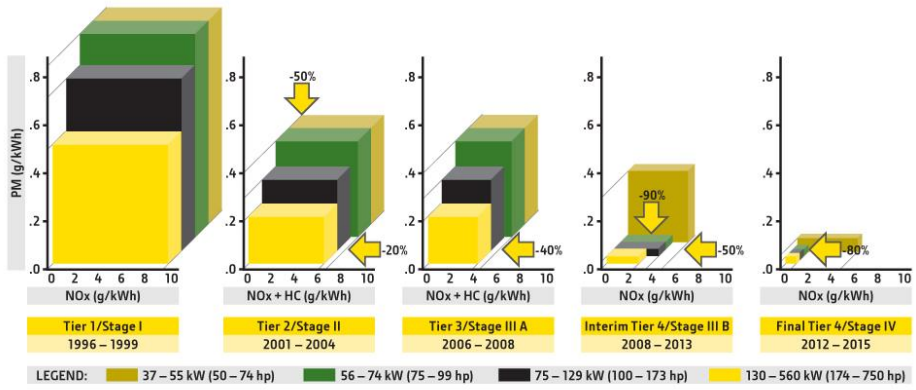


Figure 1-1. EPA and EU nonroad emissions regulations: 37 – 560 kW (50 – 750 hp) [43].

1.2. Cold start catalyst for low temperature NO adsorption

As the stringent regulations on NO_x emission are continuously issued and enforced, the reduction of NO_x in exhaust from diesel engine is considered as a great challenge. In order to reduce NO_x in exhaust gas of lean-burn engine, SCR or NSR system have been adopted for several decades. However, NO_x reduction catalyst systems cannot efficiently operate below 200 °C. For example, in SCR system, urea solution starts to decompose at above 180 °C to provide NH₃, which remains one of the crucial obstacles for low temperature NO_x reduction. As a result, during cold start period (initial ca. 100 –200 sec of engine operation), a significant amount of NO_x is released in to air without any catalytic purification [44]. Therefore, NO_x emission during cold start period must be controlled to satisfy the stringent legislation.

Recently, in order to control the NO_x emission during cold start, low temperature NO adsorption materials, namely, cold start catalysts (CSC) or passive NO_x adsorbers (PNA) having the function of storing NO_x at low temperature and releasing them at higher temperature, where SCR and NSR properly operates attract significant attention. In previous literature, it is reported that PGM/metal oxide catalysts have considerable NO_x adsorption ability at low temperature (80 – 120 °C) [45, 46]. In addition, several industrial groups have also reported about catalysts for low temperature NO adsorption. A TWC catalyst including Pd/zeolite as a NO_x storage material was investigated by Honda. [47]. Ford investigated and reported various reaction conditions

containing hydrocarbons and H₂O influencing the low temperature NO_x adsorption of PGM catalysts [48]. Johnson Matthey reported a diesel Cold Start Concept (CSCTM) catalyst that has the ability of storing NO_x and HCs at cold start region and oxidizing CO, NO, and HCs after warming up [44]. Moreover, Johnson Matthey also reported that Pd loaded zeolites (such as BEA, MFI, and CHA) has the ability to trap NO_x at low temperature [49]. Recent patents by Johnson Matthey have claimed a cold start concept catalyst containing PGM supported on metal oxide and zeolite [50-52]. In order to achieve the purpose, such cold start catalysts require two important functions, which are large NO_x storage capacity during cold start and proper NO_x desorption temperature. In particular, the most desirable NO_x releasing temperature must be placed within the operating temperature of SCR or NSR.

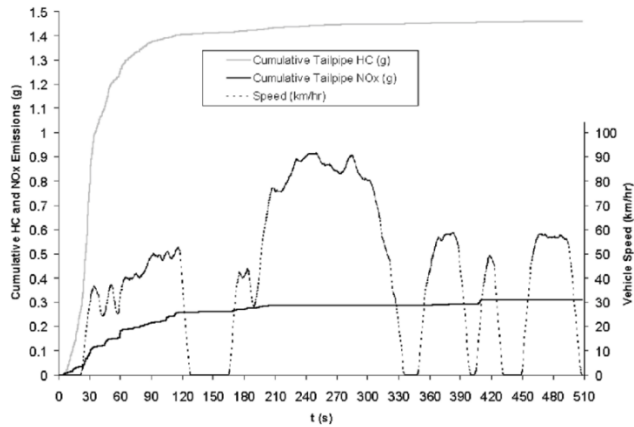


Figure 1-2. Cumulative THC and NOx tailpipe emissions over bag 1 of the FTP75 chassis dynamometer drive cycle for the Ford Expedition with the EXP3 exhaust system, retarded spark timing at cold-start conditions, modified EGR control and OEM cast exhaust manifolds [53].



Figure 1-3. The function of cold start NOx adsorption catalyst.

1.3. Objectives

As regulations on NO_x emission have been reinforced, it is necessary to apply cold start catalyst (CSC, i.e. low temperature NO adsorption catalyst) into exhaust purification system. However, except for its catalytic functions such as NO adsorption and desorption, catalyst for diesel engine should have some differentiated properties due to diesel exhaust condition. First, since the position of catalyst, especially, CSC is close to the engine, catalyst usually undergo severe hydrothermal environment causing the deterioration of catalyst. Also, sulfur species in the fuel and lubricant oil lead to the deactivation of catalysts. Therefore, hydrothermal stability and sulfur resistance are required to adopt CSC to diesel after-treatment system.

In this respect, this thesis mainly consists of investigating materials having potential for the low temperature NO adsorption catalyst and its stability under hydrothermal and sulfur aging condition. In Chapter 2, in order to find out proper catalyst in terms of low temperature NO adsorption ability, various combinations between PGMs and metal oxide supports were evaluated. In addition, NO adsorption/desorption active site and mechanism of the optimum catalyst was investigated after hydrothermal aging process. Based on the result in Chapter 2, sulfur aging and regeneration effect on the metal oxide-based catalysts were examined. Especially, to identify the deactivation mechanism of catalyst resulting from sulfur aging, characterizations on sulfur aged and regenerated catalysts were focused in Chapter 3. In Chapter 4, to overcome the

deactivation of catalyst by sulfur aging, zeolite-based catalyst was introduced. In particularly, ion exchange method of PGM/zeolite catalyst was proposed for granting proper low temperature NO adsorption ability.

Chapter 2. Low temperature NO adsorption ability over hydrothermally aged PGM/metal-oxide catalysts for cold start application

2.1. Introduction

The purification of NO_x component in diesel exhaust gas is crucial to fulfill the present and future stringent legislation. Currently, NO_x storage reduction (NSR) or selective catalytic reduction (SCR) is mainly applied to control the NO_x in diesel emission. When the NO_x treatment systems reach the proper operating temperature (> 200 °C), NO_x species in exhaust is effectively reduced by these NO_x reduction technologies. However, below 200 °C, in other words, during cold start period (initial ca. 100 sec of engine operation), a significant amount of untreated NO_x is emitted to the atmosphere [44]. To address the NO_x emission during cold start, one strategy attracts considerable attention with the concept of storing NO_x during cold start period and desorbing them at elevated temperature where NO_x reduction catalyst (NSR or SCR) operates.

The platinum group metal (PGM) has been used as an active phase of catalysts. Pt, a PGM, is an essential component of TWC, DOC, and NSR due to its high oxidation ability [54-56]. However, Pt is readily deactivated under a high temperature atmosphere because of sintering, and this has motivated efforts to find substitutes. Thus, Pd, which has better resistance to thermal degradation and lower price than Pt, has been intensively studied as a

replacement of Pt. For example, Pt-Pd bimetallic catalysts also have been investigated to facilitate the synergistic effect of two PGMs [33, 55, 57]. It has been reported that both Pt and Pd metals are able to adsorb NO_x molecules at low temperature [49, 58-60]. Especially, it is known that the oxidation state of Pd plays a key role in NO adsorption, as evidenced by the fact that various ionic and metallic Pd species such as Pd²⁺, Pd⁺, and Pd⁰ can adsorb NO at low temperature, although PdO cannot [61, 62]. In the case of Pt, metallic Pt can adsorb NO_x [58].

Due to its relatively large specific surface area and superior thermal stability, Al₂O₃ has been applied as a support material in numerous reactions such as CO oxidation [63] and HCs oxidation [64, 65]. In addition, previous literature shows that Pt/Al₂O₃ has the ability of storing NO_x at low temperature [45]. CeO₂-based materials have been extensively investigated for the various application because of its excellent activity of alternating its oxidative state between Ce³⁺ and Ce⁴⁺ rather easily to store and release oxygen. [66-68]. Furthermore, CeO₂ is well known as a low temperature NO adsorption material [69, 70], and, accordingly, Ce-based materials have been widely applied to NO_x reduction catalysts such as NSR and SCR [71-73].

In this chapter, we evaluated the intrinsic low temperature NO adsorption ability of Pd/CeO₂ compared with Pt, Pt-Pd supported on CeO₂, and Al₂O₃ catalysts after hydrothermal aging in order to use it as a NO_x trap catalyst for cold start application. The NO_x adsorption/desorption behavior was extensively investigated as a function of various parameters such as catalyst,

adsorption time, and reactants. The combined activity and DRIFT results allow us to elucidate the role of PGMs and support, and the adsorption/desorption mechanism over the Pd/CeO₂ catalyst.

2.2. Experimental

2.2.1. Catalysts preparation

CeO₂ and Al₂O₃ support materials were obtained from Rhodia and Sasol, respectively. Three different combinations of Pt and Pd (2:0, 1:1 and 0:2 wt%) were loaded on these supports by the conventional incipient wetness impregnation method with aqueous solutions of Pd (NO₃)₂•2H₂O (Sigma Aldrich) and/or Pt(NH₃)₄(NO₃)₂ (Alfa Aesar) as a metal precursor. After impregnation, all catalysts were dried at 100 °C for 24 hr and calcined at 500 °C in 15% O₂ balanced with N₂ for 2 hr, which were designated as “Fresh”. Since automotive emission control catalyst requires excellent hydrothermal stability, the calcined samples were treated with 15% O₂ and 10% H₂O in N₂ with a total flow rate of 200 ml/min at 750 °C for 25 hr, and were denoted as hydrothermally aged (HTA) samples. We primarily investigated the HTA samples for activity measurement and characterization, if not specified.

2.2.2. Catalyst characterizations

The crystalline phase of the catalysts was analyzed by powder X-ray diffraction (XRD) using a Rigaku (mode 1 smartlab) diffractometer with Cu K α radiation (40 kV and 30 mA). The XRD data were recorded in a range of 10 – 80 ° (2 θ) with a step size of 0.02 ° at a rate of 2.5 °/min.

N₂ physisorption was carried out to measure the BET surface area on a Micromeritics ASAP 2010 at -196 °C (liquid nitrogen temperature). Before measurement, the catalysts were degassed at 250 °C for 4 hr under a vacuum condition.

CO-chemisorption was conducted a BEL-CAT-II (BEL Japan Inc.) with a thermal conductivity detector (TCD). 0.05g of sample was pretreated in 5 % H₂/Ar at 400 °C for 30 min and purged with He for 10 min. After pretreatment, the sample cell was cooled down to -78 °C with He gas and then 5 % CO/He was introduced into reactor using pulse method. We assumed that the adsorption ratio between CO and surface PGM atoms is 1:1 for calculation [74, 75].

DRIFT spectra were collected in the 4000 – 600 cm⁻¹ range with 128 scans at a resolution of 4 cm⁻¹ on a Nicolet 6700 (Thermo Fisher Scientific) equipped with a MCT detector using DRIFT cell (HARRIC praying mantis™). KBr background was collected at 120 °C. Prior to NO adsorption (100 ppm NO, 9.5 % O₂, 5 % H₂O in N₂ balance, 200 ml/min), the samples were pretreated without NO (9.5 % O₂, 5 % H₂O in N₂ balance, 200 ml/min) at 500 °C for 30 min to remove impurities. IR spectra were collected during NO adsorption at 120 °C for 1 hr and also during ramping from 120 to 500 °C under 9.5 % O₂, 5% H₂O, and N₂ with an interval of 50 °C in order to investigate the change in the adsorbed NO_x species on the catalyst during NO_x adsorption/desorption. During the temperature ramping, each spectrum is recorded after stabilization at that temperature for at least 10 min. To extract pure nitrogenous species on catalyst, final IR spectra are obtained by subtracting those of before NO adsorption from

those of after NO adsorption at the same temperature. IR spectra of before NO adsorption are collected with same method during the cool down.

2.2.3. Activity measurement for the adsorption/desorption of NO

An activity test was carried out in a continuous flow quartz reactor. The catalyst (0.1 g) was blended with inert α -Al₂O₃ (0.1 g) to dissipate the heat generated during activity test. The catalyst powder in the reactor was sustained by quartz wool with the same height for each experiment. Before the introduction of gases to the reactor, preheated H₂O (5 %) was continuously injected by a syringe pump at 120 °C to the mixing line. The total flow rate of the inlet stream was 200 ml/min at a gas hourly space velocity (GHSV) of 120,000 h⁻¹. A K-type thermocouple was located on the top of the catalyst bed to measure the temperature of the reactor.

The scheme of NO adsorption/desorption is shown in Figure 2-1. To remove impurities, the catalyst was pre-treated under an oxidative condition with 5% CO₂ and 5% H₂O at 500 °C for 30 min before the activity test. For NO adsorption, 100 ppm NO was introduced for 100 sec at 80 °C with CO₂ (5%), H₂O (5%), and O₂ (9.5%) in N₂ to simulate cold-start NO_x emission. After finishing the NO adsorption procedure, the catalyst was heated with CO₂ (5%), H₂O (5%), and O₂ (9.5%) in N₂ in a range of 80 – 500 °C at a rate of 10 °C/min while the NO_x concentration was measured with a NO_x analyzer (Thermo electron Corp., 42i-HL).

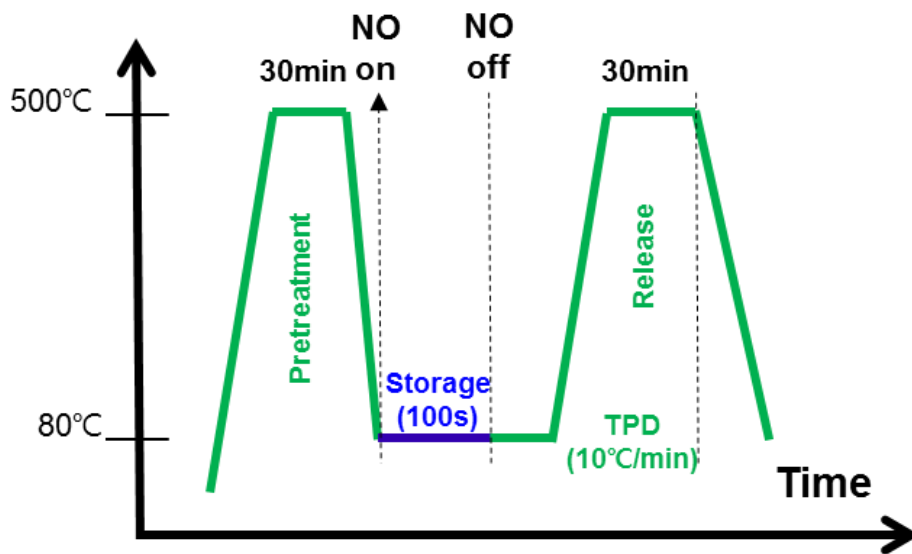


Figure 2-1. The scheme of NO adsorption/desorption process. 9.5 % O₂, 5 % H₂O, and 5 % CO₂ always exist in all steps.

2.3. Result & discussion

2.3.1. Structural properties and CO-chemisorption

XRD patterns of fresh and HTA samples are shown in Figure 2-2. In fresh CeO₂-supported catalysts (Figure 2-2a), the diffraction peaks at 28.5 °, 33.1 °, 47.6 °, and 56.4 ° correspond to the (111), (200), (220), and (311) planes of cubic CeO₂ phase, respectively [76]. After hydrothermal aging, the peaks turn out to be slightly sharper than those of fresh samples, indicating the formation of a more crystalline CeO₂ phase due to sintering. It is interesting to note that no trace of Pt or Pd peaks is observed in any of the fresh and HTA samples, demonstrating that the average crystalline size of Pt and/or Pd species is smaller than the XRD detection limit. Result of CO-chemisorption (Table 2-1) is consistent with the XRD ones. Namely, the dispersions of fresh Pt and Pd on ceria measured by CO-chemisorption are 63 and 41 %, respectively, indicating the presence of small Pt (1.8 nm) and Pd (3.0 nm) particles which are below the detection limit of XRD. In addition, similar to the result of XRD, CO-chemisorption results demonstrate that the change in PGM dispersion is negligible after HTA treatment, which provides the evidence about the well dispersed PGM species on CeO₂ even hydrothermal treatment. Nagai et al. reported that the formation of Pt-O-Ce bond inhibited the sintering of Pt particles during thermal treatment [77]. Therefore, it can be mentioned that similar interaction exists in the Pd and Pt-Pd on ceria, accounting for a good

thermal stability against sintering.

In contrast to CeO₂ supported catalysts, Al₂O₃ supported ones demonstrate different behavior of PGM sintering. As shown in the XRD patterns of Figure 2-3a, all the fresh samples exhibit several peaks assigned to γ -Al₂O₃ phase, although Pd-containing samples demonstrate broad peaks assigned to PdO. However, the hydrothermal treatment on Pt and/or Pd supported on Al₂O₃ catalysts leads to the severe sintering of PGM, as displayed in Figure 2-3b. The diffraction pattern of Pt/Al₂O₃ clearly shows a highly crystalline metallic Pt phase at $2\theta = 39.8^\circ$ (JCPDS 04-0802) with a crystalline size of 23.0 nm. In the case of Pd/Al₂O₃, the main peak of PdO (101) at 33.9° (JCPDS 43-1024) is observed with a crystalline size of 16.4 nm. In contrast to Pt or Pd/Al₂O₃ catalysts, Pt-Pd/Al₂O₃ shows two distinct phases. Since the sharp peak at 40.0° is located between Pt (111) and Pd (111), it can be assigned to PtPd alloy, which is in good agreement with a previous report by Graham et al. [78]. Another noticeable phase is PdO with a crystalline size of 17.6 nm, as evidenced by the peak at 33.9° . Therefore, it can be summarized that the HTA Pt-Pd/Al₂O₃ sample contains two distinct crystalline phases of PdO and PtPd alloy. Comparing the ability of the support to prevent PGM sintering, it can be concluded that the CeO₂ support is superior to Al₂O₃. As presented in Table 2-1, Al₂O₃ supported catalysts have higher surface area than those of CeO₂. After hydrothermal treatment, the surface area of all catalysts decreases to some extent compared with that of the fresh catalysts, whereas the pore volume is almost unchanged.

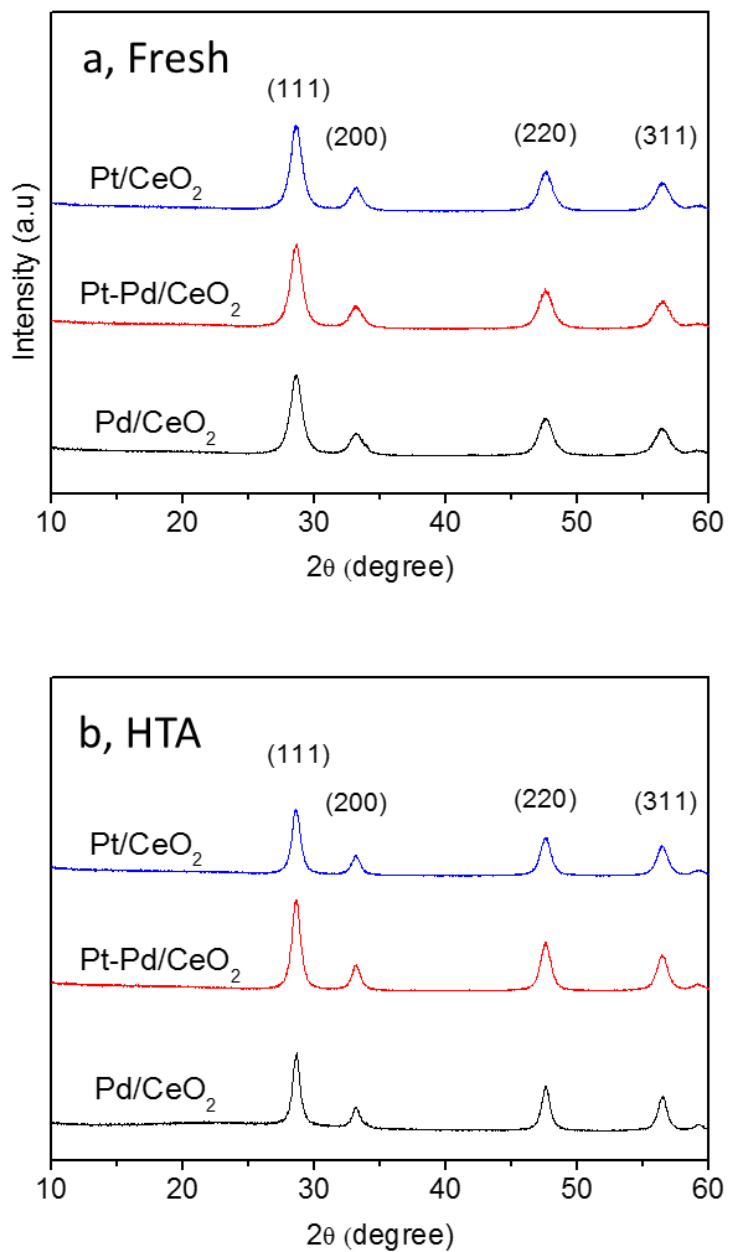


Figure 2-2. XRD patterns of various CeO₂ supported catalysts: (a) fresh and (b) HTA.

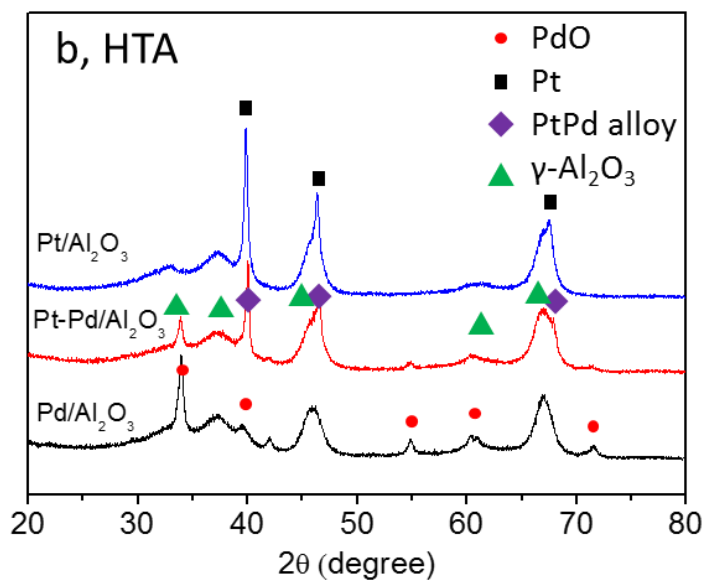
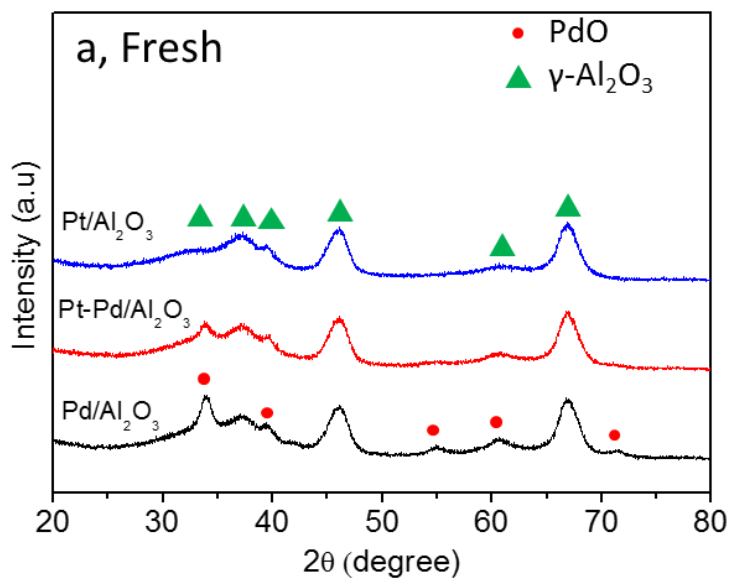


Figure 2-3. XRD patterns of various Al_2O_3 supported catalysts: (a) fresh and (b) HTA.

Table 2-1. The average particle size of PGM and the N₂ physisorption results of various catalysts.

Sample	PGM dispersion ^a (%)		Average particle size (nm)		BET (m ² /g)		Pore volume (cm ³ /g)	
	Fresh	HTA	Fresh	HTA	Fresh	HTA	Fresh	HTA
Pt/CeO ₂	63	65	1.8 ^a	1.5 ^a	125	90	0.27	0.26
Pt-Pd/CeO ₂	-	-	-	-	130	91	0.27	0.26
Pd/CeO ₂	37	41	3.0 ^a	2.7 ^a	124	86	0.27	0.26
Pt/Al ₂ O ₃	-	-	-	23.0 ^b	219	153	0.44	0.40
Pt-Pd/Al ₂ O ₃	-	-	6.7 ^b (PdO)	17.6 ^b (PdO) 26.9 ^b (PtPd alloy)	219	182	0.44	0.41
Pd/Al ₂ O ₃	-	-	7.4	16.4 ^b	199	158	0.40	0.40

a: Determined by CO-chemisorption

b: Determined by XRD

2.3.2. Low temperature NO adsorption

2.3.2.1. Adsorption/desorption of NO on various catalysts

For the calculation of mass balance, Figure 2-4. shows the NO_x concentration during NO adsorption/desorption experiment with or without catalyst. In all the catalysts, it is observed that the NO_x amount of blank test is almost equal to the sum of unadsorbed and desorbed NO_x during NO adsorption/desorption with an error below 2 %. Furthermore, DRIFT results also support the complete removal of the adsorbed NO_x species on catalyst up to 500 °C (in the DRIFT section). Therefore, it can be mentioned that the adsorbed NO_x species on catalyst are wholly desorbed below 500 °C. Note also that the formation of N₂O during NO adsorption/desorption is insignificant, which is confirmed by using the mass balance and DRIFT analysis. Moreover, Theis et al reported the negligible amount of N₂O formation during similar experiment with ours [48]. Therefore, the desorbed NO_x species in this study mainly indicate NO and NO₂.

After adsorption of NO on HTA Pd/CeO₂ sample at 80 °C, the NO_x desorption profile during the temperature ramping from 80 to 500 °C is displayed in Figure 2-5. The NO_x desorption curve clearly shows two desorption peaks (arbitrarily assigned to α and β). The low temperature peak α has a maximum at around 300 °C with a desorption amount of about 5.9 $\mu\text{mol/g}$

cat. in a temperature range of 180 to 370 °C. In addition, one highly symmetric peak centered at ca. 450 °C (β) is shown with smaller intensity (5.5 $\mu\text{mol/g cat.}$) than α . It is worth mentioning that while NO is primarily desorbed from the α peak, NO and NO₂ are from the β peak, which implies that the nature of the two peaks is completely different. Based on the amount of NO_x desorbed, 50% of NO that was introduced to the reactor for 100 sec was eventually stored at 80 °C. As described in the introduction, the desirable desorption temperature of a cold start catalyst must be located within the working temperature of the SCR or NSR. In this regard, Pd/CeO₂ has a valid NO_x desorption temperature window.

In order to identify the origin of active sites for NO adsorption, various catalysts were evaluated. Figure 2-6 shows NO_x desorption curves of the CeO₂ support and CeO₂-supported catalysts with various Pt/Pd ratios after HTA treatment. The amount of NO_x adsorbed over catalysts are listed in Table 2-2. Without PGM metal, the CeO₂ support itself primarily desorbs NO_x at around 220 °C with a small peak at 450 °C. Moreover, the total amount of NO_x desorbed (8.0 $\mu\text{mol/g cat.}$) is smaller than Pd/CeO₂ catalyst (11.4 $\mu\text{mol/g cat.}$). In the case of Pt-containing samples (Pt/CeO₂ and Pt-Pd/CeO₂), the desorption peak is primarily located at a similar position to the β peak of Pd/CeO₂, implying that the combination of PGM (Pd or Pt) and CeO₂ is responsible for the active site for high temperature desorption of NO_x. Note that the intensity of the β peak depends strongly on the speciation of Pt and Pd. Meanwhile, the α peak is exclusively shown in the Pd containing samples. Combined XPS and H₂-TPR analysis results clearly demonstrated that Pd/CeO₂ contains PdO, on

which NO was hardly adsorbed [61, 62]. Watson et al. claimed that the oxidation of Pd to PdO results in steric hindrance of the NO adsorption sites on Pd [61]. Moreover, Ogura et al. shows that PdO on SiO₂ cannot adsorb NO based on NO-TPD results [62]. As such, two individual components (PdO and CeO₂) cannot desorb NO at around 300 °C, strongly suggesting that the active site of the α peak is generated by the close interaction between PdO and CeO₂. Existence of such intimate interactions can be proved by the H₂ spill-over from Pd to CeO₂, as observed in H₂-TPR (It will be discussed in the next chapter.). It can be summarized that since the intensity and temperature of NO_x desorption peaks depend on the speciation of loaded PGM metal, the combination of Pd and Pt on CeO₂ enables the catalyst to control the NO_x desorption. With respect to the amount of NO adsorption, the Pd/CeO₂ catalyst has the highest NO adsorption capacity among the samples under our reaction condition, as presented in Table 2-2.

To obtain more information about the effect of the PGM metal and support on the adsorption/desorption of NO, a series of Al₂O₃ supported catalysts were also evaluated. As can be seen in Fig. 2-7, Pd containing catalysts on Al₂O₃ show NO desorption at around 200 °C, whereas Pt/Al₂O₃ shows negligible amount over the entire temperature range up to 500 °C. In other words, Pd on Al₂O₃ provides adsorption sites for NO adsorption, although Pt does not. In comparison with our results, Ji et al. reported that Pt/Al₂O₃ has the ability to store NO_x at low temperature [45]. This difference in activity originates from the state of the catalyst, since all catalysts in this study were treated severely at

high temperature, which induces significant sintering of Pt in Pt/Al₂O₃, as evidenced by XRD. It is interesting to note that there is a remarkable difference in NO adsorption/desorption between the Al₂O₃ and CeO₂ supports. For comparison, the NO_x desorption curve of Pd/CeO₂ is displayed together with those of Al₂O₃ supported samples in Figure 2-7. The significant difference between Pd/CeO₂ and Pd/Al₂O₃ lies in the high temperature desorption peak (β), which provides strong evidence that the adsorption site of β requires both PdO and CeO₂, as discussed above. Moreover, Pd/Al₂O₃ presents a lower temperature peak than α of Pd/CeO₂, indicating that NO_x adsorbed on Pd/Al₂O₃ is more weakly bonded than that on Pd/CeO₂. Hence, Pd/Al₂O₃ is not suitable for the cold start application.

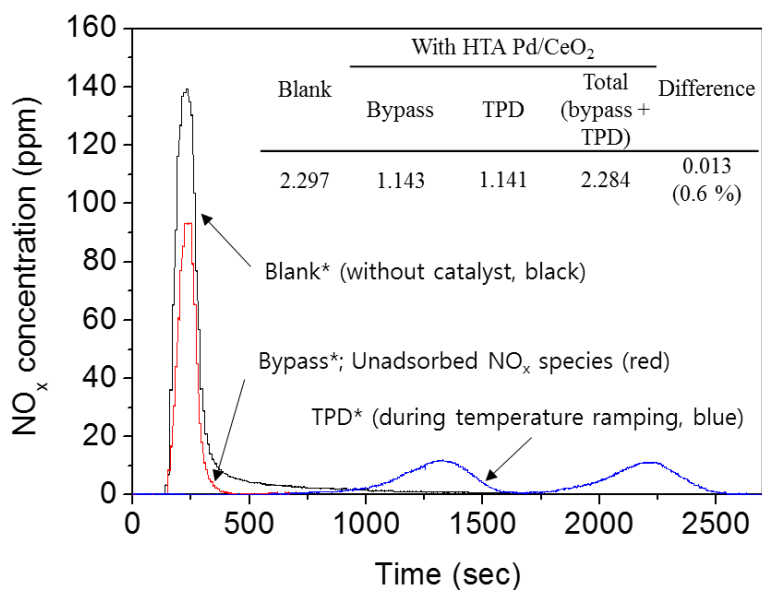


Figure 2-4. NO_x concentration and amount (insertion, μmol) of NO adsorption/desorption experiment with or without catalyst. *Blank: the measurement of NO pulse without catalyst, Bypass: Unadsorbed NO_x amount in the presence of catalyst, TPD: NO_x concentration during desorption process.

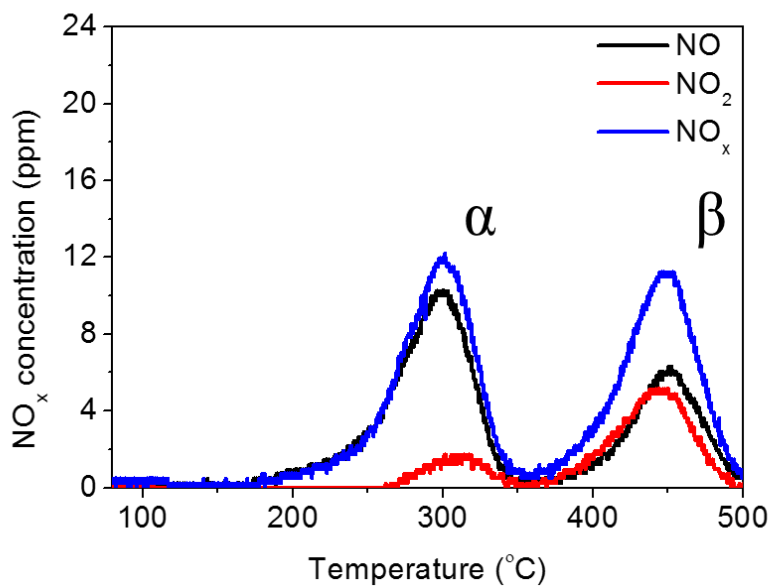


Figure 2-5. NO, NO₂, and NO_x desorption curves of HTA Pd/CeO₂ catalyst. (NO adsorption temperature: 80 °C, ramping rate: 10 °C/min).

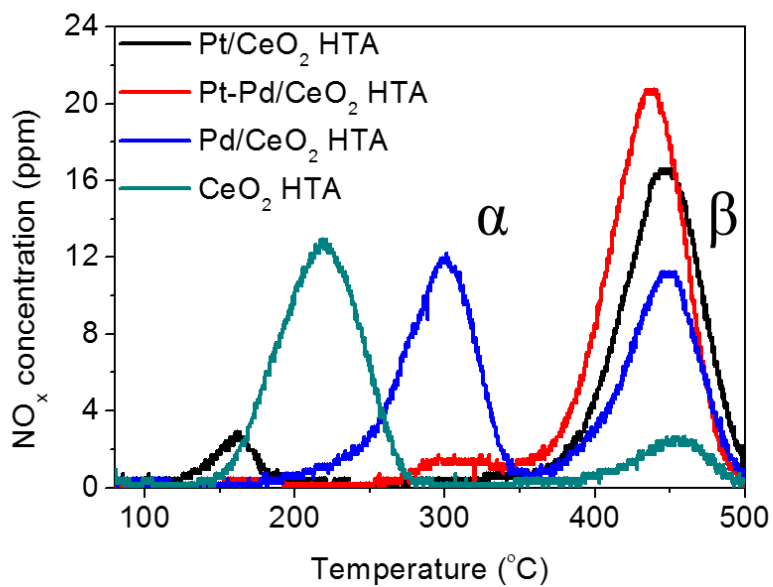


Figure 2-6. NO_x desorption curve of HTA CeO₂ support and Pt, Pt-Pd, and Pd supported on CeO₂ catalysts.

Table 2-2. NO_x storage capacity of various catalysts measured by NO adsorption/desorption.

Catalyst	NO _x storage capacity of HTA catalyst	
	NO _x storage ^a (μmol/g cat.)	NO _x storage ^b (%)
CeO ₂	8.0	34.8
Pt/CeO ₂	9.8	42.6
Pt-Pd/CeO ₂	11.2	49.0
Pd/CeO ₂	11.4	50.0
Pt/Al ₂ O ₃	0.7	3.2
Pt-Pd/Al ₂ O ₃	5.9	25.6
Pd/Al ₂ O ₃	6.8	29.4

a: $\frac{\text{the amount of NOx during TPD } (\mu\text{mol})}{\text{the amount of catalyst using in experiment } (g)}$

b: $\frac{\text{the amount of NOx during TPD } (\mu\text{mol})}{\text{the amount of NOx during blank test } (\mu\text{mol})} \times 100$

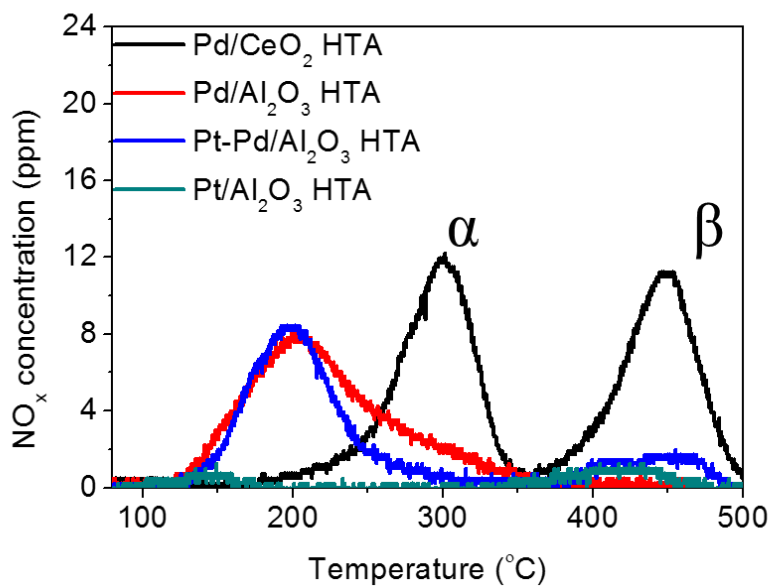


Figure 2-7. NO_x desorption curve of HTA Pd, Pt-Pd, Pt/Al₂O₃ and Pd/CeO₂ catalyst.

2.3.2.2. Effect of adsorption time on the adsorption/desorption of NO on Pd/CeO₂

Since Pd/CeO₂ shows the highest NO_x storage ability as well as desirable desorption temperature, we extensively studied the NO adsorption/desorption behavior of Pd/CeO₂ as a function of various adsorption parameters. Figure 2-8 displays NO_x and NO₂ desorption curves of the Pd/CeO₂ catalyst as a function of NO adsorption time. With increasing NO exposure time, the overall amount of NO adsorbed on the catalyst increases gradually. It is worth mentioning that the rate of peak growth is different between α and β . For the case of shorter NO adsorption time (50 sec), the intensity of the β peak is higher than that of α , indicating the former active sites store NO_x at low temperature more readily than the latter. However, with a further increase in adsorption time (100 – 500 sec), the adsorption amount of the α peak grows proportionally with NO exposure time, whereas the β peak is quickly saturated. This implies that the adsorption capacity of the α peak is larger than that of the β peak, whereas opposite results are found for the storage preference.

When NO adsorption time is longer than an hour, the weakly bound NO_x begins to desorb at low temperature (below 150 °C), which is designated as the α^* peak. Note that NO₂ desorption is observed only at β peak in cases of less than 500 sec of NO adsorption. On the other hand, with an increase of adsorption time beyond 1 hr, the NO_x desorption curves of Pd/CeO₂ exhibit a new NO₂ desorption peak at low temperature (150 – 250 °C), which is identical

to the location of the α^* peak. It can be summarized that the adsorbed NO_x species related to the α^* peak are decomposed to produce NO and NO_2 .

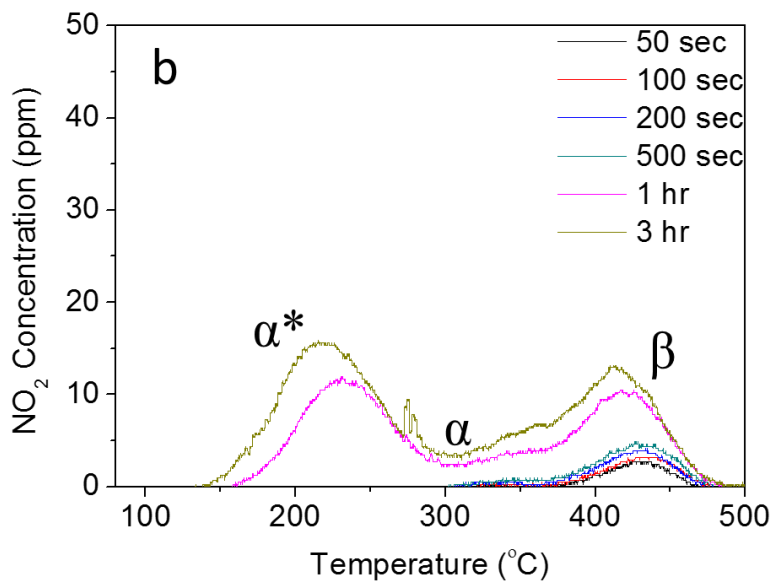
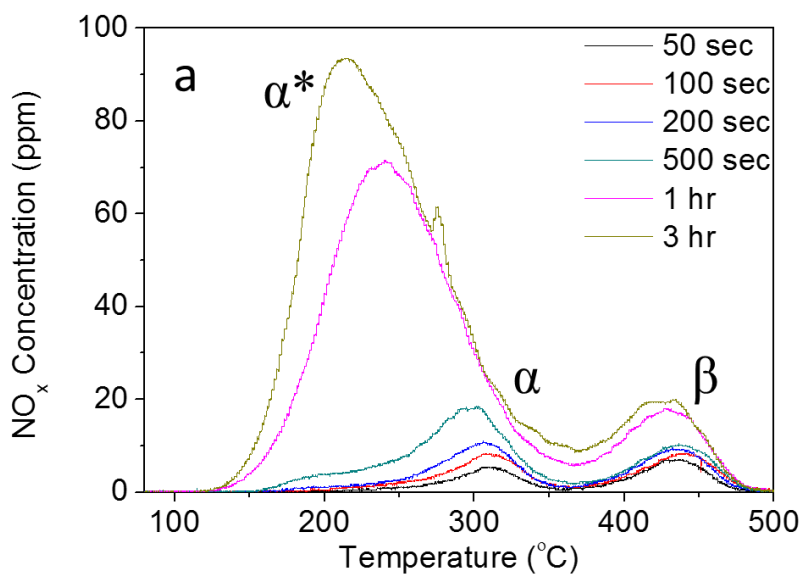


Figure 2-8. (a) NO_x and (b) NO_2 desorption curves of HTA Pd/CeO₂ with the NO adsorption time for 50, 100, 200, 500 sec, 1 and 3 hr.

2.3.2.3. Effect of gas mixture on the adsorption/desorption of NO on Pd/CeO₂

As shown in Figure 2-9, the NO_x adsorption/desorption behavior of Pd/CeO₂ depends heavily on the gas condition. As described earlier, Pd/CeO₂ has two desorption peaks (α and β) at 300 and 450 °C, respectively, when NO is adsorbed with O₂, CO₂, and H₂O. However, the absence of CO₂ in the gas mixture (red) reduces the desorption amount of the α peak. On the other hand, when the catalyst is not exposed to H₂O during NO adsorption/desorption, the intensities of both the α and β peaks increase slightly (blue) in addition to the formation of a small trace of α^* peak. In both cases, the α peak slightly shifts to lower temperature by 10 – 20 °C. Interestingly, when the adsorption/desorption of NO was carried out in the absence of both H₂O and CO₂, the adsorption capacity of the β peak (14.3 $\mu\text{mol/gcat}$) is almost three times higher than that including either CO₂ or H₂O, indicating that the presence of H₂O and CO₂ inhibits the NO adsorption, especially for the β peak. Previous studies reported that PdO and CeO₂ can adsorb H₂O up to 81 and 187 °C, respectively [79, 80]. Moreover, the adsorption of H₂O on the ceria surface at 120 °C was observed in our DRIFT study (which will be shown in the next section), demonstrating that adsorbed H₂O is able to prevent the NO adsorption by preferentially occupying NO adsorption sites of Pd/CeO₂. This also presented that H₂O has an inhibiting effect on NO adsorption at low temperature (below 100 °C) [48]. Similar to H₂O, CO₂ also can adsorb on the surface of

PdO and CeO₂ to form carbonate [81, 82]. However, the stability of the adsorbed CO₂ is quite different depending on the absorbent. CO₂ adsorbed on PdO is readily desorbed below room temperature [81], although the carbonate species on CeO₂ formed by the adsorption of CO₂ is stable up to 377 °C [82]. Since CeO₂ is related to the active sites for α and β peaks, the presence of CO₂ is expected to prevent NO adsorption on both sites. In addition, it must be pointed out that the presence of H₂O and CO₂ leads to a decrease of the desorption temperature of the β peak, implying that the stability of adsorbed NO_x species related to the β peak is significantly influenced by the gaseous environment. Furthermore, in the absence of H₂O and CO₂, the intensity of the α peak is considerably reduced, which might be explained by the preferential adsorption of NO on the active sites of β peak, because it provides energetically stable adsorption sites with larger capacity.

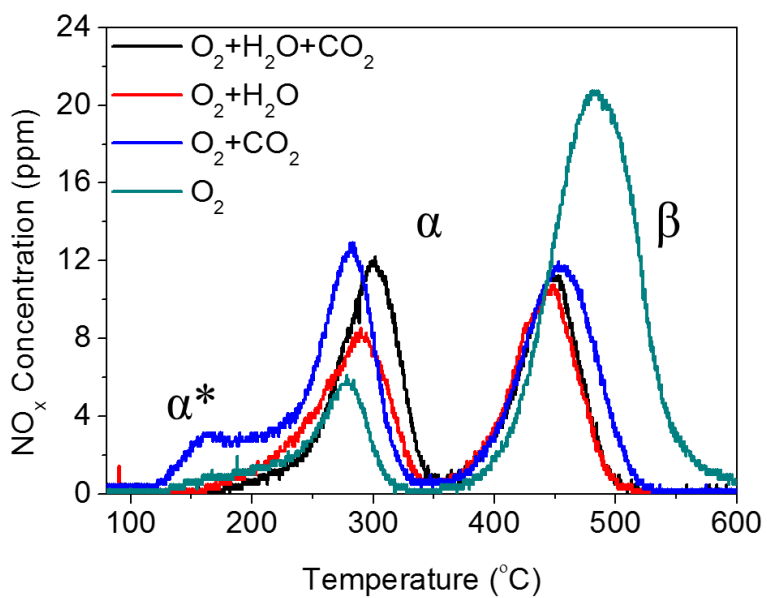


Figure 2-9. NO_x desorption curves of HTA Pd/CeO₂ catalyst under various gas mixture: O₂ + H₂O + CO₂ (standard), O₂ + H₂O, O₂ + CO₂, and only O₂.

2.3.3. DRIFT results during the adsorption/desorption of NO on Pd/CeO₂

Our results clearly exhibit that Pd/CeO₂ has superior NO adsorption ability and proper desorption temperature window based on the NO adsorption/desorption experiment. In order to obtain the comprehensive understanding of the NO adsorption/desorption mechanism and intermediate species on Pd/CeO₂, DRIFT study was performed in a similar manner to our activity measurement: the IR spectrum was obtained during the adsorption of NO with 9.5 % O₂ and 5 % H₂O in N₂ balance at 120 °C, followed by step-wise temperature ramping every 50 °C in a temperature range of 150 – 500 °C. Note that CO₂ is excluded in DRIFT experiments because carbonate species formed on CeO₂ are expected to overlap with nitrate species, which are expected to prevent from identifying the adsorbed NO_x species. Since two NO_x desorption curves (NO+O₂+CO₂+H₂O vs NO+O₂+H₂O) are almost identical except for the slight decrease in the intensity of the α peak over the latter case as shown in Figure 2-9, we think that DRIFT experiment with the NO/O₂ adsorption in the presence of H₂O would provide the valuable information about adsorption/desorption chemistry under the simulated condition.

Figure 2-10a and 10b show the series of DRIFT spectra collected during NO adsorption on Pd/CeO₂ at 120 °C as a function of adsorption time in the range of 1800 – 800 and 3800 – 3000 cm⁻¹, respectively. Up to 30 min of adsorption, the IR spectra exhibit the formation of a various bands at 1475, 1400, 1230, 1040, and 830 cm⁻¹. According to previous literature data [56, 60, 69, 83-85],

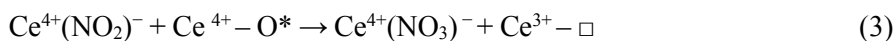
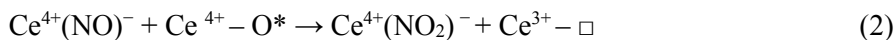
such peaks can be assigned to various nitrogen oxide species such as bridging nitro-nitrito (1475 cm⁻¹), linear nitrite (1415 cm⁻¹), and chelating nitrite (1230, 1040, and 830 cm⁻¹). In addition, the bands of HNO₂ species interacting with H₂O (at 1620 and 1315 cm⁻¹) are also observed, which is accompanied by an abrupt decrease of the surface OH band at 3699 cm⁻¹ and an increase of adsorbed H₂O in the 3600 – 3000 cm⁻¹ region. The changes can be explained by a previous report by Azambre et al. that hydroxyl groups on ceria surface react with adsorbed NO to produce HNO₂ and H₂O in the following reaction [76, 84].



where “Ce⁴⁺ – OH⁻” is the hydroxyl group on the ceria surface. Hence, the reaction of NO with OH on ceria is one of pathways to produce nitrite and nitrate species.

Increasing the NO exposure time for longer than 30 min leads to the growth of almost all bands in the 1800 – 800 cm⁻¹ region, in addition to the evolution of a new shoulder band at 1199 cm⁻¹ assigned by bidentate nitrite [84]. It must be pointed out that nitrosyl species, which are expected to form at 1700 – 1900 cm⁻¹ by the direct adsorption of NO on metallic or ionic Pd⁰⁻²⁺ [60], are not observed in any DRIFT spectra indicating that CeO₂ or the interface between Pd and CeO₂ provides the active sites for NO adsorption rather than Pd itself. On the ceria surface, activated O* species can oxidize adsorbed NO and NO₂, giving rise to the appearance of the nitrites and nitrates species according to the

following reactions [76, 83, 84].



where “ $\text{Ce}^{4+} - \text{O}^*$ ” and “ $\text{Ce}^{3+} - \square$ ” represent an active oxygen and oxygen vacancy on ceria, respectively. Especially, it is likely that ceria in Pd/CeO₂ catalyst is highly interacted with Pd.

In addition, it is worth mentioning that the DRIFT spectra of Pd/CeO₂ obtained after NO adsorption are different from those of bare Ce-based oxide (CeO₂ or Ce_xZr_{1-x}O₂) and Pt/CeO₂. Previous reports about the adsorption of NO on the latter materials demonstrate that the major peak after NO/O₂ adsorption is located at around 1170 cm⁻¹, assigned to surface nitrites or nitroxyl anion (NO⁻) [56, 69, 83, 86]. However, in the current study on Pd/CeO₂, the IR band at 1170 cm⁻¹ is not observed, which implies that Pd on CeO₂ induces different adsorbed NO_x species from Ce-based oxide or Pt/CeO₂. Therefore, it is reasonable to claim that Pd-ceria interaction provide the adsorption site of NO (α) and/or assist the oxidation of NO_x (β)

After purging with O₂, H₂O, and N₂ (i.e. without NO) for 30 min, the intensity of the peaks decreases slightly, demonstrating that most of the adsorbed NO_x species are rather stable. It can be summarized that the primary NO_x species adsorbed on Pd/CeO₂ at 120 °C are various nitrites such as nitro-nitrito, linear, bidentate and chelating nitrites, whereas nitrate species are not

detected. In the previous literature, it is reported that NO/O₂ adsorption on Pt/CeO₂ and even bare Ce-based material at low temperature (below 100 °C) forms nitrate species [69, 87]. It is thought that the absence of nitrate species on Pd/CeO₂ might arise from the presence of H₂O in the reactant.

Based on the results of the NO desorption experiment, there are three main desorption features arbitrarily designated as α^* , α , and β peaks according to the NO_x desorption temperature and component. In the case of a low temperature NO_x adsorption catalyst, it is crucial to identify the adsorbed species leading to desorption of NO_x in the range of 200 - 500 °C. Thus, DRIFT spectra collected during temperature ramping are useful to understand the NO_x desorption mechanism. Figure 2-10 presents the DRIFT spectra of Pd/CeO₂ as a function of temperature with an IR range of 1800 – 800 cm⁻¹. With an increase in temperature from 120 to 300 °C, the IR peaks of HNO₂ (1622 and 1315 cm⁻¹), linear nitrite (1415 cm⁻¹), chelating nitrite (1230, 1042, and 830 cm⁻¹), and bidentate nitrite (1190 cm⁻¹) decrease, leading to the complete disappearance at 300 °C. It suggests that nitrite species and H₂O-related NO_x species formed by NO + OH reaction on the ceria surface are desorbed to produce NO and NO₂ gases at around 250 °C, in other words, resulting in the evolution of α^* peak.

In the temperature range from 200 to 300 °C, the generation of monodentate nitrate species are evidenced by an increase in bands at 1522, 1222, and 1031 cm⁻¹ following the reaction in Eq.(3) [76, 84, 86]. Moreover, other bidentate nitrate species are also observed at 1543, 1245, and 1010 cm⁻¹ [76, 84, 86].

Previous literature reported that the $\text{HNO}_2\text{-H}_2\text{O}$ species are decomposed to release H_2O and form bidentate nitrite species on the ceria surface, which are transformed progressively into bidentate nitrate ones due to the oxidation above $200\text{ }^\circ\text{C}$ [84]. It is also confirmed that the development of these nitrate bands leads to the formation of the $\nu_3 + \nu_1$ combination mode at around 2546 cm^{-1} and the overtones of the 1543 , 1522 , 1222 , 1030 , and 1006 cm^{-1} bands at ca. 3076 , 3026 , 2430 , 2050 , and 2014 cm^{-1} , respectively (not shown) [76, 84].

In the $200 - 350\text{ }^\circ\text{C}$ temperature range, another noteworthy phenomenon is that nitro-nitrito compound (at 1475 cm^{-1}) rapidly decreases and completely disappears at $350\text{ }^\circ\text{C}$. Hence, the combined results of NO adsorption/desorption and DRIFT strongly suggest that the desorption of NO gas at the α peak related to both Pd and ceria originates from the decomposition of nitro-nitrito species formed at the interface between Pd and CeO_2 .

When the temperature is elevated from 300 to $500\text{ }^\circ\text{C}$, the intensities of nitrate species (at 1543 , 1522 , 1245 , 1222 , 1031 , and 1010 cm^{-1}) gradually increase and eventually reach a maximum at 400°C . With an increase of temperature above $400\text{ }^\circ\text{C}$, these nitrate species on CeO_2 substantially begin to decrease. This leads us to conclude that the β peak desorbing as NO and NO_2 results from the decomposition of these nitrate species. As described in Figure 2-6, the β peak of Pd/ CeO_2 is significantly higher than that of CeO_2 , supporting that Pd/ CeO_2 forms nitrate species more abundantly. Based on these results, it is summarized that Pd on CeO_2 plays a crucial role in promoting the oxidation

of nitrite to nitrate on the catalyst.

To sum up, there are three kinds of major NO_x species participating in the NO_x desorption on Pd/CeO₂. First, various nitrite compounds on the ceria surface are desorbed at around 200 °C (α^* peak). NO desorbing from the interface between Pd and CeO₂ at around 300 °C is related to nitro-nitrito species at 1475 cm⁻¹ (α peak). Lastly, nitrate species on CeO₂ formed by the oxidation of nitrite are decomposed into NO and NO₂ at above 400 °C (β peak).

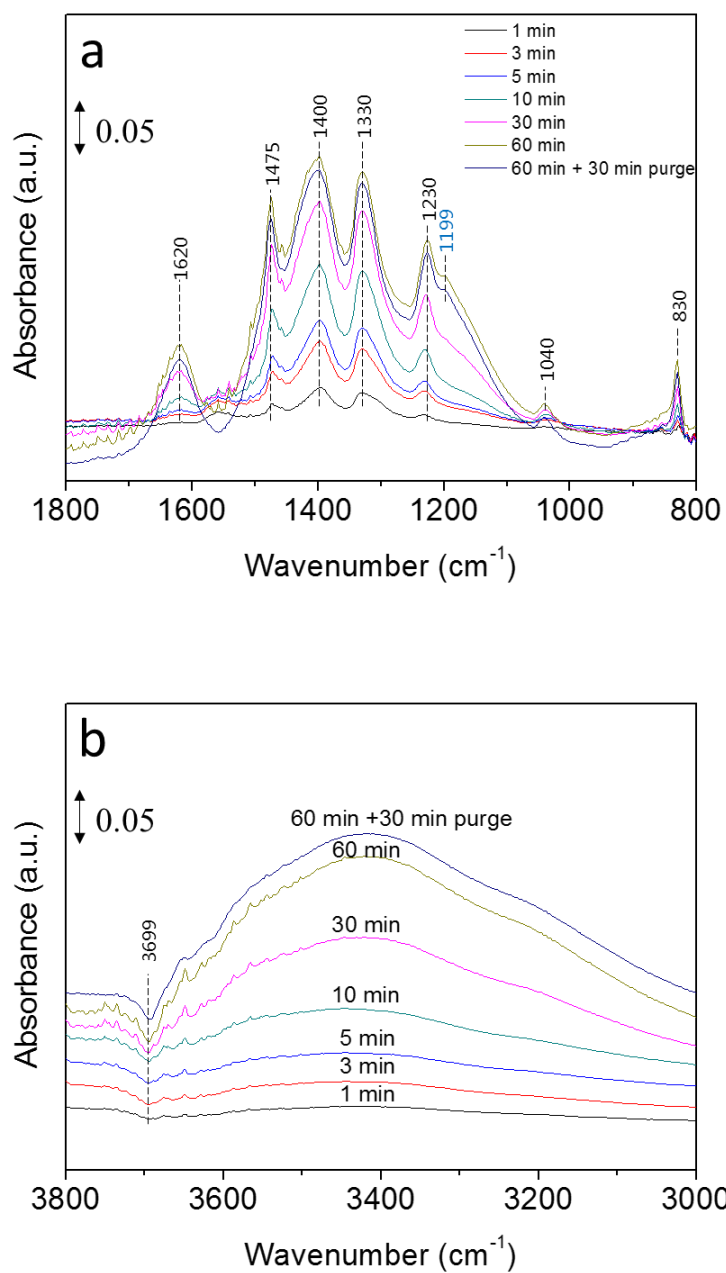


Figure 2-10. DRIFT spectra during NO+O₂+H₂O adsorption as a function of adsorption time (min) over HTA Pd/CeO₂ in the range of (a) 1800 – 800 and (b) 3800 – 3000 cm⁻¹.

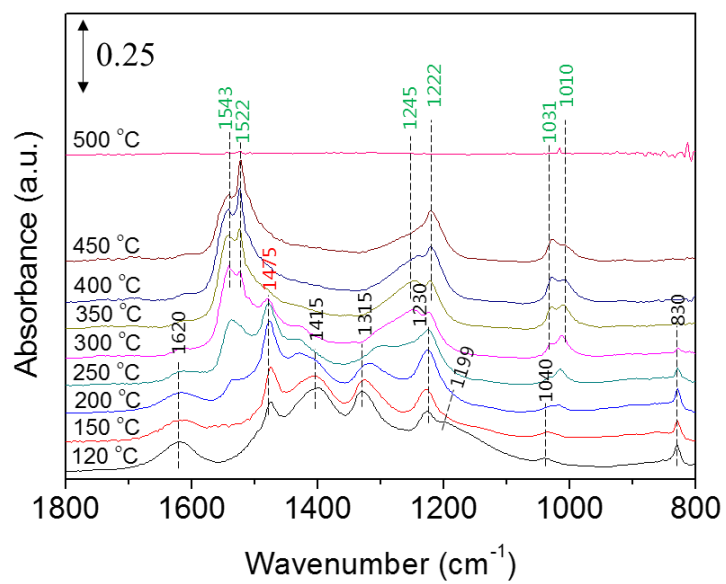


Figure 2-11. DRIFT spectra during desorption as a function of temperature (°C) over HTA Pd/CeO₂ with the range of 1800 – 800 cm⁻¹.

Chapter 3. Effect of sulfur poisoning and regeneration on NO adsorption ability over Pd/Ce-based catalysts

3.1. Introduction

Ce-based materials are easily poisoned by the sulfur species contained in the fuel and the lubricant oil. It is known that sulfur aging on CeO₂ leads to the loss of surface area and forms Ce(SO₄)₂ which prevents the alteration of oxidation states between Ce³⁺ and Ce⁴⁺, yielding the decrease in oxygen storage capacity (OSC) and catalytic activity of catalyst [68, 88-92]. In addition, there is the possibility of formation of PdSO₄, which deactivate the active PdO phase [93]. To regenerate sulfated Ce-based catalyst by decomposing thermodynamically stable Ce(SO₄)₂, high temperature treatment (above 700 °C) under oxidative or inert condition is necessary [68, 94]. Chen et al. [49] demonstrated that sulfated Pd/CeO₂ cannot adsorb NO at low temperature. However, they only reported the NO adsorption ability of sulfur aged Pd/CeO₂, so that the effect of regeneration on the NO adsorption ability remain unrevealed. In addition, it is well known that the addition of Zr in CeO₂ lattice (i.e. ceria-zirconia mixed oxides) presents improved sulfur tolerance by preventing SO₂ poisoning on catalyst and maintaining the structural and textural properties during regeneration [68, 92]. Therefore, it is of interest to understand the effect of (Ce-Zr)O₂ mixed oxide on the low temperature NO adsorption ability after sulfur

aging and regeneration.

In this work, we investigated the effect of the sulfur aging and regeneration on the low temperature NO adsorption ability over Pd/CeO₂ and Pd/Ce_{0.58}Zr_{0.42}O₂. To compare the relative chemisorption strength of SO₂ and NO over catalysts, affinity test and SO₂-TPD were carried out. Especially, we focused on the physicochemical change of catalysts during SA and DeSO_x treatment by applying N₂ physisorption, XRD, CO-chemisorption, and H₂-TPR analysis, which allow us to understand the relationship between the physicochemical property and NO adsorption ability resulting from sulfur treatment and regeneration.

3.2. Experimental

3.2.1. Catalysts preparation

CeO₂ and Ce_{0.58}Zr_{0.42}O₂ (denoted as “Ce58”) were obtained from Rhodia. 2 wt% of Pd was loaded by applying conventional incipient wetness impregnation method with aqueous Pd (NO₃)₂•2H₂O (Sigma Aldrich) solution equivalent to the total pore volume of supports. The impregnated samples were dried at 100 °C for 24 h and then calcined at 500 °C in 15% O₂ balanced with N₂ for 2 hr. Subsequently, the calcined samples (1 g) were hydrothermally aged with 15% O₂ in N₂ with 10% water vapor (total flow rate: 200 ml/min) at 750 °C for 25 hr, which was named to “HTA” sample.

In sulfur aging procedure, HTA samples (0.4 g) were exposed to SO₂ containing gases (250 ppm SO₂, 5 % H₂O, 9.5 % O₂ and N₂ with total flow rate of 200 ml/min) at 300 °C for 24 h. The amount of exposed sulfur to catalyst is 0.26 (g S/g cat). Those samples were denoted as “SA (sulfur aging)”. After sulfur aging, catalysts were regenerated by heating the SA sample while flowing 6 % O₂, 5% CO₂, and 10 % H₂O with N₂ balance from room temperature to 750 °C at a ramping rate of 10 °C/min and staying at 750 °C for 30 min. During the regeneration, the evolution of SO₂ was measured by using ULTRAMAT23 gas analyzer (SIEMENS), which was denoted to SO₂-TPD. The regenerated catalysts were named as “DeSOx”.

3.2.2. Catalysts characterizations

The specific surface area and pore structure were measured by N₂ adsorption/desorption isotherms on a Micromeritics ASAP 2010 at -196 °C (liquid N₂ temperature). Prior to the analysis, all catalysts were degassed at 250 °C for 4 h under evacuation condition.

The powder X-ray diffraction (XRD) patterns of the various treated samples were taken with a Rigaku (mode 1 smartlab) diffractometer using Cu K α radiation source operating at 40 kV and 30 mA. All catalysts were measured in the 2 θ range of 5 – 90 ° with a step size of 0.02 ° at a speed of 2.5 °/min. For each sample, the crystalline size of CeO₂ and Ce58 was obtained by using the Scherrer equation with (1 1 1) reflection.

FT-IR spectra were acquired on a M2000 (MIDAC Corp.) to investigate the adsorbed sulfur species on catalyst. Catalyst mixed with KBr at the ratio of 1:49 (total 0.2 g of mixed catalyst) was pressed into wafer by using a pelletizer. FT-IR spectra were collected at a resolution of 4 cm⁻¹ with the scan number of 64 under He flow at room temperature.

X-ray photoelectron spectroscopy (XPS) was carried out using a VG Multilab2000 (ThermoVG Scientific) equipped with Al K α (h ν = 1486.6 eV). The binding energy of C1s (284.6 eV) was used as a reference for calibration.

CO-chemisorption was measured on a BEL-CAT-II (BEL Japan Inc.) equipped with a thermal conductivity detector (TCD). In order to exclude the formation of carbonate species on ceria, which leads to excessive CO

consumption, CO pulse was introduced at $-78\text{ }^{\circ}\text{C}$ [95-97]. The samples (0.05 g) were reduced in 5 % H_2/Ar at $400\text{ }^{\circ}\text{C}$ for 30 min and cooled down to $-78\text{ }^{\circ}\text{C}$. After TCD stabilization with He, a 0.857 cm^3 of 5 % CO/He was pulsed into the reactor. The CO pulse was repeated until the TCD signal of CO peak became saturated. For calculation of metal dispersion, we assumed a 1:1 ratio of CO and surface Pd atoms.

The reducibility of catalyst was investigated by Cryo- H_2 -temperature programmed reduction (H_2 -TPR) on the same equipment of CO-chemisorption. 0.05 g of sample was pretreated under air at $300\text{ }^{\circ}\text{C}$ for 1 hr, followed by purging with Ar for 10 min prior to the measurement. After pretreatment, the experiment was carried out in a flow of 5 % H_2/Ar from -90 to $900\text{ }^{\circ}\text{C}$ at a rate of $5\text{ }^{\circ}\text{C}/\text{min}$.

For the quantitative analysis of the amount of residual sulfur on catalyst, elemental analysis was conducted with a CHNS-932 and Truspec 4640 (Leco Corp.). The measurement was repeated several times to get average value. 1~2 mg of catalyst was used for each analysis.

The Raman spectroscopic measurements of Ce-based materials were conducted with a T64000 (HORIBA Jobin Yvon) spectrometer. Ar ion laser (wavelength of 514.5 nm) was used as source of light.

3.2.2. NO adsorption/desorption activity

NO adsorption test was conducted in a continuous flow quartz reactor. The catalyst (0.1 g) sieved between 150 and 180 μm was blended with inert $\alpha\text{-Al}_2\text{O}_3$ (0.1 g). The catalyst in the reactor was sustained by quartz wool. In front of the reactor, water vapor (5 %) was injected by using a syringe pump at 120 $^\circ\text{C}$. The total flow rate was 200 ml/min at a GHSV of 120,000 h^{-1} .

During all processes of activity test such as pretreatment, NO adsorption and desorption, CO_2 (5%), H_2O (5%), and O_2 (9.5%) in N_2 were always introduced as reactants. Before NO adsorption, all catalysts were pretreated at 500 $^\circ\text{C}$ for 30 min. For NO adsorption/desorption, 100 ppm of NO was exposed for 100 sec and the temperature of the catalyst was raised from 80 to 500 $^\circ\text{C}$ at a rate of 10 $^\circ\text{C}/\text{min}$. The NO_x concentration during desorption was monitored by a NO_x analyzer (Thermo electron Corp., 42i-HL). All of adsorbed NO_x species in catalysts are desorbed below 500 $^\circ\text{C}$, which is verified by mass balance between the NO_x amount of blank test (without catalyst) and the sum of unadsorbed and desorbed NO_x species during NO adsorption/desorption. Therefore, we regarded the amount of desorbed NO_x during temperature ramping as NO adsorption capacity.

3.3. Result & discussion

3.3.1. Low temperature NO adsorption/desorption activity of Pd/CeO₂ and Pd/Ce58

Figure 3-1 shows the NO_x desorption features of the various treated Pd/CeO₂ and Pd/Ce58 catalysts in addition to HTA CeO₂ in the temperature range from 80 to 500 °C after adsorption of NO at 80 °C for 100 sec. In Figure 3-1a, HTA CeO₂ catalyst shows one symmetric peak at 220 °C arising from the desorption of nitrite species with a small trace of NO_x desorption at 450 °C originating from the decomposition of nitrate species [84]. When Pd is loaded onto CeO₂, the high temperature NO_x peak (5.5 μmol/g cat) increases significantly and new NO_x desorption peak appears at 300 °C (5.9 μmol/g cat). It is reported that PGM on CeO₂ promotes the oxidation of adsorbed nitrite to nitrate species during temperature ramping. Those nitrate species desorb NO_x at ca. 450 °C, resulting in the enhancement of the NO adsorption ability of CeO₂. [46, 98]. Moreover, although PdO cannot adsorb NO [61, 62], the addition of Pd to CeO₂ provides new adsorption site of Pd/CeO₂ desorbing NO_x at 300 °C, which is higher temperature than CeO₂ alone [98]. Hence, the NO adsorption capacity of catalyst is significantly enhanced from 8.0 to 11.4 μmol/g cat. when Pd is loaded on CeO₂. Also, it must be pointed out that the desorption temperature is located between 250 and 500 °C, in other words, in the operating temperature of SCR, which is desirable. In the case of Pd/Ce58 (Figure 3-1b), HTA sample

shows similar NO_x desorption temperature with HTA Pd/CeO₂, demonstrating the presence of similar NO_x adsorption site. However, there is notable difference between two catalysts. HTA Pd/Ce58 displays only half amount of NO_x desorption at 450 °C (2.8 μmol/g cat.) compared with HTA Pd/CeO₂ (5.5 μmol/g cat.), which is proportional to the amount of ceria in catalyst. Since ceria is the main adsorption site to desorb NO_x at 450 °C, the decrease in high temperature peak might be ascribed to the decreased amount of CeO₂ in catalyst. In other words, it can be mentioned that the effect of ZrO₂ on the NO adsorption ability of Pd/(Ce-Zr)O₂ is negligible.

After sulfur aging on HTA Pd/CeO₂ and Pd/Ce58, NO adsorption ability of Pd/CeO₂ disappears completely, as evidenced by NO_x desorption curves of SA Pd/CeO₂ and Pd/Ce58 which show no NO_x desorption over all temperature range. To find out the inhibition effect of SO₂, affinity test between two gases (SO₂ and NO) and Pd/CeO₂ is conducted. Figure 3-2 shows the evolution of NO and SO₂ with time-on-stream at 300 °C. For the experiment, HTA Pd/CeO₂ was saturated with NO by introducing 100 ppm of NO at 80 °C for 1 hr and then the catalyst was heated from 80 to 300 °C. Most of NO adsorbed on catalyst is expected to exist up to 300 °C as shown in Figure 3-1. At 300 °C, 250 ppm of SO₂ is introduced into reactor similar to the sulfur aging process. When the catalyst is exposed to SO₂ at 300 °C, the abrupt desorption of NO_x species on Pd/CeO₂ is clearly observed with simultaneous adsorption of SO₂ for 20 min. It obviously indicates that SO₂ in the reactant replaces adsorbed NO, resulting in NO desorption, since SO₂ preferentially occupies the adsorption

site of NO with the stronger adsorption strength on Pd/CeO₂. Therefore, it can be summarized that adsorbed sulfur species strongly prevent the NO adsorption on catalysts. As a result, NO hardly adsorb on SA Pd/CeO₂ and Pd/Ce58 samples.

To find out the effect of the regeneration treatment on the SA Pd/CeO₂ and Pd/Ce58 samples, SO₂-TPD (i.e. regeneration) is carried out at 750 °C for 30 min. SO₂ desorbed from sulfated Pd/CeO₂ and Pd/Ce58 during regeneration is displayed in Figure 3-3. Note that the plateau around 45 min arise from the saturation of SO₂ concentration due to the limitation of gas analyzer (ca. 800 ppm). As can be seen in the Figure 3-3, adsorbed sulfur species on the SA Pd/CeO₂ and Pd/Ce58 begin to release SO₂ at ca. 650 °C and the evolution of SO₂ disappears at the end of regeneration procedure. Such result implies that the considerable amount of sulfur species in SA catalysts are desorbed during the regeneration. Furthermore, the fact that the desorption temperature of SO₂ (at ca. 750 °C) is higher than that of adsorbed NO_x species (at 300 and 450 °C) on HTA catalysts also supports that the adsorption strength of SO₂ is stronger than that of NO_x species, which is consistent with the result of affinity test as described above. Elemental analysis is carried out to measure the amount of residual sulfur on catalyst, which are listed in Table 3-1. SA Pd/CeO₂ sample has a significant amount of sulfur (4.57 wt%), whereas after regeneration, only small amount of sulfur (0.32 wt%) remains in catalyst. In the case of SA Pd/Ce58, relatively lower amount of sulfur (2.01 wt%) than that of SA Pd/CeO₂ is loaded during SA, demonstrating that ceria-zirconia mixed oxide is more

resistant to sulfur poisoning than pure ceria, as reported previously [68]. Moreover, there is not much difference in the residual sulfur between two DeSO_x samples (0.32 vs. 0.42 wt%) indicating that most of sulfur species on catalysts are removed resulting from regeneration.

After regeneration process, however, the NO_x adsorption ability of catalysts could not be recovered entirely. In Figure 3-1, DeSO_x Pd/CeO₂ and Pd/Ce58 have only one desorption peak at ca. 240 and 200 °C, respectively. Moreover, the NO adsorption capacity of DeSO_x Pd/CeO₂ (6.2 μmol/g cat.) and Pd/Ce58 (5.9 μmol/g cat.) decreases considerably in comparison of HTA sample. It is interesting to note that the NO_x desorption temperature of DeSO_x Pd/CeO₂ (at 240 °C) and Pd/Ce58 (at 200 °C) shift to lower temperature than HTA sample (at 300 °C), indicating the decrease in the stability of adsorbed NO_x species on DeSO_x samples after regeneration. Furthermore, more importantly, there is no NO_x desorption at high temperature (at 450 °C). It is reported that although CeO₂ is the main adsorption site for NO_x desorption at high temperature, the promoting effect of PdO which oxidizes adsorbed NO_x species from nitrite to nitrate is considerably important [98]. Thus, the absence of high temperature peak might be explained by the disappearance of promoting effect of PdO. Therefore, it can be summarized that the sulfur aging and regeneration leads to change physicochemical properties of Pd/CeO₂ and Pd/Ce58 significantly, resulting in the decrease in the NO adsorption ability of catalysts.

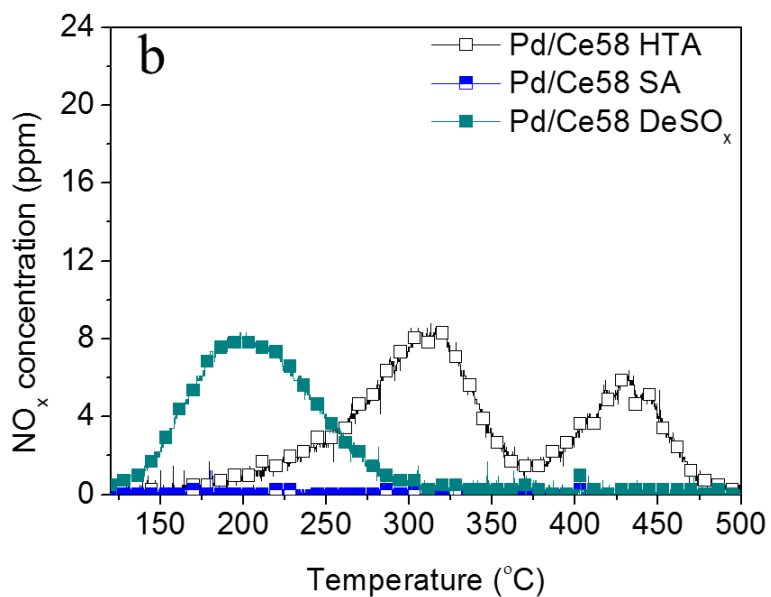
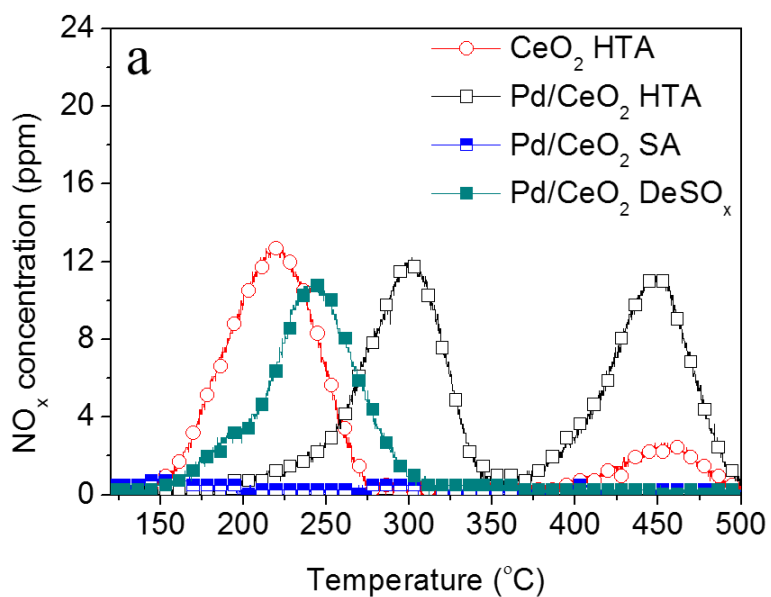


Figure 3-1. NO_x desorption curves of HTA, SA and DeSO_x (a) Pd/CeO₂ and (b) Pd/Ce58 catalysts with HTA CeO₂.

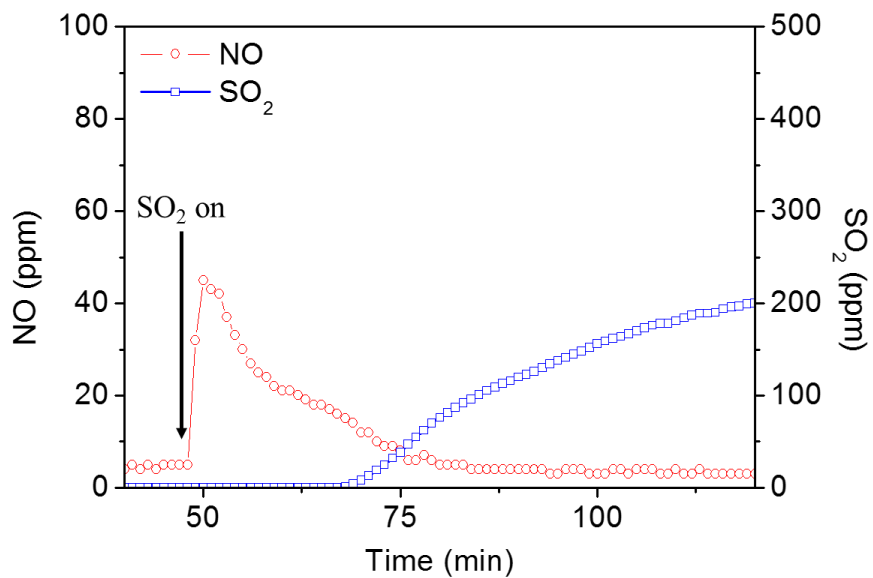


Figure 3-2. Evolution of NO and SO₂ after the introduction of SO₂ to NO pre-adsorbed on HTA Pd/CeO₂ at 300 °C.

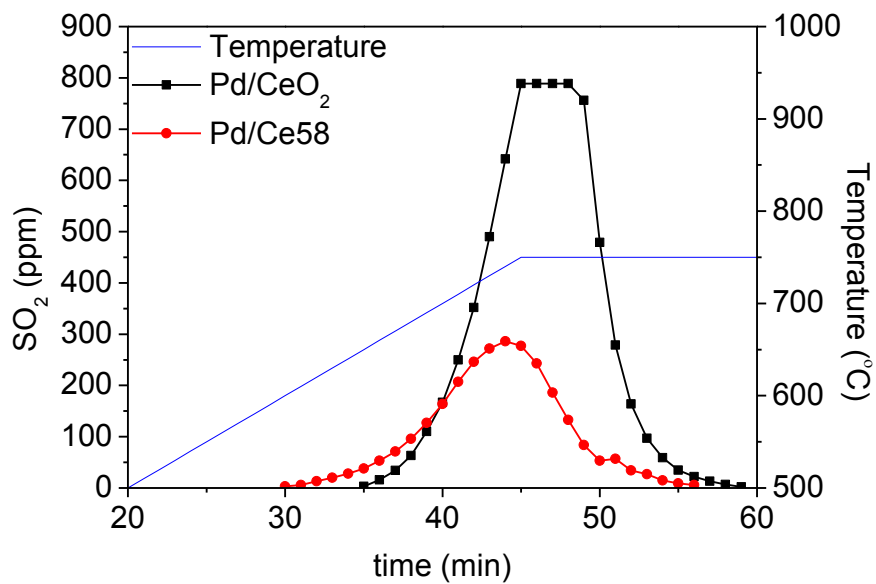


Figure 3-3. SO₂-TPD of SA Pd/CeO₂ and Pd/Ce58 catalysts.

Table 3-1. Sulfur amount, structural and textural properties, and Pd dispersion of HTA, SA and DeSO_x samples.

Sample	Sulfur amount ^a (wt%)	Crystalline size of support ^b (nm)	Specific surface area (m ² /g)	Pore volume (cm ³ /g)	Pd dispersion ^c (%)
HTA	-	11.5	86	0.26	41
Pd/CeO ₂	SA	4.57	11.5	0.14	16
	DeSO _x	0.32	26.5	0.20	10
	HTA	-	10.0	50	0.18
Pd/Ce58	SA	2.01	9.5	0.14	16
	DeSO _x	0.42	10.1	0.16	21

a: Measured by Elemental Analysis

b: Calculated by Scherrer equation

c: Measured by CO-chemisorption

3.3.2. Characterization of Pd/CeO₂ and Pd/Ce58 with various treatments

3.3.2.1. XPS and FTIR analysis

XPS analysis is carried out in order to determine the oxidation state of Pd in catalysts after the various treatments. Note that in the Pd/Ce58, since it is difficult to analyze Pd state by XPS because of the interference between Pd 3d and Zr 3p, therefore, we cannot adduce data about the Pd/Ce58. Pd 3d spectrum of HTA, SA, and DeSO_x Pd/CeO₂ (in Figure 3-4) represent the binding energy (BE) at 337.0, 336.8, and 337.0 eV, respectively. These binding energies of Pd 3d can be assigned to the typical oxidation state of Pd²⁺, supporting that the principal state of Pd on CeO₂ is PdO regardless of sulfur loading and removal. In the case of S 2p XPS (not shown), SA Pd/CeO₂ and Pd/Ce58 clearly exhibits the dominant peak at around 168 eV arising from the formation of SO₄²⁻ species [99]. Therefore, the main sulfur species formed on SA catalysts during sulfur aging is sulfate. After regeneration, the peak at 168 eV disappears completely, consistent with the elemental analysis for DeSO_x sample.

To characterize sulfur species on the SA sample, FT-IR spectrum is collected before and after regeneration. Figure 3-5 shows IR spectra of SA and DeSO_x Pd/CeO₂ and Pd/Ce58 with Ce(SO₄)₂ as a reference. The spectrum of sulfur aged catalysts presents a broad band centered around 1140 cm⁻¹ with shoulders at 1260 and 980 cm⁻¹, which is assigned to Ce(SO₄)₂ species according to the previous literature [92, 94, 100, 101]. Moreover, the

resemblance of IR peak between SA catalysts and $\text{Ce}(\text{SO}_4)_2$ also supports the formation of cerium sulfate. Note that since the IR peak intensities of $\text{Ce}(\text{SO}_4)_2$ is proportional to the amount of $\text{Ce}(\text{SO}_4)_2$ in catalyst, the relatively higher $\text{Ce}(\text{SO}_4)_2$ intensity of SA Pd/ CeO_2 indicates that the higher amount of sulfur is deposited on Pd/ CeO_2 than that on Pd/Ce58, which is well corresponding to the SO_2 -TPD and elemental analysis. After regeneration, the peak intensities of $\text{Ce}(\text{SO}_4)_2$ decrease to almost baseline, demonstrating the removal of sulfur species in both catalysts.

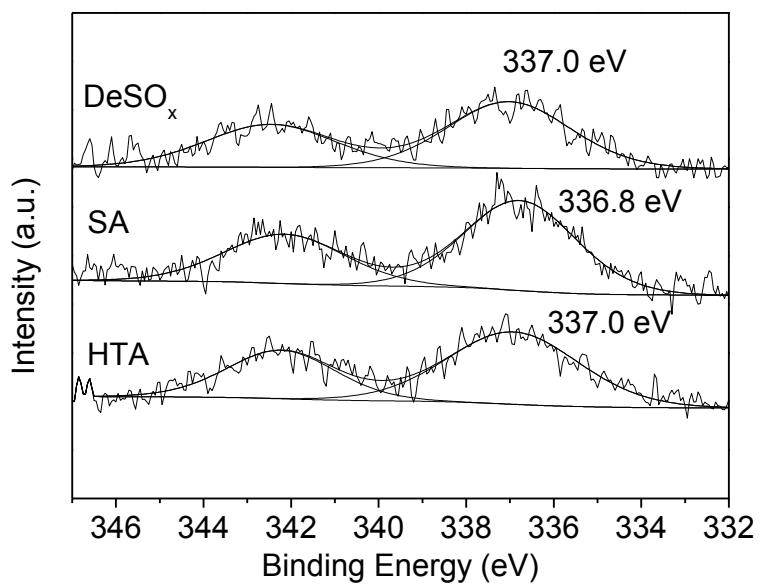


Figure 3-4. Pd 3d XPS spectra of HTA, SA, and DeSO_x Pd/CeO₂ catalysts.

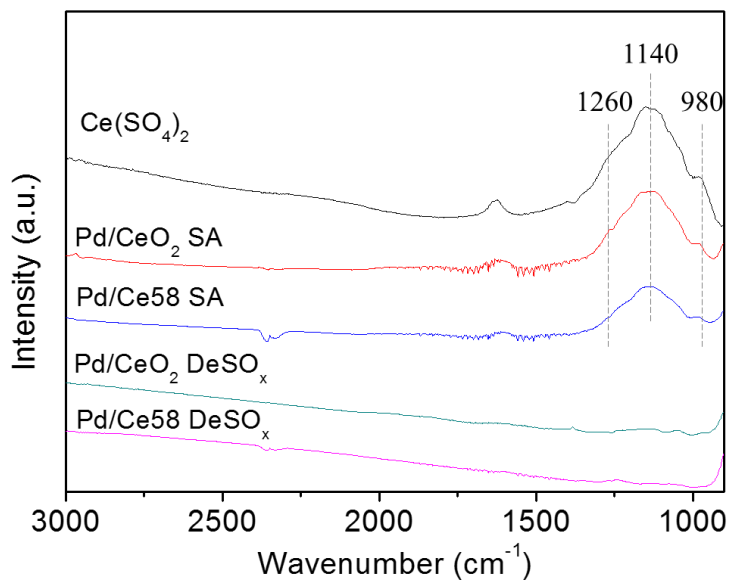


Figure 3-5. FT-IR spectra of SA and DeSO_x Pd/CeO₂ and Pd/Ce58 in the range of 3000 – 950 cm⁻¹. Ce(SO₄)₂ is shown as a reference.

3.3.2.2. XRD and BET

XRD patterns of the various treated Pd/CeO₂ and Pd/Ce58 catalysts are displayed in Figure 2-6. All Pd/CeO₂ catalysts clearly exhibit the peaks at 28.5 °, 33.1 °, 47.6 °, and 56.4 °, corresponding to the fluorite cubic structure of CeO₂ with the (111), (200), (220), and (311) planes, respectively [76, 102, 103]. In the case of Pd/Ce58, lattice shrinkage arising from the substitution of Ce⁴⁺ by Zr⁴⁺ induces the peak shift of (Ce-Zr)O₂ phase to higher 2θ compared with pure CeO₂ [104]. Those results are clearly confirmed by Raman spectra (not shown) which show F_{2g} vibration mode of fluorite type lattice at 463 cm⁻¹ in CeO₂ and a progressive shift of the fluorite band from 463 to 473 cm⁻¹ in Ce58 attributed to cell contraction due to Zr incorporation into Ce lattice. In addition, there is no peak separation in XRD between CeO₂ and ZrO₂, indicating the formation of stable solid solution of (Ce-Zr)O₂ after the HTA treatment. It is worth to note that no PdO phase at 33.9 ° (JCPDS 43-1024) is observed, implying that the crystalline sizes of PdO in catalysts are below the detection limit of XRD. Thus, it can be mentioned that PdO is well dispersed on supports and the sulfur treatment on Pd/CeO₂ and Pd/Ce58 do not affect the particle size of PdO significantly. Crystalline sizes of CeO₂ and Ce58 in various treated catalysts calculated by Scherrer equation are listed in Table 3-1. The crystallite size of CeO₂ in the HTA sample is 11.5 nm. Since there is no remarkable change in the patterns between HTA and SA sample, the crystalline size remains unchanged after sulfur aging. However, regeneration treatment leads to the increase in the

peak intensity and the decrease in the peak width, giving rise to the significant growth of crystalline size from 11.5 to 26.5 nm. Such observation strongly demonstrates that during the decomposition of $\text{Ce}(\text{SO}_4)_2$ (i.e. regeneration process), the sintering of CeO_2 takes place seriously. However, in contrast, Pd/Ce58 shows negligible change in crystalline size after regeneration, indicating that Pd/Ce58 maintains its own structure even after regeneration procedure. The addition of Zr in CeO_2 lattice results in the structural shrinkage which improves structural stability [104]. In addition, it is known that since ZrO_2 has high sulfur tolerance, sulfur aging on ZrO_2 only forms surface sulfate species with smaller amount of sulfur than that of CeO_2 [92, 105]. Since only decomposition of surface sulfate takes place during regeneration of sulfur aged ZrO_2 , the structure of ZrO_2 remains unchanged. Similar effect is applicable in $(\text{Ce-Zr})\text{O}_2$ mixed-oxide. ZrO_2 in mixed-oxide alleviates the formation of bulk $\text{Ce}(\text{SO}_4)_2$ and inhibits the structural change during regeneration. Those properties aid in maintaining catalyst structure, leading to the insignificant change in Pd/Ce58 sample during regeneration. Hence, it can be mentioned that ceria-zirconia mixed oxide have better structural stability than pure ceria during regeneration [68].

The specific surface area and pore volume of the catalysts are also shown in Table. 3-1. In addition, Figure 3-7 exhibits the pore size distribution calculated by BJH method of HTA, SA and DeSO_x catalysts. During the sulfur aging, specific surface area and pore volume of Pd/ CeO_2 decrease considerably from 86 to 40 m^2/g and 0.26 to 0.14 cm^3/g , respectively. Similar to Pd/ CeO_2 ,

the results of N₂ physisorption on HTA and SA Pd/Ce58 clearly exhibits the decrease in surface area and pore volume. Furthermore, pore size distribution in Figure 3-7 shows that the mesopore of SA Pd/CeO₂ and Pd/Ce58 around 10 nm of pore diameter is also significantly reduced, indicating the blockage of the pore due to the formation of Ce(SO₄)₂ during sulfur aging. However, after regeneration process, the totally different trend is observed between Pd/CeO₂ and Pd/Ce58. The surface area of Pd/CeO₂ decreases by 60 % although sulfate species on Pd/CeO₂ is almost removed. In addition, the small mesopore (less than 20 nm) of Pd/CeO₂ disappears completely, resulting in the formation of larger pore (~50 nm). It clearly indicates that the structure of catalyst collapsed significantly during DeSO_x process, which is well corresponding to XRD result. In contrast to Pd/CeO₂, SA Pd/Ce58 partially recovers its own surface area and pore volume after regeneration. Furthermore, there is no structural disruption, as verified by pore size distribution in Figure 3-7 which shows negligible change during regeneration. Combined XRD and N₂ physisorption results clearly reveal that (Ce-Zr)O₂ mixed oxide have more stable structure during the decomposition of Ce(SO₄)₂ in catalysts. However, it must be pointed out that both DeSO_x Pd/CeO₂ and Pd/Ce58 catalysts show the significant reduction of NO adsorption ability compared with HTA samples. Therefore, it can be claimed that the textural collapse cannot explain the partial recovery of NO adsorption ability.

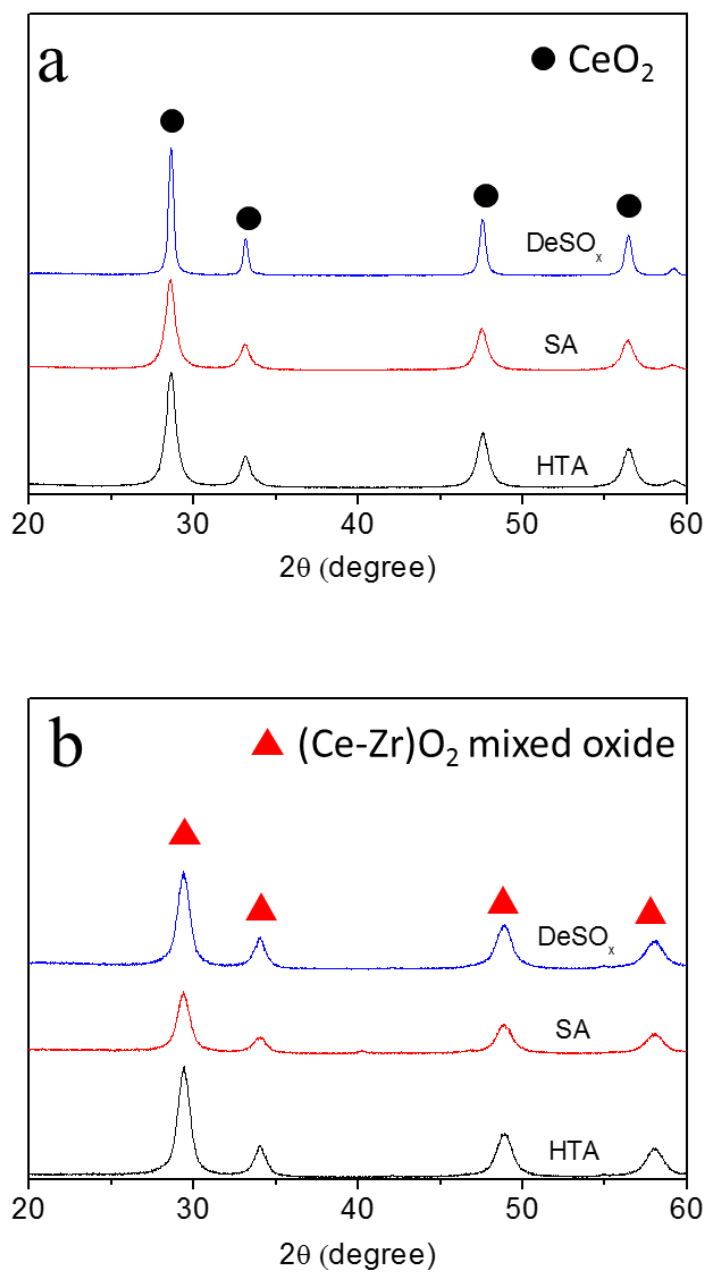


Figure 3-6. XRD patterns of HTA, SA and DeSO_x (a) Pd/CeO₂ and (b) Pd/Ce58 catalysts.

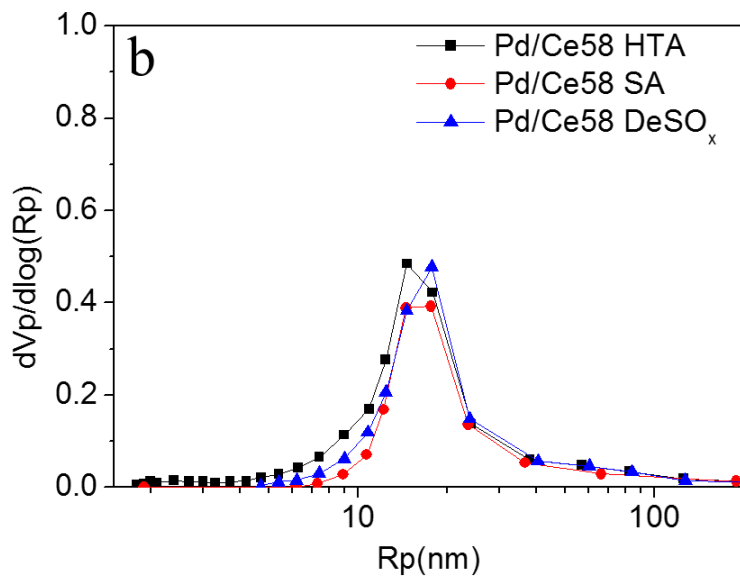
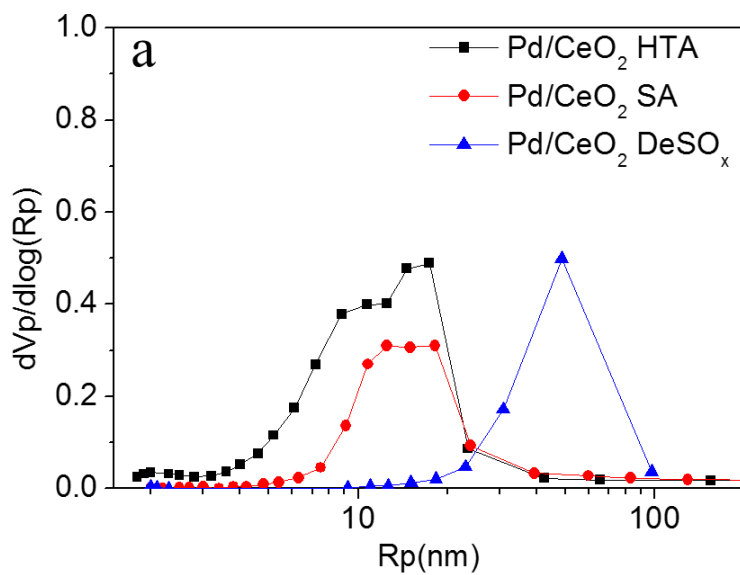


Figure 3-7. Pore size distribution of HTA, SA, and DeSO_x (a) Pd/CeO₂ and (b) Pd/Ce58 catalysts.

3.3.2.3. CO-chemisorption and H₂-TPR

To investigate the change in Pd state, Pd dispersion on HTA, SA and DeSO_x samples are measured by using CO-chemisorption, which are listed in Table 3-1. In HTA samples, Pd is well dispersed on CeO₂ and Ce58, as verified by the Pd dispersion (41 and 21%, respectively) and average particle size of Pd (2.7 and 5 nm, respectively) assuming that CO is adsorbed on Pd atom at 1:1 stoichiometry ratio. However, Pd dispersion is considerably reduced after sulfur aging. Particle size of SA sample based on CO chemisorption is 7.2 nm, which is within the detection limit of XRD. However, it is worth to point out that there are no peaks arising from Pd or PdO phase according to XRD of SA samples, implying that the discrepancy exists between two results. Since N₂ physisorption results clearly demonstrate that most of small pore in SA are covered by Ce(SO₄)₂, the decrease in Pd dispersion of SA sample is ascribed to the increase in inaccessible Pd sites due to the change in textural properties, rather than the sintering of PdO. In spite of the decomposition of Ce(SO₄)₂ during regeneration, Pd dispersion of Pd/CeO₂ further decreases from 16 to 10%. When we pay attention to XRD of DeSO_x sample, two important phenomena are noticeable. First, there is no evidence of forming crystalline PdO phase in DeSO_x Pd/CeO₂, implying that sintering of PdO does not occur after regeneration. Second one is the substantial growth of crystalline size of CeO₂ phase from 11.5 nm to 26.5 nm, in addition to the reduction of BET surface area. It means that CeO₂ is severely sintered during regeneration

process without significantly changing the size of Pd. Although the size of Pd does not change, the Pd dispersion in DeSO_x sample are reduced from 16 to 10 % compared with SA sample. On the other hand, DeSO_x Pd/Ce58 recovers its own Pd dispersion (21 %) because of the excellent structural stability. Such phenomena obviously demonstrate that the change in Pd dispersion is not the main reason for the loss of NO adsorption ability because high temperature NO_x desorption peak disappears in spite of the same Pd dispersion over DeSO_x Pd/Ce58 and HTA Pd/Ce58.

In our previous work, we reported the existence of interaction between PdO and CeO₂ by demonstrating H₂-spillover from Pd to ceria, which plays a key role in the enhancement of NO adsorption ability [98]. In order to find out the change in the interaction between PdO and ceria after regeneration, H₂-TPR was carried out for the HTA and DeSO_x catalysts. Figure 2-8 shows the H₂-TPR profiles of HTA and DeSO_x Pd/CeO₂ and Pd/Ce58 with HTA CeO₂. In the bottom of Figure 2-8a, HTA CeO₂ shows two broad H₂ consumption peaks originating from the reduction of surface and bulk CeO₂ at 500 and 800 °C, respectively [106, 107]. Compared with HTA CeO₂, HTA Pd/CeO₂ exhibits 3 features which are the reduction of PdO to Pd and the formation of Pd hydride at 23 °C, the reduction of bulk CeO₂ at 800 °C, and the decomposition of Pd hydride at 83 °C (negative peak) [108-110]. Previous literature reported that the close interaction between PdO and CeO₂ gives rise to the increase in the H₂ consumption at around PdO reduction temperature due to the simultaneous reduction of surface ceria [106, 111]. Therefore, the larger H₂ consumption at

23 °C (0.29 mmol/g cat.) than the content of PdO (0.19 mmol/g cat.) indicates the co-reduction of PdO and surface ceria arising from the close interaction between PdO and CeO₂. In HTA Pd/Ce58, note that the reduction energies of bulk ceria in the mixed oxide are comparable to the value of surface ceria [112]. Therefore, the simultaneous reduction of surface and bulk ceria is usually observed at lower temperature (at around 500 °C, in the case of bare sample) than the reduction of bulk pure ceria (at around 800 °C) [106, 113]. However, HTA Pd/Ce58 exhibits H₂ consumption peak at ca. 10 °C (0.491 mmol/g cat.) and 105 °C (0.196 mmol/g cat.) with valley-like feature at 61 °C which can be assigned to the reduction of PdO (with the formation of Pd hydride), ceria, and the decomposition of Pd hydride, respectively. It must be pointed out that the migration of ceria reduction to lower temperature (at 105 °C) than bare sample (at ca. 500 °C) and the larger H₂ consumption at 10 °C (0.491 mmol/g cat.) than the content of PdO (0.19 mmol/g cat.) clearly demonstrate the H₂-spillover originating from the interaction between PdO and ceria. Therefore, H₂-TPR results provides the solid evidence about the close PdO and ceria interaction over both HTA catalysts.

However, after regeneration process, the reducibility of Pd/CeO₂ and Pd/Ce58 is significantly changed. As can be seen in the middle of Figure 2-8a, DeSO_x Pd/CeO₂ shows several peaks at 0 – 150, 275, 500, and 850 °C. As mentioned above, the high temperature peak (at 850 °C) originates from the reduction of bulk CeO₂. Previous literature [92] reported that SO₂-poisoned Pd/CeO₂ is reduced at around 500 °C to release H₂S gas. Therefore, the peak at

500 °C is mainly assigned to the reduction of residual sulfur which is also observed in DeSO_x Pd/Ce58 in Figure 2-8b. In addition, the small H₂ consumption peak at 275 °C is attributed to the reduction of surface ceria, demonstrating that the promotional effect of Pd species which reduce the surface ceria at 23 °C mitigates substantially after SA and regeneration. Moreover, one noticeable change after regeneration is the significant decrease in the reduction of PdO. The H₂ consumption from 0 to 150 °C (0.20 mmol/g cat.) is almost equivalent to the amount of PdO (0.19 mmol/g cat.), indicating that the additional reduction of surface CeO₂ at around 23 °C can be excluded in the DeSO_x sample unlike HTA one. In the case of DeSO_x Pd/Ce58, similar phenomena are observed. After regeneration, the amount of H₂ consumed to reduce PdO at 10 °C (0.18 mmol/g cat.) declines, which is comparable to the content of PdO (0.19 mmol/g cat.). In addition, H₂ consumption of ceria at 105 °C (0.488 mmol/g cat.) increases at the expense of the amount of H₂ consumption at 10 °C. Such observations obviously demonstrate the disappearance of co-reduction of PdO and support after SA and regeneration. Although the reduction temperature of two supports somewhat increases after regeneration, they are still lower than the original reduction temperature of supports, indicating the presence of H₂ spillover. Therefore, there are two possible explanations for this phenomenon. One is the decrease in the Pd-Ce interaction, leading to the shifting of reduction temperature of DeSO_x supports at higher temperature than that of HTA ones. The other is the presence of another specific Pd-Ce interaction (or bond) which is responsible for the co-

reduction of PdO and support at PdO reduction temperature rather than H₂ spillover. The latter is more reasonable because of the presence of the co-reduction and the equivalent H₂ consumption of the sum of PdO and support between HTA and DeSO_x samples (ex) Pd/Ce58 HTA: 0.491 (10 °C) + 0.196 (105 °C) - 0.190 (PdO) = 0.497, DeSO_x: 0.180 (10 °C) + 0.488 (105 °C) - 0.190 (PdO) = 0.478 mmol/g cat.). This result indicates that although the co-reduction of PdO and Ce58 disappears completely after SA and regeneration, H₂ spillover still occurs around Pd species. Therefore, it can be claimed that there is specific Pd-Ce interaction (or bond) causing co-reduction which might be the important factor for the improvement of NO adsorption ability of Pd/Ce-based catalysts. The further analysis is needed to verify this hypothesis. Consequentially, it can be summarized that the interaction between PdO and CeO₂ is weakened by strong chemisorption of sulfur on ceria, which is not recovered even after DeSO_x process, resulting in the partial recovery of NO adsorption. Moreover, the inability of Pd to promote the oxidation of nitrite to nitrate gives rise to the complete disappearance of the high temperature NO_x desorption peak (at 450 °C).

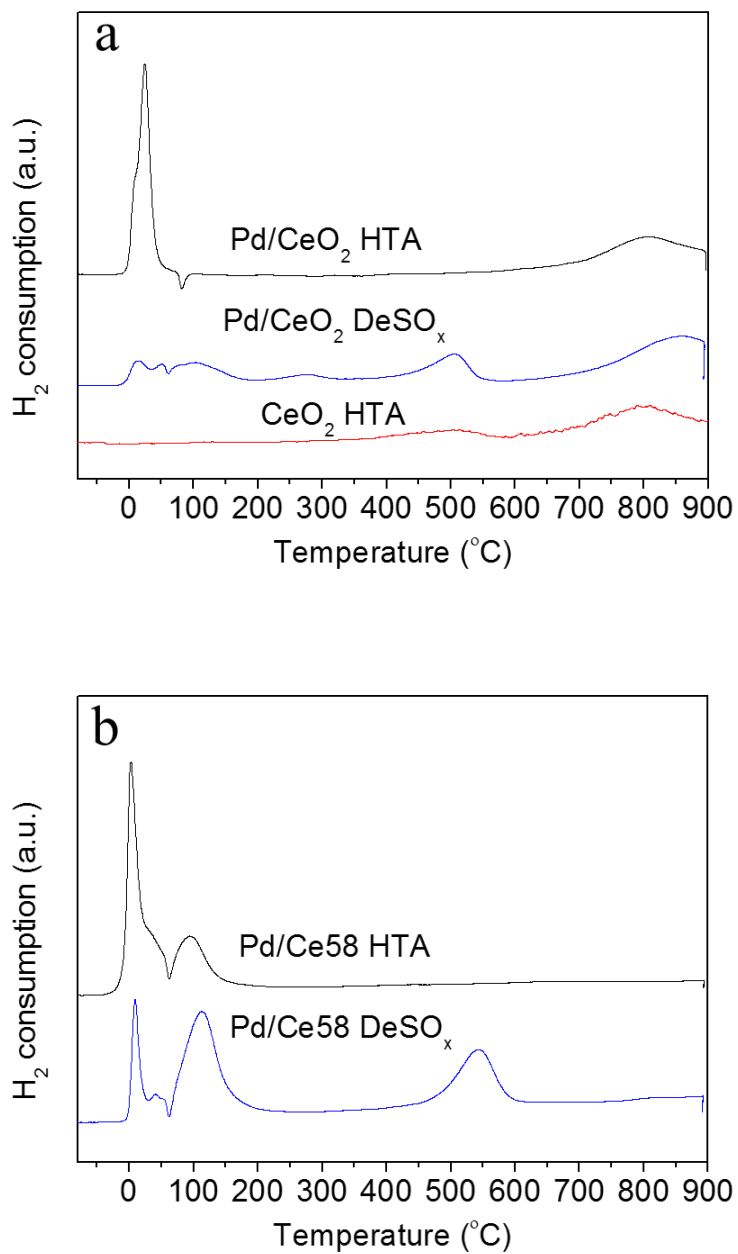


Figure 3-8. H₂-TPR spectra of HTA and DeSO_x (a) Pd/CeO₂ and (b) Pd/Ce58 with HTA CeO₂.

Chapter 4. Activation of Pd/SSZ-13 by hydrothermal aging treatment for low temperature NO adsorption

4.1. Introduction

In the case of Ce-based material having NO adsorption ability, the loading of PGM such as Pd and Pt improves the NO storage ability by helping the oxidation of NO_x species during adsorption and thermal desorption process [46, 98]. However, sulfur aging on ceria induces the blockage of NO adsorption sites, yielding negligible NO_x storage ability [114, 115]. In spite of the regeneration process, i.e. removal of sulfur, Pd/CeO₂ exhibits partial recovery of NO adsorption ability [115]. Therefore, further development of Ce-based material is required for practical application.

The alternative material as PNA catalyst is zeolite-supported Pd which has good resistance against sulfur and hydrocarbon (HC) poisoning. Numerous studies have been carried out over Pd/zeolite to apply the HC-SCR reaction such as the determination of active Pd species for HC-SCR [62, 116], NO adsorption property [59, 62, 117-120], and deactivation of Pd/zeolite [121]. Recently, NO adsorption/desorption properties of Pd/zeolite have been intensively investigated to address cold start NO_x emission. Chen et al. reported high NO storage efficiency and ability of Pd/zeolite by using various zeolites such as BEA, MFI, and CHA [114]. They also found that the framework

structures have an influence on the NO storage ability and NO_x desorption temperature. Vu and coworkers identified that the introduction of CO molecule as a reactant enhances the NO adsorption ability and raises the NO_x desorption temperature of Pd/BEA, which is explained by a change in chemical state of Pd [122]. Zheng et al. reported that multiple Pd species such as dispersed Pd (in the cationic sites), PdO₂ and PdO (on the external surfaces) coexist in Pd/zeolite (Beta, ZSM-5, and SSZ-13) [123]. They concluded that NO adsorption occurs differently depending on the presence or absence of CO and H₂O due to the variation in Pd state. In our previous work [124], it is reported that calcined Pd/SSZ-13 having PdO particles on which NO hardly adsorb exhibits negligible NO adsorption ability. However, hydrothermal aging (HTA) treatment on calcined Pd/SSZ-13 induces Pd ion exchange in SSZ-13, leading to significant enhancement of NO adsorption ability. Therefore, Pd states in zeolites play an important role in achieving the proper NO adsorption ability.

It was reported that Ce-based material can adsorb NO_x at low temperature (below 200 °C). However, facile sulfur poisoning of ceria make it difficult to apply to the practical conditions [114]. Therefore, Pd supported on zeolite attracts considerable attention as a promising material of a cold start NO_x trap catalyst due to its high tolerance against sulfur [114]. In addition, Three-way catalyst including Pd/ZSM-5 as a NO_x storage material is also reported by Honda [47].

Ogura et al. reported that in the CH₄ SCR of NO reaction, the active sites of Pd/ZSM-5 is Pd²⁺ ion species which can adsorb NO and react with CH₄, thus

suggesting that the nature of Pd plays a key role in NO adsorption [62]. Moreover, previous reports using NO as probe molecule demonstrated that Pd ion and metallic Pd species can adsorb NO, although PdO cannot [59, 60, 62, 117, 125, 126]. Thus, under the highly oxidizing condition like diesel emission, ionic Pd species in zeolite seem to be an essential component for NO_x adsorption. Chen et al. [114] reported that Pd/CHA has desirable NO adsorption ability at low temperature after comparing various zeolite supports such as CHA, MFI and BEA. Considering the synthesis method of Pd/CHA, the ion exchange of Pd²⁺ ion (0.86 Å) in SSZ-13 is expected to be difficult because of the hydrolysis of Pd ion in aqueous solution and small pore size (3.8 Å) of CHA structure. However, note that Chen et al. [114] demonstrated the presence of Pd ion in HTA treated Pd/zeolite prepared by incipient wetness impregnation which is not a common method for ion exchange, so that the effect of HTA treatment on the NO adsorption capacity and the physicochemical property of Pd/zeolite remains as a big question.

Hence, we extensively investigated the NO adsorption/desorption ability, the behavior, and the active sites of various Pd/SSZ-13 samples prepared by incipient wetness impregnation, wet impregnation, ion-exchange, and solid-state ion exchange. Especially, we focused on the physicochemical change of Pd in Pd/SSZ-13 before and after hydrothermal aging treatment by applying combined XRD, H₂-TPR, XAFS, and DRIFT analysis.

4.2. Experimental

4.2.1. Catalysts preparation

NH₄-SSZ-13, obtained from Zeolyst, was used as a support without further treatment. The Si to Al ratio of SSZ-13 is 22.4 (i.e. Si/Al_f: 22.4, Al_f: Framework Al). Pd(NO₃)₂•2H₂O (Sigma Aldrich) or PdCl₂ (Alfa Aesar) were used as Pd precursor depending on the preparation methods. Four methods including incipient wetness impregnation (IWI), wet impregnation (WET), ion exchange (ION), and solid-state ion exchange (S-S) were applied to load Pd into NH₄-SSZ-13. IWI method used the aqueous Pd (NO₃)₂ solution equivalent to the total pore volume of NH₄-SSZ-13. WET method was applied by mixing an excess of aqueous Pd(NO₃)₂ solution (200 ml, 5 mM) with 5 g of NH₄-SSZ-13 for 1 hr, followed by the evaporation of solvent in a rotary evaporator for 24 hr. In case of ION method, 2 g of NH₄-SSZ-13 was introduced into aqueous Pd (NO₃)₂ solution (50 ml, 20 mM) and then stirred at 65 °C for 20 hr. The filtered solid was washed with DI-water. For S-S method, PdCl₂ and SSZ-13 was ground together in a mortar for 1 hr. 2 wt% of Pd was loaded on SSZ-13 by using four methods. Furthermore, to investigate the effect of Pd loading, Pd/SSZ-13 catalysts with various Pd loadings (0.2, 0.5, 1, 2, 3, and 5 wt%) were synthesized by applying IWI method. After loading Pd, all catalysts were dried at 105 °C for 24 hr and calcined at 500 °C in 15% O₂ balanced with N₂ for 2 hr, which were designated as “fresh”. In order to investigate hydrothermal stability,

the calcined samples were treated with 15% O₂ and 10% H₂O in N₂ (total flow rate: 200 ml/min) at 750 °C for 25 hr, which were denoted to “hydrothermal aging (HTA)” samples. Note that there is no Pd loss within the error in Pd/SSZ-13 during HTA treatment, which is verified by ICP measurement before after HTA treatment (ex) Pd(1)/SSZ-13 IWI: As synthesized (1.11 wt%), Fresh (0.94 wt%), and HTA (0.97 wt%).

Sulfur aging (SA) on Pd/SSZ-13 was conducted with same method in the Chapter 3.

4.2.2. Catalysts characterizations

Information about the crystalline structure of the fresh and HTA catalysts was obtained from powder X-ray diffraction (XRD) using a Rigaku (mode 1 smartlab) diffractometer with Cu K α radiation (40 kV and 30 mA). The XRD patterns were collected in the range of 5 – 90 ° (2 θ) with a step size of 0.02 ° at a speed of 2.5 °/min.

Cryo-H₂-temperature programmed reduction (Cryo-H₂-TPR) was carried out by using a BEL-CAT-II (BEL Japan Inc.) with a thermal conductivity detector (TCD). 0.05 g of sample was oxidized in a flow of 21 % O₂/N₂ at 300 °C for 1 h prior to the measurement. After pretreatment, the sample was cooled down to -90 °C and exposed to 5 % H₂/Ar. Temperature was raised from -90 to 900 °C at a rate of 10 °C /min.

Pd K-edge X-ray absorption fine structure (XAFS) of the catalyst was

collected in ambient condition at Pohang Accelerator Laboratory (7D-XAFS beamline in PLS-II) using Si(111) crystal as monochromator where the beam energy and ring current were 2.5 GeV and 300 mA, respectively. Energy calibration was carried out for the samples by the Pd foil ($E_0 = 24,350$ eV). X-ray intensity for Pd K-edge signal was monitored by using ionization chambers purged with pure N₂ gas at room temperature for the measurement of incident (I_0) and fluorescence (I_f) beam. Bulk PdO was used as reference compounds. The step and duration time for X-ray absorption near edge structure (XANES) and extended X-ray absorption fine structure (EXAFS) were 1.0 eV and 2 sec, and 0.30 nm⁻¹ and 3 sec, respectively. The total number of points per XAFS spectrum was 478, sufficient for the analysis of EXAFS. The obtained EXAFS data were analyzed by ATHENA and ARTEMIS.

For XAFS analysis, Artemis implemented in in Demeter program package (0.9.25) was utilized after the data processing using Athena. The background removal was performed to extract XAFS signal using AUTOBK program for $R_{\text{bkg}}=0.1$ nm and subsequently the corresponding XAFS data in k space was fourier transformed with the Kaiser-Bessel window function, 10 nm⁻¹ after k^3 weighting to amplify the high k information. The range for fourier transformation for Pd samples, Δk were 30 – 130 nm⁻¹. The phase shifts and amplitude functions of the reference was generated using *Feff6L*. The curve fitting range in r space, Δr was varied depending on the sample. The number of independent point of the data for the curve fit, N_{idp} determined from Nyquist theorem was always larger than the number of variable, providing the sufficient

degree of freedom, N_{var} . The scattering path from the possible model structure was obtained from the F_{eff} calculation. Only scattering with large contribution were included in the multi-shell fitting. The manybody reduction factor, S_0^2 for Pd, 0.9 was obtained from the curve fit of the XAFS data of Pd foil under the same condition and utilized further in the curve fit of the sample. The statistical quality of the curve fit or proposed model can be determined from the R-factor available in the refinement.

Scanning transmission electron microscopy (STEM) and Energy-dispersive spectroscopy (EDS) analysis was carried out at an accelerating voltage of 200 kV in a JEM-2100F (JEOL) electron microscope equipped with Field emission gun. EDS mapping analysis was conducted on more than ten particles. By applying low dwell time and averaging over several accumulations, the beam damage of samples was minimized. During the scanning, beam tracking was used to avoid drift. All STEM specimens were suspended in ethanol and then ultrasonically dispersed. Drops of the suspension were fully deposited onto a copper grid coated with carbon and then dried overnight before analysis.

DRIFT spectra were acquired in the range of 4000 – 600 cm^{-1} with 128 scans at a resolution of 4 cm^{-1} on a Nicolet 6700 (Thermo Fisher Scientific) with a MCT detector using DRIFT cell (HARRIC praying mantis™). Before NO adsorption with 100 ppm NO, 2.5 % H_2O , 9.5 % O_2 in N_2 balance (200 ml/min), the pretreatment was conducted without NO at 500 °C for 30 min to remove impurities. After NO adsorption at 120 °C, DRIFT spectra was collected to obtain the information about the adsorbed species. DRIFT spectra were

recorded while ramping the temperature from 120 to 500 °C with the interval of 50 °C in the lean gas atmosphere, which provided us with the desorption behavior of the adsorbed species. The reference spectrum was obtained at the same temperature during pretreatment process. In the case of CO-DRIFT, the pretreatment of catalysts was conducted at 500 °C for 30 min under air condition. And then, the pretreated catalyst was cooled down to 25 °C. After purging with N₂ at 25 °C for 30min, 500 ppm of CO (in N₂ balance) was introduced to catalyst for 30 min. DRIFT spectra was collected until the purging the CO exposed catalyst for 30 min with N₂.

Inductively coupled plasma-atomic emission spectroscopy (ICP-AES) was conducted with Optima-4300 DV (PerkinElmer) to measure the amount of Pd in SSZ-13. Before analysis, 30 mg of samples was dissolved in aqua regia solution.

²⁷Al MAS (Magic angle spinning) Nuclear magnetic resonance (NMR) experiments were carried out on a 500MHz WB Bruker Avance II system operating at 4 mm MAS probe. Spinning frequency of 10 kHz, a 65 kHz spectral window, 6572 complex points, and a 0.1 s pulse delay were utilized to acquire 512 time-averaged scans. Time domain free induction decays were apodized with exponential functions corresponding to 100 Hz of Lorentzian line broadening prior to Fourier transformation.

4.2.3. NO adsorption activity

An activity test was conducted in a quartz reactor. The catalyst (0.035 g) sieved between 150 and 180 μm was mixed with inert $\alpha\text{-Al}_2\text{O}_3$ (0.1 g). The catalyst in the reactor was sustained at the same position by quartz wool. In front of the mixing line of gas mixture, water vapor (5 %) was introduced by a syringe pump while heating the line at 120 $^\circ\text{C}$. The total flow rate of the gases was 200 ml/min at a GHSV of 120,000 h^{-1} . A K-type thermocouple located on the top of the catalyst was used as the temperature of the reactor.

To simulate exhaust emission gas, CO_2 and H_2O were always introduced as reactant. Prior to NO adsorption, pretreatment was carried out at 500 $^\circ\text{C}$ with CO_2 (5%), H_2O (5%), and O_2 (9.5%) in N_2 for 30 min. For NO adsorption, 100 ppm of NO was introduced for 100 sec with CO_2 (5%), H_2O (5%), and O_2 (9.5%) in N_2 at 120 $^\circ\text{C}$. We tested NO adsorption at three temperatures such as 80, 120, and 160 $^\circ\text{C}$. Among them, 120 $^\circ\text{C}$ shows the highest NO adsorption ability. After discussion with Hyundai-Kia motors company, 120 $^\circ\text{C}$ was selected as NO adsorption temperature. After the NO adsorption process with CO_2 (5%), H_2O (5%), and O_2 (9.5%) in N_2 , the temperature of the catalyst was raised from 120 to 500 $^\circ\text{C}$ at a rate of 10 $^\circ\text{C}/\text{min}$. The NO, NO_2 , and NO_x concentration during temperature ramping were monitored by a NO_x analyzer (Thermo electron Corp., 42i-HL). To examine reproducibility of catalysts, each experiment was repeated at least 3 times, which is expressed by error bar in Fig. 2b. Note that most of our experiment conditions such as pretreatment and activity test are provided and/or determined by discussion with Hyundai-Kia Motors Company.

4.3. Results

4.3.1. Low temperature NO adsorption over various Pd/SSZ-13 catalysts

In order to investigate the effect of Pd loading methods on NO adsorption ability over the Pd(2)/SSZ-13 catalysts, various catalysts were prepared by applying four Pd loading methods such as IWI, WET, ION and S-S. Pd content (wt% and Pd/Al_f ratio) determined by ICP analysis and NO adsorption capacity of the various Pd/SSZ-13 catalysts are listed in Table 4-1. Figure 4-1 shows the NO_x desorption curves of fresh and HTA Pd(2)/SSZ-13 catalysts prepared by different synthesis methods after the adsorption of NO at 120 °C for 100 sec. In addition, NO, NO₂, and NO_x concentration of HTA Pd(2)/SSZ-13 IWI during desorption are displayed in Figure 4-2. It must be pointed out that regardless of various Pd loading methods, all of fresh Pd(2)/SSZ-13 catalysts hardly adsorb NO, as demonstrated by NO_x desorption profiles in the Figure 4-1 that shows only small trace of NO desorption at around 350 °C. In contrast, HTA Pd(2)/SSZ-13 catalysts clearly show two distinct desorption peaks having a maximum intensity at around 250 °C and 400 °C, indicating that HTA treatment allows all catalysts to have the improved NO adsorption ability. Furthermore, the fact that all HTA catalysts exhibit similar NO_x desorption profiles and, moreover, most of desorbed NO_x species (> 95%) primarily consist of NO implies the existence of the similar NO adsorption sites irrespective of loading methods. However, although the Pd content of all catalysts is around 2 wt%, it

must be pointed out that NO adsorption ability of each catalyst is slightly different depending on Pd loading method. Synthesis method using the aqueous solution (IWI; 26.2 $\mu\text{mol/gcat}$, WET; 25.8 $\mu\text{mol/gcat}$, and ION; 31.1 $\mu\text{mol/gcat}$) presents superior NO adsorption ability to S-S (17.1 $\mu\text{mol/gcat}$) method.

To obtain the information about the effect of Pd amount in SSZ-13 on NO adsorption/desorption, a series of fresh and HTA Pd(M)/SSZ-13 IWI (M: 0.2 – 5 wt%) were also evaluated. To facilitate the control of Pd loading, IWI method was adopted to load Pd on SSZ-13. Pd loadings and the amount of NO_x adsorbed of various catalysts are also listed in Table 4-1. NO_x desorption curves over the catalysts with the various Pd wt% loadings are displayed in Figure 4-3a. In the HTA catalysts, an increase in the Pd loading yields an increase in NO adsorption capacity up to 2 wt% (Pd/Al_F: 0.3). As can be seen in Figure 4-3a, Pd(0.2)/SSZ-13 IWI shows broad NO_x desorption feature from 150 to 450 °C. Above 0.5 wt% of Pd, the NO_x desorption peak of high temperature (at 400 °C) grows significantly and maintains similar intensities for the samples with higher Pd loading. In the case of the low temperature peak (at 250 °C), the NO adsorption capacity gradually increases up to 2 wt%, whereas it decreases at higher Pd content such as 3 and 5 wt% in comparison of HTA Pd(2)/SSZ-13. Figure 4-3b shows the change in the NO adsorbed on HTA catalysts as a function of Pd amount. With increasing the amount of Pd from 0.2 to 0.5 wt%, the amount of NO desorbed at high temperature considerably increases from 5.2 to 14.9 $\mu\text{mol/gcat}$ and maintains similar capacity between 10.4 and 13.9 $\mu\text{mol/gcat}$ at higher Pd loadings. However, in the case of the low temperature

desorption peak, only small amount of NO adsorption capacity increases from 0.2 (3.6 $\mu\text{mol/gcat}$) to 0.5 (4.5 $\mu\text{mol/gcat}$) wt%. In contrast to high temperature desorption peak, the significant growth of NO_x adsorption ability is observed at 1 (10.2 $\mu\text{mol/gcat}$) and 2 (14 $\mu\text{mol/gcat}$) wt% of Pd. However, 3 and 5 wt% Pd/SSZ-13 show the significant decrease in the amount of NO adsorption of 12.0 and 6.9 $\mu\text{mol/gcat}$, respectively. In summary, the peak area of low temperature NO_x desorption (<300 °C) increases up to 2wt% and decreases at above 3 wt%, whereas that of high temperature NO_x desorption (>300 °C) exhibits similar NO_x desorbed at above 0.5 wt% of Pd loading. Consequently, the sum of two desorption peaks shows volcano-shape curve with a maximum at 2 wt% (Figure 4-3b, Sum), demonstrating that HTA Pd/SSZ-13 catalyst has optimum Pd loading for low temperature NO adsorption. Besides, the fact that the high temperature desorption peak is preferentially enhanced at lower Pd content (0.5 wt%) indicates that the NO adsorption site of high temperature is more readily activated than that of low temperature. Similar to other fresh catalysts, a negligible NO adsorption ability of fresh catalysts with various Pd loadings is observed (not shown). Thus, it can be concluded that the HTA treatment is an essential process to activate Pd/SSZ-13 to adsorb NO at low temperature.

Table 4-1. Pd loadings (as synthesis) and NO adsorption capacity (after HTA) of Pd/SSZ-13 catalysts measured by ICP and NO adsorption/desorption experiment, respectively.

Catalyst	Pd content		NO adsorption capacity of HTA catalyst		
	Pd wt%	Pd/Al _f ^a	($\mu\text{mol/gcat}$) ^b	(%) ^c	
IWI*	Pd(5)	4.66 %	0.61	20.2	30.7
	Pd(3)	2.84 %	0.37	22.5	34.2
	Pd(2)	2.28 %	0.30	26.2	40.0
	Pd(1)	1.11 %	0.14	21.7	33.0
	Pd(0.5)	0.49 %	0.06	19.4	29.6
	Pd(0.2)	0.20 %	0.03	8.9	13.5
WET*	Pd(2)	2.35 %	0.31	25.8	39.0
ION*	Pd(2)	2.04 %	0.27	31.1	47.3
S-S*	Pd(2)	2.04 %	0.27	17.1	26.0

a: Framework Al

b: $\frac{\text{the amount of NOx during TPD } (\mu\text{mol})}{\text{the amount of catalyst used in experiment } (g)}$

c: $\frac{\text{the amount of NOx during TPD } (\mu\text{mol})}{\text{the amount of NOx during blank test } (\mu\text{mol})} \times 100$

*IWI: Incipient wetness impregnation,

WET: Wet impregnation,

ION: Ion exchange,

S-S: Solid-state ion exchange.

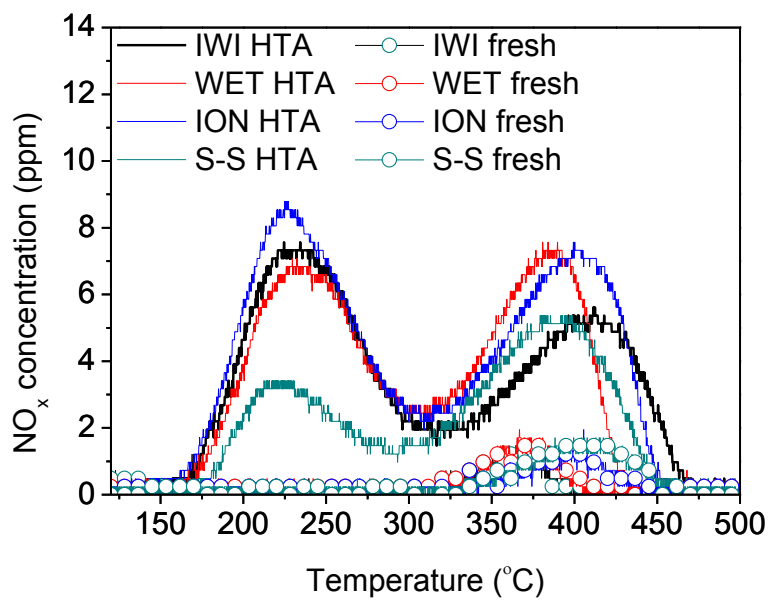


Figure 4-1. NO_x desorption curves of fresh and HTA Pd(2)/SSZ-13 IWI, WET, S-S, and ION catalysts. NO adsorption temperature = 120 °C, ramping rate = 10 °C/min.

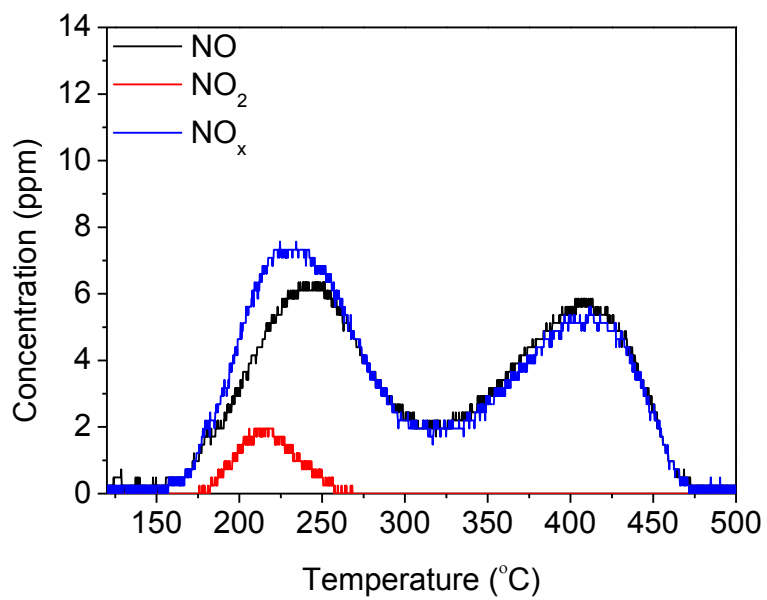


Figure 4-2. NO, NO₂ and NO_x concentration of HTA Pd(2)/SSZ-13 IWI during desorption.

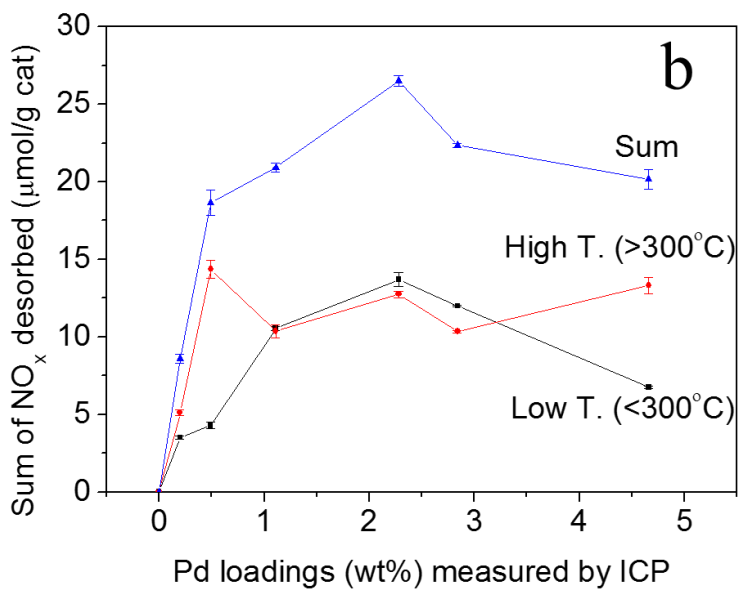
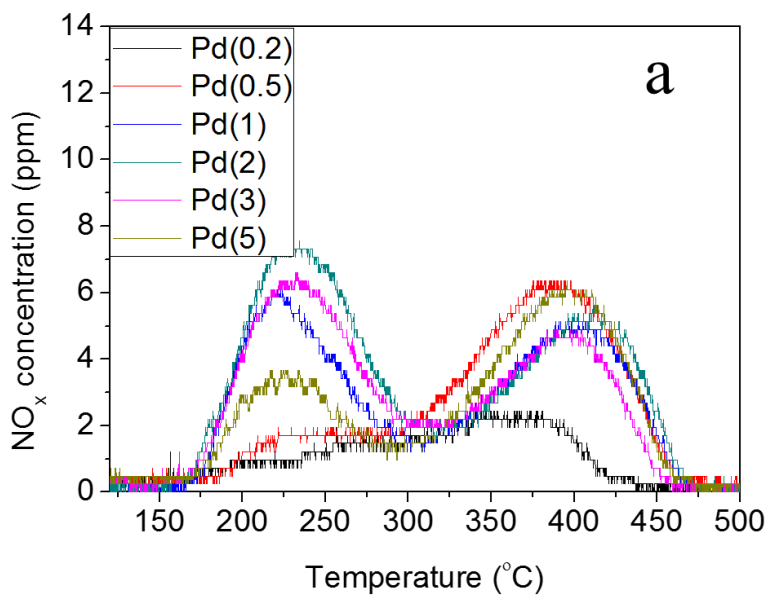


Figure 4-3. NO_x desorption (a) curves and (b) amount of Pd/SSZ-13 IWI catalyst (HTA) with various Pd loading.

4.3.2. XRD and NMR

XRD patterns of fresh and HTA Pd(2)/SSZ-13 IWI samples are shown in Figure 4-4. Moreover, the XRD patterns in the region of PdO in Pd(M)/SSZ-13 IWI (M: 0.2 – 5 wt%) are shown in Figure 4-5. Diffraction peaks of fresh Pd(2)/SSZ-13 sample are well matched with the Chabazite structure of SSZ-13 (JCPDS 52-0784). After hydrothermal aging treatment, although intensities of some peaks assigned to SSZ-13 increase slightly compared with fresh ones, the overall zeolite structure is maintained after HTA treatment. Note that bare SSZ-13 has a small diffraction peak at around 34 ° which is overlapped with that of crystalline PdO phase at 33.9 ° (JCPDS 43-1024). Such interference between PdO and SSZ-13 makes it difficult to accurately measure the peak intensity of PdO. However, in the Pd wt% ranging from 2 to 5, the increase in PdO peak intensity is clearly observed, demonstrating the growth of crystalline PdO depending on the amount of Pd in SSZ-13. Moreover, it is worth mentioning that there is no difference in the intensity of PdO peak between fresh and HTA samples except for Pd(5)/SSZ-13. In other words, the PdO peaks of Pd(2) and Pd(3)/SSZ-13 maintain its intensity even after HTA while only Pd(5)/SSZ-13 exhibits the growth of PdO peak, which provides the evidence that the sintering of PdO occurs significantly over Pd(5)/SSZ-13 resulting from HTA. Regardless of the amount of Pd loading, the remarkable change of SSZ-13 phase is not observed in any case, demonstrating that the zeolite structure of Pd/SSZ-13 catalysts is quite stable upon the hydrothermal aging treatment.

Hydrothermal aging on zeolite usually causes the extraction of Al element in the zeolite framework by hydrolysis (i.e. dealumination) without significant damage on their crystal structures. In order to investigate the dealumination of zeolite, ^{27}Al MAS NMR is carried out for fresh and HTA H-SSZ-13 with HTA Pd(1)/SSZ-13 IWI which is displayed in Figure 4-6. The spectrum of fresh H-SSZ-13 exhibits an intense peak of the tetrahedrally coordinated framework Al located at ~ 58 ppm. A peak at 1 ppm is attributed to octahedrally coordinated Al in the fresh sample. After HTA treatment on H-SSZ-13 and Pd/SSZ-13, the significant decrease in the peak of tetrahedral framework Al and the appearance of penta- and octahedral Al peaks (centered at ~ 30 and ~ 1 ppm, respectively) are observed. Such results indicate the formation of extra framework AlO_x species, resulting from dealumination of zeolite. One noticeable observation is that the peak area and intensity of tetrahedral Al in HTA Pd(1)/SSZ-13 is bigger than that of HTA H-SSZ-13, which implies that Pd containing sample has more Al sites in SSZ-13 framework after HTA treatment.

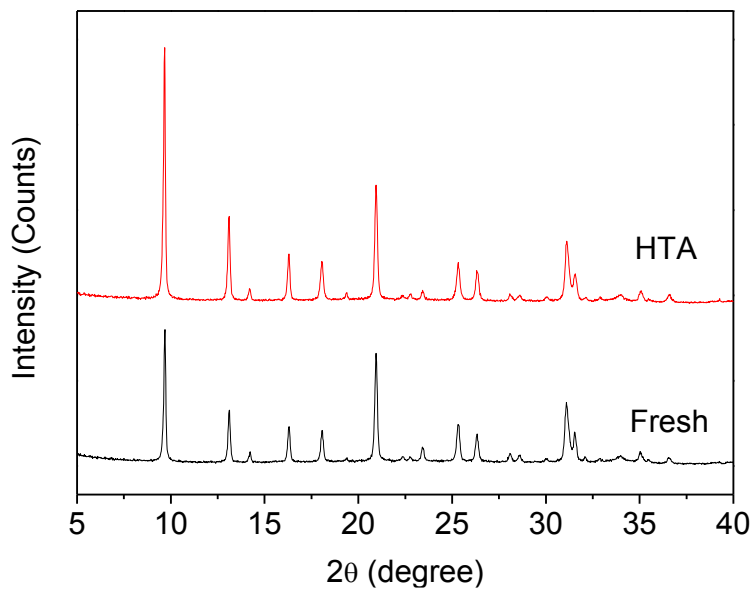


Figure 4-4. XRD patterns of fresh and HTA Pd(2)/SSZ-13 IWI catalysts.

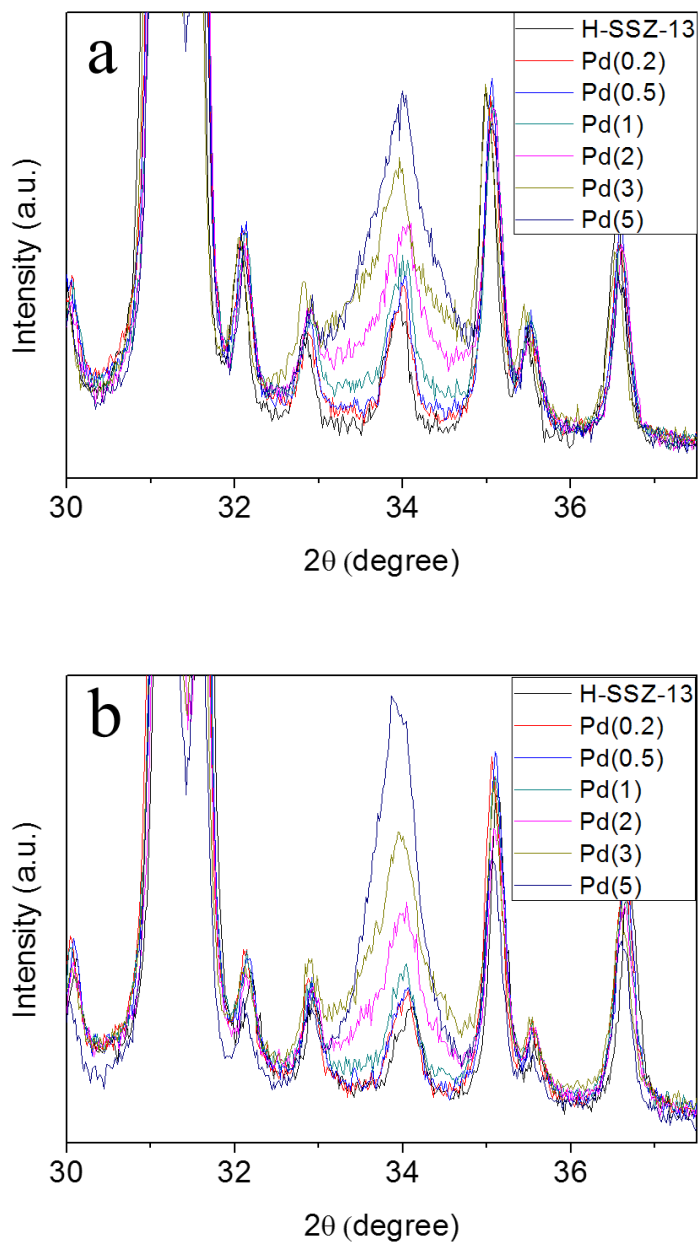


Figure 4-5. XRD patterns in the region of PdO of (a) fresh and (b) HTA Pd/SSZ-13 IWI catalyst with various Pd loading.

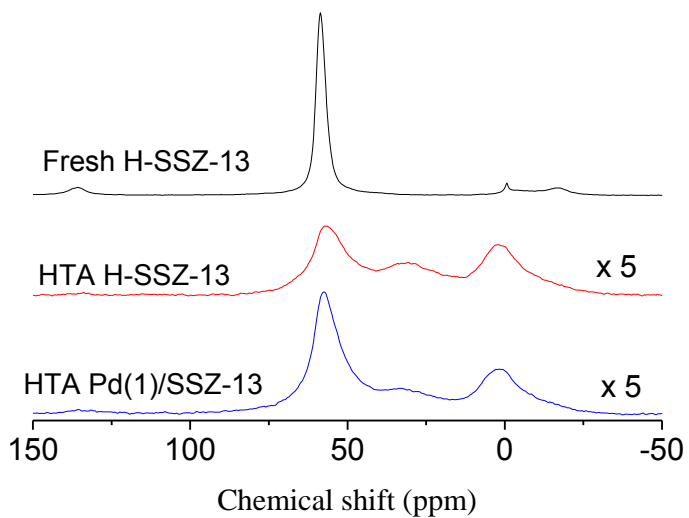


Figure 4-6. Solid-state ^{27}Al -NMR spectra of fresh and HTA H-SSZ-13, and HTA Pd(1)/SSZ-13 IWI.

4.3.3. H₂-TPR and XPS

NO adsorption/desorption activity results allow us to confirm that HTA treatment activates the adsorption site of NO on Pd/SSZ-13. Moreover, since XRD results demonstrate the maintenance of zeolite structure during HTA, we pay more attention to the change in the nature of Pd on SSZ-13 after HTA.

H₂-TPR profiles of fresh and HTA Pd/SSZ-13 IWI catalysts are displayed in Figure 4-7. All catalysts exhibit the release of physisorbed Ar in zeolite pore below - 50 °C [127]. Fresh Pd/SSZ-13 samples present a strong H₂ consumption peak at ca. 0 °C with a small minus peak at ca. 60 °C. Since H-SSZ-13 has only one desorption peak of Ar below - 50 °C (not shown), a positive and a negative feature of H₂ consumption over Pd/SSZ-13 are attributed to the presence of Pd. According to the previous study, a low temperature H₂ consumption around 0 °C is ascribed to the reduction of PdO to Pd and the formation from Pd to Pd hydride [127-129]. The minus feature at 60 °C originates from the decomposition of Pd hydride to release H₂, which is in good agreement with previous studies [127, 128, 130]. In Figure 4-7, the intensities of PdO reduction are linearly proportional to the amount of Pd in fresh Pd/SSZ-13, demonstrating that PdO exists primarily in fresh Pd/SSZ-13 samples.

However, hydrothermal treatment leads to a significant change in the reducibility of Pd in SSZ-13. Below 1 wt% of Pd, the peak intensity at ca. 0 °C is hardly shown after the HTA. Furthermore, the decomposition feature of Pd

hydride disappears, indicating that most of Pd in HTA Pd(0.5 and 1 wt%)/SSZ-13 have a different nature from PdO in fresh ones. In addition, compared with fresh catalysts, a broad H₂ consumption peak from ca. 25 to 125 °C is noticeably observed. It is reported that Pd ions located in supercages of zeolite X and Y are reduced by H₂ at around 90 °C [129, 130]. Furthermore, Sachtler et al. observed that the reduction peak of Pd ions in zeolite is located at much higher temperature (90 – 250 °C) than PdO with a broad feature [127, 131, 132]. Therefore, such observation provides the evidence of the presence of Pd ion species in HTA Pd/SSZ-13 samples.

With increasing Pd loadings to 2 and 3 wt% in HTA Pd/SSZ-13 sample, H₂ consumption peak of PdO comes to appear with a broader and smaller peak at higher temperature than that of fresh ones. Previous literature [128] reported that smaller PdO particle on zeolite support exhibits broader reduction peak at higher temperature (ca. 26 °C) than large PdO particle, which supports the formation of small PdO particles on Pd/SSZ-13 with high Pd loading after HTA treatment. Moreover, despite the peak overlapping between the Pd ion reduction and PdH_x decomposition at higher Pd loading samples (2 and 3 wt%), we could observe the existence Pd ion over the HTA samples, as evidenced by the higher background in the range of 25 – 100 °C. Thus, H₂-TPR led us to confirm that HTA treatment induces the redispersion of bulk PdO into Pd ions, in addition to the formation of smaller PdO particle.

Based on the quantitative analysis calculated by the numerical integration method, Figure 4-8 exhibits the amount of H₂ consumption to reduce bulk PdO

in Pd/SSZ-13 as a function of Pd wt%, in addition to the difference in the amount of H₂ consumed for bulk PdO reduction between fresh and HTA catalysts. As mentioned above, in the fresh catalysts, the amount of H₂ consumption to reduce PdO is almost equal to that of Pd in Pd/SSZ-13, while HTA samples show the relatively lower H₂ consumption, especially at low Pd loading. The difference in the amount of H₂ consumed to reduce PdO between fresh and HTA catalysts increases and reaches its maximum at 2 wt%.

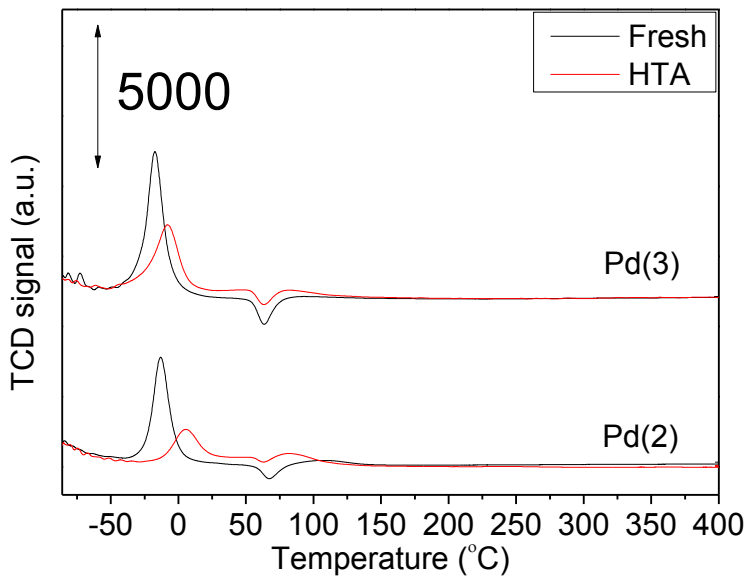
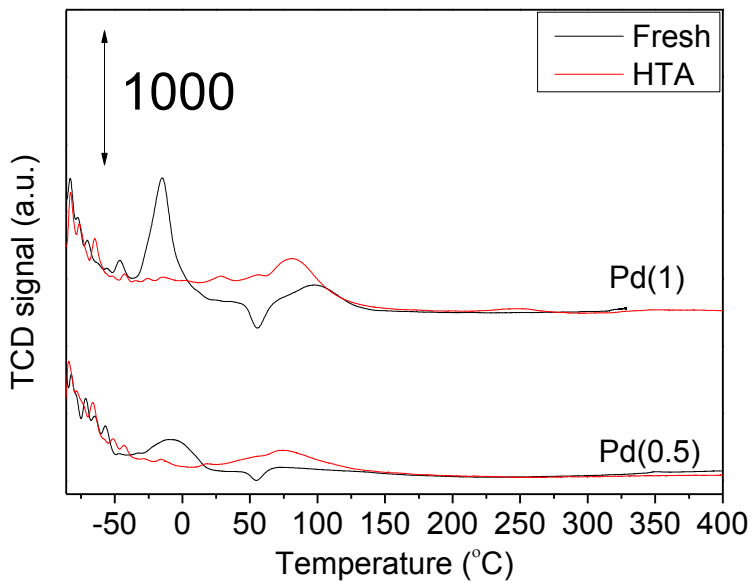


Figure 4-7. H₂-TPR spectra of fresh and HTA Pd/SSZ-13 IWI catalysts.

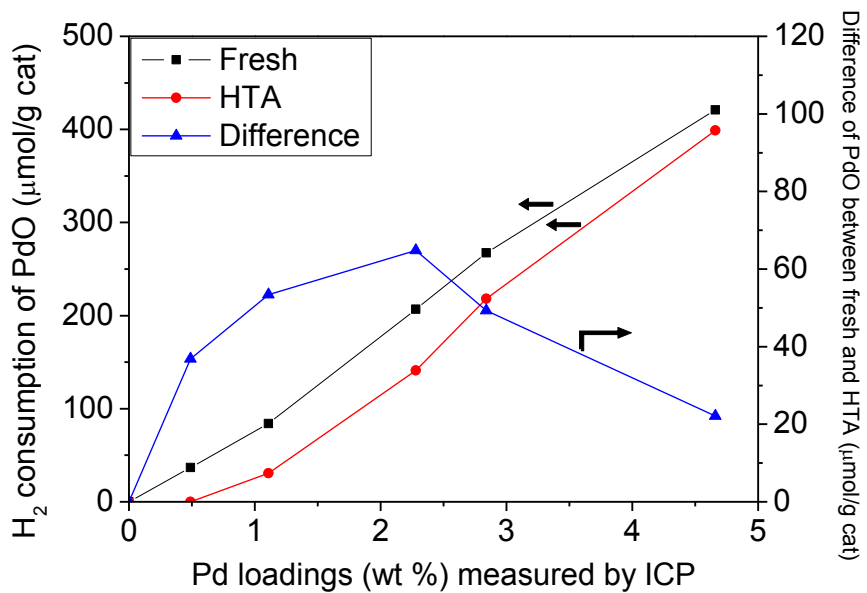


Figure 4-8. Difference of the amount of PdO reduced at around 0 °C between fresh and HTA samples calculated by H₂-TPR of Pd/SSZ-13 IWI catalyst.

4.3.4. XAFS and STEM

Figure 4-9 presents a series of selected Pd K-edge XANES spectra of fresh and HTA Pd/SSZ-13 IWI in addition to PdO and Pd foil as standards. For comparison, we selected specific Pd content such as low (0.5 wt%), middle (2 wt%), and high (5 wt%) concentration. In white line region, it is clear that the spectra of all Pd/SSZ-13 catalysts including Pd(1 and 3 wt%)/SSZ-13 (not shown) have similar shape with the spectrum of PdO, demonstrating that the dominant oxidation state of all Pd species in SSZ-13 is +2 before and after HTA.

Fourier transforms of k^3 -weighted EXAFS for fresh and HTA Pd/SSZ-13 IWI are displayed in Figure 4-10. For comparison, the spectra of PdO and Pd foil are also included in Figure 4-10. In the spectra measured before HTA (Figure 4-10), two intense peaks appeared at ca. 1.5 and 3 Å (phase shift uncorrected) due to Pd-O bond and Pd-(O)-Pd, respectively, indicating the formation of bulk PdO, which is evident from the resemblance with the spectrum for PdO reference. The similar intensities of Pd-O bond at about 1.5 Å from 0.5 to 5 wt% imply the same oxidation state of Pd (+2) in all samples in spite of the different Pd loading. On the other hand, the peak intensity of Pd-(O)-Pd increases gradually with increasing the amount of Pd in SSZ-13. Since the intensity of Pd-(O)-Pd shells is related to the size of PdO [118], it can be inferred that the particle size of PdO in fresh samples increases with the amount of Pd.

No detectable change takes place in the Pd-O peaks after HTA treatment,

whereas the intensity of Pd-(O)-Pd peak is significantly reduced especially at lower Pd content such as 0.5 and 1 wt%, implying the transformation of PdO into highly dispersed Pd²⁺ resulting from HTA treatment. Besides, it is noteworthy to point out that Pd-(O)-Pd shell is not observed in HTA Pd(0.5)/SSZ-13, which supports the presence of monodispersed Pd²⁺ ions in catalyst. Those results are well correlated with H₂-TPR result which shows the significant decrease in the reduction peak of bulk PdO as well as the appearance of the reduction peak of Pd ions after HTA.

For the case of Pd/SSZ-13 samples with 2 and 3 wt% Pd, the extent of peak reduction is not so big as the samples with lower Pd loadings, although the peak intensity of Pd-(O)-Pd decreases slightly after HTA treatment. Table 4-2 displays the coordination number (CN) and various parameter calculated by the basis of curve-fitting analysis. The CN of Pd-(O)-Pd shells for Pd(1)/SSZ-13 decreases from 2.8±2.8 to 0.8±1.2 after HTA, whereas, relatively, smaller change of CN is observed for Pd(2)/SSZ-13. This implies that the change in PdO size during HTA is related to the amount of Pd loading. With the Pd range of 0.5 – 3 wt% samples, even though the reduction of Pd-(O)-Pd peak is observed between fresh and HTA, the extent of peak reduction decreases with increasing the amount of Pd. Finally, Pd(5)/SSZ-13 shows the increase in Pd-(O)-Pd peak after HTA to the contrary, indicating the growth of PdO particle, which is good agreement with XRD result in Figure 4-5.

To further visualize the effect of HTA on Pd in SSZ-13, the distribution of Pd was examined by STEM-EDS analysis before and after HTA treatment.

Figure 4-11 shows Pd EDS maps and Z-contrast STEM images over the fresh and HTA Pd(1)/SSZ-13 IWI. In Figure 4-11a, fresh catalyst clearly exhibits several strong Pd signals (red spot) in patches. Moreover, in the same locations (red circle), dark contrasts are observed in the STEM image (Right, Figure 4-11a), indicating that the formation of large Pd particles. Based on these observations, it could be claimed that Pd is locally agglomerated on the fresh sample. After activation by HTA, however, it is shown that Pd signals are homogeneously redistributed within the whole particle (in Figure 4-11b), implying the formation of finely dispersed Pd species in HTA Pd(1)/SSZ-13 IWI. Although this result cannot be the direct evidence of the presence of Pd ion, it strongly supports the redistribution of bulk PdO in SSZ-13 resulting from HTA treatment.

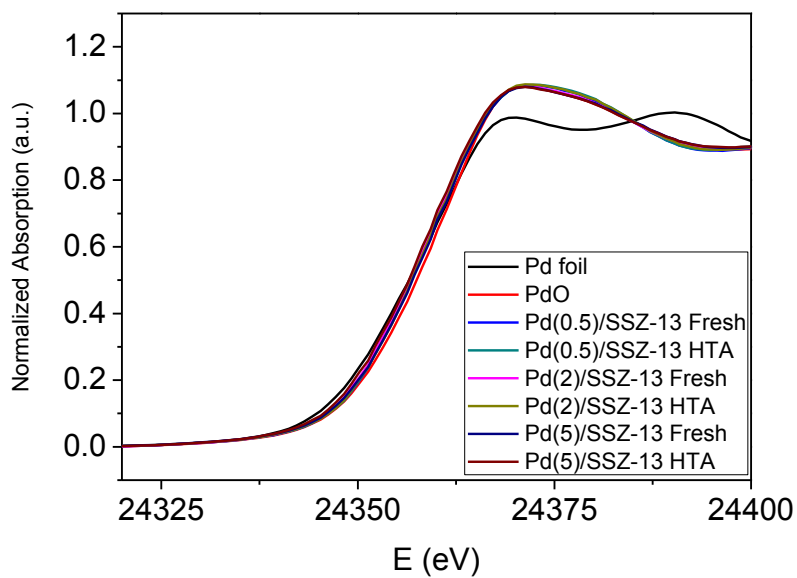


Figure 4-9. Pd *K* edge XANES of fresh and HTA Pd(0.5, 2, and 5)/SSZ-13 catalysts in addition to Pd foil and PdO.

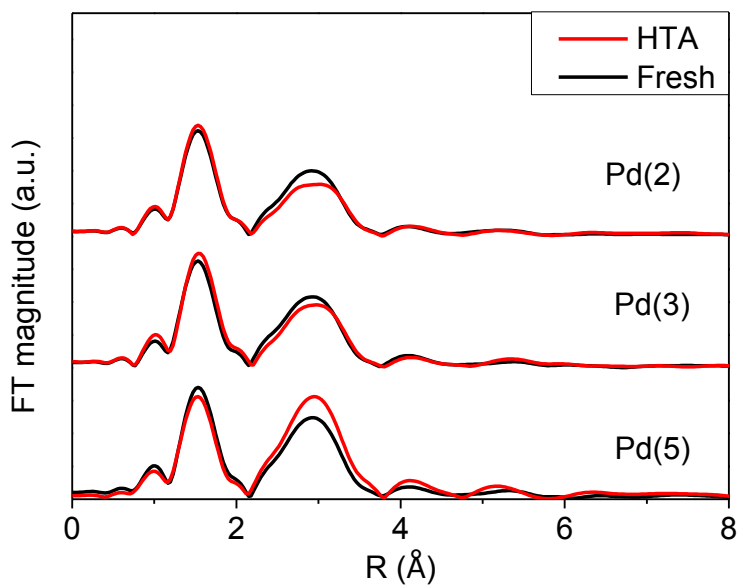
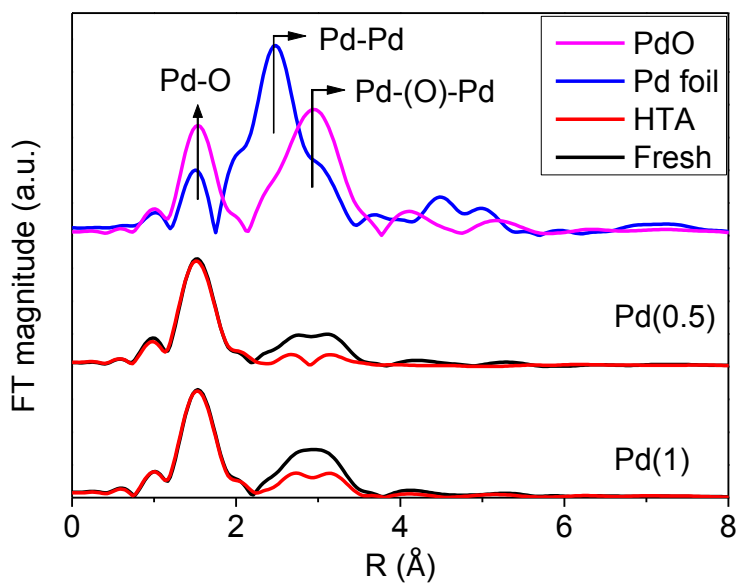


Figure 4-10. Fourier transforms of k^3 -weighted Pd K edge EXAFS for Pd metal, PdO, and Pd/SSZ-13 IWI with different Pd loadings.

Table 4-2. Results of curve fit of EXAFS data for Pd/SSZ-13 collected at Pd K edge.

Pair	CN	Distance (nm)	DW factor (μm^2)	ΔE (eV)	R-factor
Fresh Pd(1)/SSZ-13 IWI					
Pd-O	3.1±0.5	0.202±0.001	7±13	13.0±1.5	0.018
Pd-Pd	2.8±2.8	0.307±0.002	64±56		
HTA Pd(1)/SSZ-13 IWI					
Pd-O	3.8±0.7	0.200±0.001	21±16	11.0±0.0	0.058
Pd-Pd	0.8±1.2	0.306±0.003	46±73		
Fresh Pd(2)/SSZ-13 IWI					
Pd-O	3.2±0.5	0.202±0.001	12±14	12.7±1.5	0.019
Pd-Pd	4.2±2.8	0.307±0.001	68±38		
HTA Pd(2)/SSZ-13 IWI					
Pd-O	3.2±0.5	0.201±0.001	8±14	12.0±1.6	0.020
Pd-Pd	3.2±3.6	0.307±0.002	70±63		

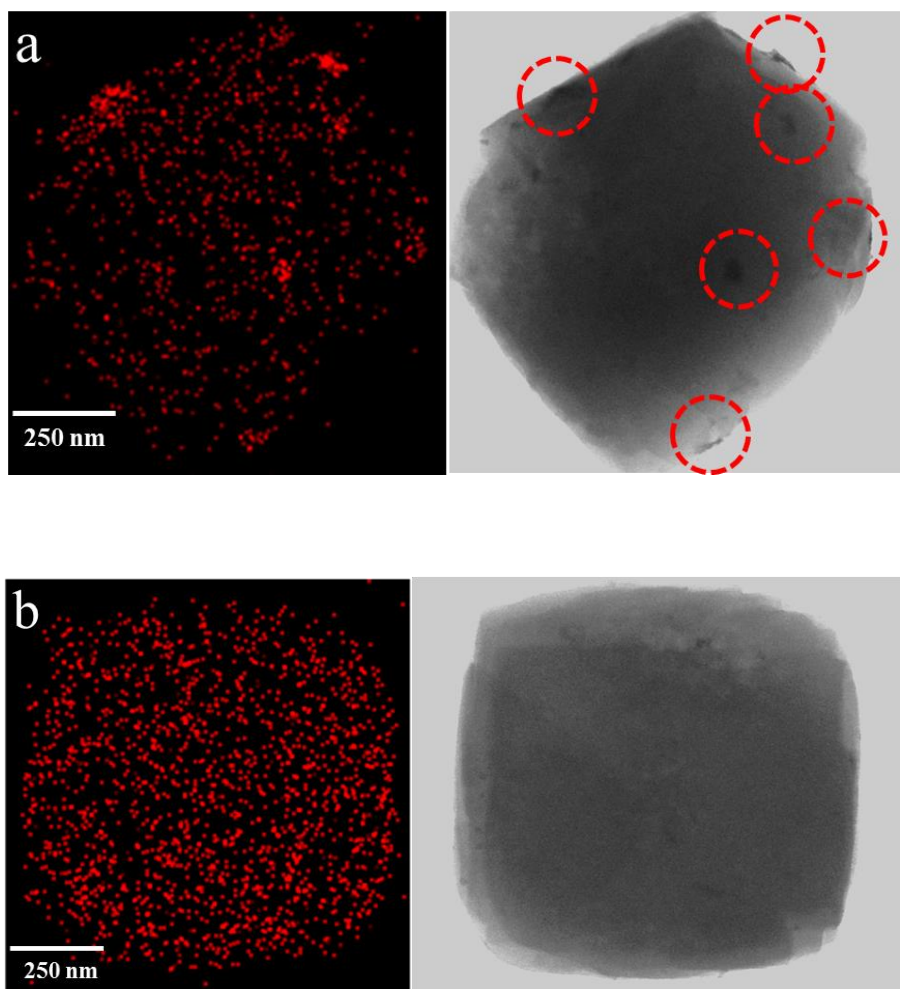


Figure 4-11. (Left) EDS mapping analysis for Pd and (Right) Z-contrast STEM image of (a) fresh and (b) HTA Pd(1)/SSZ-13 IWI.

4.3.5. DRIFT result during NO adsorption/desorption of HTA Pd(2)/SSZ-

13

As described above, HTA treatment on Pd/SSZ-13 results in the redistributed Pd²⁺ ion species which is different from PdO of fresh sample. Moreover, such well-dispersed Pd²⁺ ion species are able to provide NO adsorption ability on Pd/SSZ-13 at low temperature. In order to have a better understanding of the origin of adsorption sites and the NO adsorption/desorption mechanism of HTA Pd/SSZ-13, a DRIFT study was performed after NO adsorption at 120 °C and the subsequent temperature ramping in a temperature range of 150 – 500 °C.

Figure 4-12a exhibits the series of DRIFT spectra collected during NO/O₂ adsorption on HTA Pd(2)/SSZ-13 IWI in the presence of H₂O at 120 °C as a function of adsorption time in the range of 2000 – 1700 cm⁻¹. IR spectra of NO adsorbed HTA Pd(2)/SSZ-13 IWI obviously shows the highest peak at ca 1800 cm⁻¹ with a shoulder at 1860 cm⁻¹ both of which are assigned to nitrosyl complex on ionic Pd species [60, 114, 126, 133, 134], evidently supporting the presence of Pd²⁺ ion in SSZ-13.

On the basis of NO desorption experiment, there are two desorption peaks which primarily desorb as NO at low temperature (around 250 °C) and high temperature (around 400 °C). In order to identify the origin of NO_x desorption at each temperature, it is important to analyze the behavior of the adsorbed NO_x species during temperature ramping. Hence, after NO adsorption at 120 °C, the

series of DRIFT spectra were acquired while raising the temperature by 50 °C from 120 to 500 °C to understand the NO_x desorption process. Fig. 2-11b exhibits the DRIFT spectra of HTA Pd(2)/SSZ-13 IWI as a function of temperature with the IR range of 2000 – 1700 cm⁻¹. With the increase in temperature from 120 to 300 °C, the band at 1800 cm⁻¹ rapidly decreased. Furthermore, it must be pointed out that the band at 1860 cm⁻¹ gradually increases and eventually reaches its maximum at 300 °C. Above 300 °C, ionic Pd-NO species at 1860 cm⁻¹ begin to decrease simultaneously with the reduction of the peak at 1800 cm⁻¹.

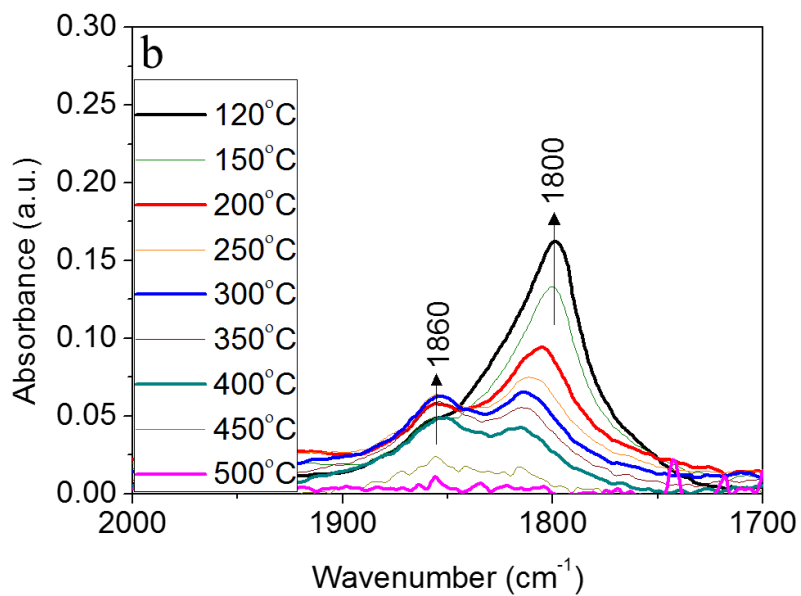
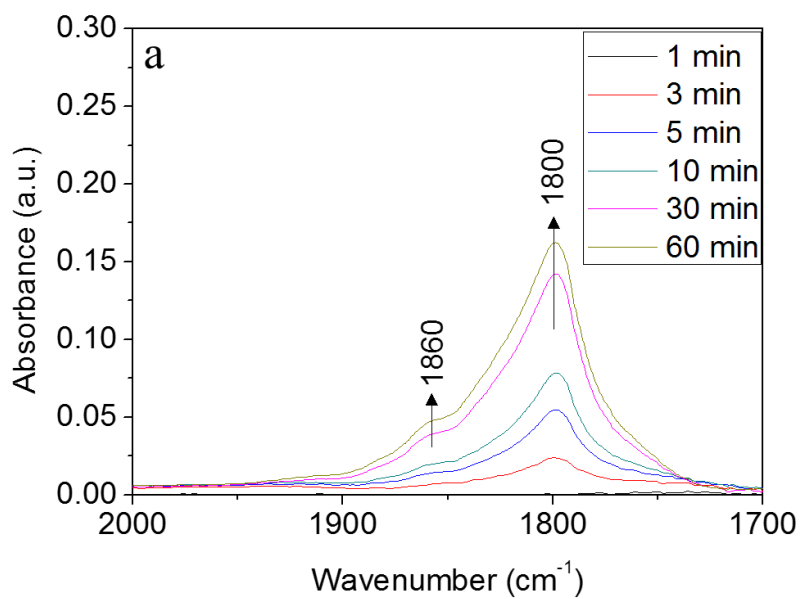


Figure 4-12. DRIFT spectra during NO (a) adsorption as a function of time (min) and (b) desorption as a function of temperature (°C) over HTA Pd(2)/SSZ-13 IWI.

4.3.6. CO-DRIFT results for fresh and HTA samples

To identify the change in the Pd species before and after HTA treatment, CO-DRIFT was conducted. Figure 4-13 displays the CO-DRIFT spectra for fresh and HTA samples. First of all, it is clearly observed that HTA sample shows a higher CO intensities adsorbed on Pd than that of fresh sample. Since the intensity of CO-DRIFT spectra reflects the amount of adsorbed CO species, such observation indicates the redistribution of Pd species after HTA treatment, which is well matched with EXAFS and STEM-EDX results. In fresh sample, three Pd²⁺-CO bands at 2159, 2142, and 2136 cm⁻¹ are found. In addition, Pd⁺-CO at 2117 cm⁻¹ and Pd⁰-CO at 2095, 1965, 1949, and 1883 cm⁻¹ are observed. Similarly, HTA sample has two Pd²⁺-CO bands at 2159, and 2133 cm⁻¹. In addition, Pd⁺-CO at 2126, 2117 cm⁻¹ and Pd⁰-CO at 2106, 2071, 1957, and 1881 cm⁻¹ are observed [135]. It is well known that Pd oxides can be easily reduced by CO. Therefore, the CO bands assigned to Pd²⁺-CO indicates the CO species adsorbed on Pd²⁺ ion [135]. In other word, the intensity of Pd²⁺-CO bands implies the amount of Pd ion species. Comparing the pick intensity of Pd²⁺-CO at ~2133cm⁻¹ between two samples, since the ratio of two peaks (HTA/fresh) is 14.4, it can be mentioned that HTA sample has more Pd ion species than fresh sample. Such observation indicates that HTA treatment induces the redistribution of Pd and the formation of Pd ion species.

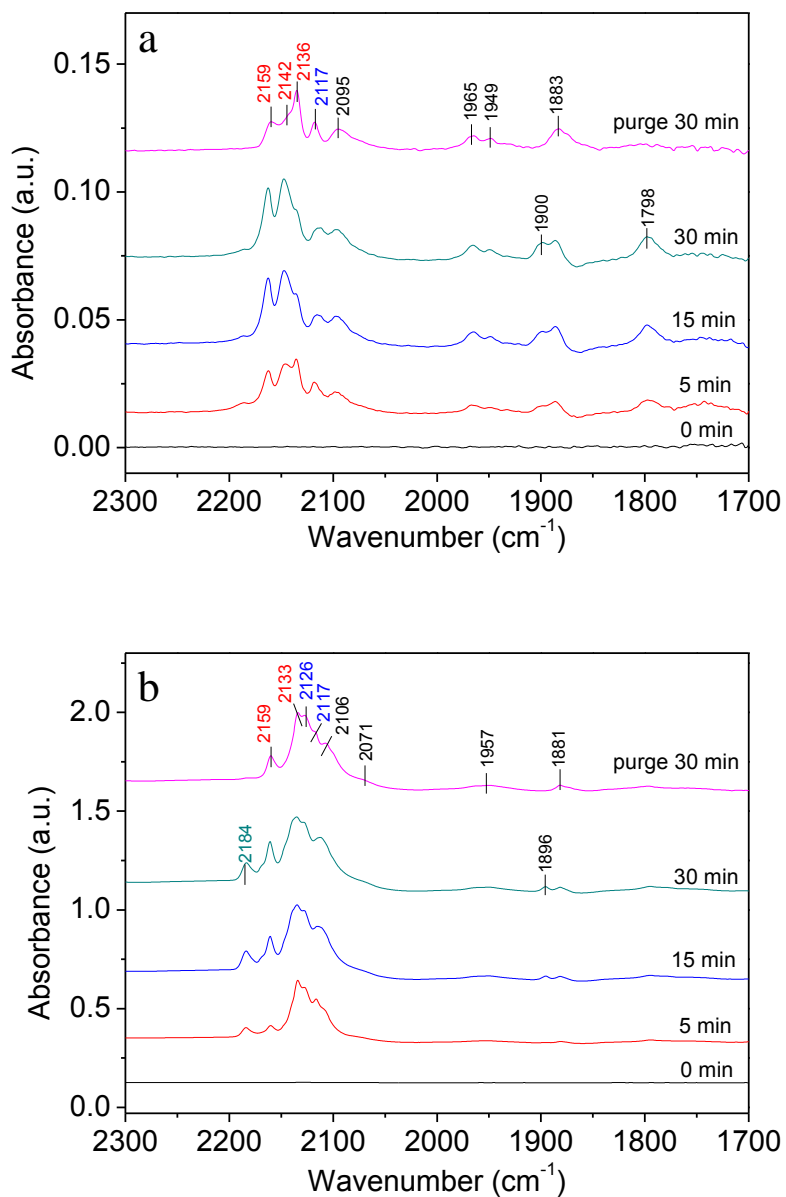


Figure 4-13. CO-DRIFT spectra for the (a) fresh and (b) HTA samples

4.3.7. Sulfur aging effect on NO adsorption ability over HTA Pd/SSZ-13

Sulfur species which are unavoidably included in the commercial fuel and lubricant oil of vehicles are well known for the poison of automotive catalyst. During the engine combustion, sulfur species are converted to SO_2 or SO_3 molecules and adsorbed on catalyst during discharge, leading to the severe deactivation of catalytic activity. To evaluate the sulfur effect on Pd/SSZ-13, NO adsorption/desorption was carried out after sulfur aging and regeneration on HTA sample. In Figure 4-14, it is clearly observed that the variation of NO_x desorption curves and amount between HTA (21.7 $\mu\text{mol/g cat}$) and SA (20.0 $\mu\text{mol/g cat}$) is insignificant, indicating that the deactivation effect of SO_2 on Pd/SSZ-13 is negligible. In addition, Pd/SSZ-13 De SO_x (21.3 $\mu\text{mol/g cat}$) also shows a similar NO_x desorption curve with HTA and SA. It is worth noticing that there is no trace of residual sulfur in Pd/SSZ-13 after SA, which is verified by EA and SO_2 -TPD (i.e. regeneration process) (data not shown). This resistance of Pd/SSZ-13 against sulfur can be explained by small pore size of SSZ-13 and the state of Pd in SSZ-13. The pore opening of zeolite SSZ-13 is about 3.8 Å which is smaller than the SO_2 molecular diameter (4.11–4.29 Å). Therefore, the penetration of SO_2 molecule in SSZ-13 is difficult, resulting in the mitigation of deactivation. In addition to pore size, the active site of Pd/SSZ-13 also affects the sulfur tolerance. In previous literature, it is reported that sulfur aging on PdO can form PdSO_4 species which can degrade the activity of

catalyst [93]. However, the main NO adsorption site of Pd/SSZ-13 is highly dispersed Pd ion at exchange sites (which will be discussed). Since SO₂ less affects such ionic Pd, Pd/SSZ-13 endures sulfur aging without significant deactivation.

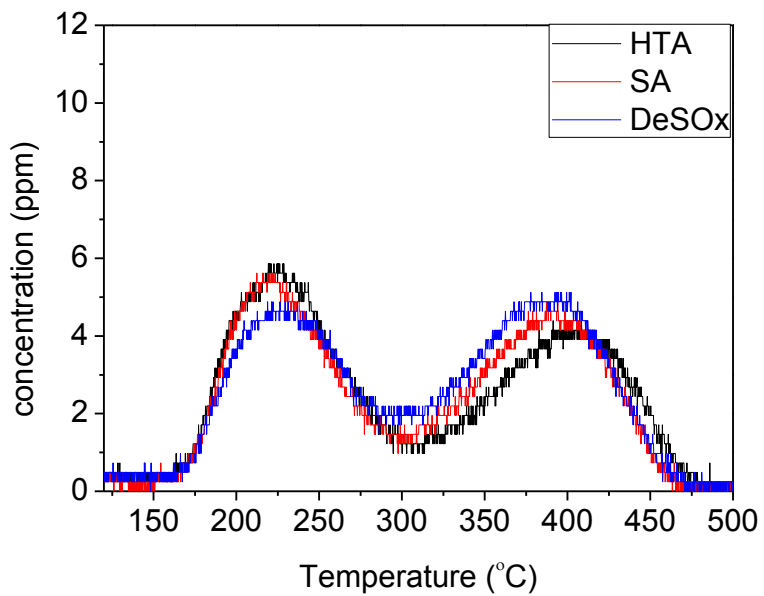


Figure 4-14. NO_x desorption curves HTA Pd/SSZ-13 after sulfur aging and regeneration treatment.

4.4. Discussion

4.4.1. The change in Pd species during HTA treatment

H₂-TPR analysis indicates that the main Pd species in fresh Pd/SSZ-13 are PdO. As mentioned in the introduction, NO is hardly adsorbed on PdO [61, 62], providing the solid reason why fresh Pd/SSZ-13 catalysts cannot adsorb NO. However, after HTA treatment, the reduction behavior of Pd in SSZ-13 is significantly changed. The difference in the amount of PdO reduced between fresh and HTA samples increases up to 2 wt% and decreases at higher Pd wt% (in Figure 4-8), which is similar to the trend of NO adsorption ability for HTA Pd/SSZ-13 IWI as a function of Pd loadings (in Figure 4-3). It strongly implies that a close relationship exists between NO adsorption capacity and the amount of Pd species which are not reduced like bulk PdO in HTA Pd/SSZ-13. In addition, HTA Pd/SSZ-13 catalysts having NO adsorption ability exhibit the broad H₂ reduction peak of Pd ion species in H₂-TPR, indicating the formation of ionic Pd in HTA Pd/SSZ-13 samples. The presence of Pd ion as an active site of NO adsorption is clearly confirmed by DRIFT spectra of HTA Pd(2)/SSZ-13 IWI. After NO adsorption, HTA Pd(2)/SSZ-13 IWI exhibit two different peaks at 1800 and 1860 cm⁻¹ assigned to nitrosyl complex on ionic Pd species. Considering the change in DRIFT peak with respect to the NO_x desorption curve in Figure 4-1, it is obvious that the desorption of NO between 120 and 300 °C is related to the nitrosyl complex at 1800 cm⁻¹ and NO desorption peak

at high temperature originates from ionic Pd-NO species observed at 1860 cm^{-1} . Therefore, it can be mentioned that Pd ions in SSZ-13 induced by HTA treatment play as an active site for NO adsorption at low temperature. In addition, both XPS and XANES results of HTA Pd/SSZ-13 support that the oxidation state of the transformed Pd species is 2+, indicating the formation of Pd²⁺ ions in catalyst after HTA treatment.

The formation of Pd²⁺ ion in SSZ-13 results from the redistribution of Pd species during HTA treatment. The decrease in the intensity of Pd-(O)-Pd shell at low Pd content such as 0.5 and 1 wt% was observed in EXAFS analysis (in Figure 4-10). Since the Pd-(O)-Pd shell reflects the formation of PdO species, the reduced intensity of Pd-(O)-Pd demonstrates the transformation of PdO into highly dispersed Pd²⁺, which also provides evidence about Pd redispersion in Pd/SSZ-13 during HTA. In addition, by visualizing agglomerated and well dispersed Pd species in fresh and HTA Pd(1)/SSZ-13 IWI, respectively, STEM-EDS also shows the redistribution of Pd. In summary, HTA treatment induces the mobility of Pd on SSZ-13, leading to the redistribution of Pd species and formation of Pd ion in SSZ-13.

The combined results of H₂-TPR, XAFS, XPS, and DRIFT clearly confirm the generation of Pd²⁺ ion in SSZ-13, which leads us to conclude that HTA treatment induces the ion exchange of Pd²⁺ ions in SSZ-13. Such phenomenon is also reported by Wang et al. [136] who demonstrated that CuO species in the fresh precipitated catalyst migrate into the SAPO-34 during the HTA treatment and form isolated Cu ions at ion exchange site. They claimed that the reduction

of CuO by high temperature (700 °C) is required for the ion exchange of Cu species. In case of Pd/SSZ-13, however, the role of H₂O is essential for the ion exchange of Pd. It is worth noticing that thermally treated Pd(2)/SSZ-13 IWI (750 °C, 25 hr without H₂O) shows negligible NO adsorption ability (almost same as the fresh samples, not shown), indicating that Pd ion exchange is not successful after HTA treatment in the absence of H₂O. Shwan et al. reported that Cu ion exchange in CuO/SSZ-13 takes place under specific gas compositions (NO and NH₃) at 250 °C [137]. They demonstrated that there are two key factors for ion exchange from CuO to Cu ion in SSZ-13. One is the reduction of CuO by NO molecule and another is the facilitation of mobility by forming [Cu^I(NH₃)_x]⁺ (x ≥ 2) complex. Similarly, it can be hypothesized that H₂O facilitates the mobility of Pd species at 750 °C, resulting in Pd redistribution and cation exchange in SSZ-13, which requires further analysis.

4.4.2. The effect of Pd ion exchange methods on the physicochemical state of Pd/SSZ-13

An insignificant NO adsorption ability of fresh Pd(2)/SSZ-13 ION obviously indicate that the main Pd species in the sample is PdO. This result clearly demonstrates the failure of cation exchange in SSZ-13 with ion exchange method. It is reported that the hydrolysis of metal ion must be prevented to introduce metal ions in zeolite by applying conventional ion

exchange [138]. However, since hydrolysis of Pd ion in aqueous solution is started at low pH (below 2) [139, 140], therefore, it is expected that the Pd ion is hydrolyzed during ion exchange procedure, resulting in the unsuccessful Pd cation exchange. In the case of medium and large pore zeolite such as ZSM-5, X, and Y, tetraammine palladium(II) ion ($\text{Pd}(\text{NH}_3)_4^{2+}$) species are generally applied [59, 141-143]. However, since the diameter of $\text{Pd}(\text{NH}_3)_4^{2+}$ could be estimated to be roughly 7.5 Å which is larger than the aperture of SSZ-13 [144], the ion exchange of Pd ion does not take place. We also confirmed no activity of fresh Pd/SSZ-13 catalyst prepared by ion exchange method using $\text{Pd}(\text{NH}_3)_4^{2+}$ species as a Pd ion (not shown). Solid-state ion exchange does not occur successfully similar to ION sample, as verified by negligible NO adsorption ability in fresh Pd(2)/SSZ-13 S-S. Previous literature reported that solid-state ion exchange takes place through the gas phase transport of PdCl_2 [130]. However, since gaseous molecule is presumably $\text{Pd}_6\text{Cl}_{12}$ whose size is approximately 7.6 Å [130], the introduction of the Pd precursor in SSZ-13 is also prevented by small pore size of SSZ-13 (3.8 Å). In summary, it can be mentioned that normal ion exchange of Pd in SSZ-13 by conventional method is difficult because of the hydrolysis of Pd ion and small pore structure of SSZ-13. Therefore, the formation of Pd^{2+} ion in SSZ-13 by HTA treatment can be regarded as the novel method for the ion exchange of Pd in small pore zeolite such as SSZ-13.

4.4.3. The limit of Pd ion exchange in SSZ-13 by HTA treatment

In NO adsorption/desorption experiment, it is confirmed that Pd/SSZ-13 with 0.3 of Pd/ A_{f} ratio (i.e. Pd 2 wt%) has the highest NO adsorption ability. In general, since the oxidation state of Pd after HTA is +2, as evidenced by EXAFS, the optimum Pd/ A_{f} ratio would be 0.5 which is equivalent with 3.8 wt% of Pd. In addition, even though 2.28 wt% of Pd (measured by ICP, 214 $\mu\text{mol Pd/gcat}$) exhibits the highest NO adsorption ability, PdO species coexist with Pd²⁺ ion in HTA Pd(2)/SSZ-13 IWI catalyst, as verified by H₂-TPR which exhibits 205 and 141 $\mu\text{mol/gcat}$ of PdO reduction in fresh and HTA samples, respectively. To estimate the exact amount of Pd ion in HTA Pd(2)/SSZ-13 IWI, titration of Pd ion is carried out by using NO-TPD. In the previous literature, the measurement of metal ion such as Pd and Cu by NO molecule was reported by using 1:1 ratio of metal cation:NO [62, 145]. In this work, since Pd ion-nitrosyl complex is mainly formed during NO adsorption, it can be assumed that the NO is able to adsorb on Pd ion at 1:1 stoichiometry. After NO adsorption for 1 hr (i.e. until the saturation of Pd ion with NO molecule), NO-TPD was conducted with similar method to NO adsorption/desorption experiment, which is displayed in Figure 4-15. As a results of titration, it was found that the amount of Pd ions capable of adsorbing NO is 50 $\mu\text{mol/gcat}$, which is similar to the amount of reduced PdO species measured by H₂-TPR before and after HTA (205 (fresh) - 141 (HTA) = 64 $\mu\text{mol/gcat}$). This result indicates that only 23 % of Pd in Pd(2)/SSZ-13 IWI is converted to Pd ion

species during HTA treatment. Such ion exchange level of Pd in SSZ-13 is explained by the limited number of ion exchange sites arising from the effect of hydrothermal treatment on SSZ-13. In NMR analysis, it is confirmed that the dealumination of SSZ-13 occurs significantly during hydrothermal treatment, resulting in the reduction of the number of framework Al sites. Therefore, it is reasonable to claim that dealumination of SSZ-13 leads to the lower number of ion exchange Al sites than theoretical one. Such decrease in the number of Al site in zeolite could explain the reason why Pd is not fully ion exchanged in SSZ-13 during HTA.

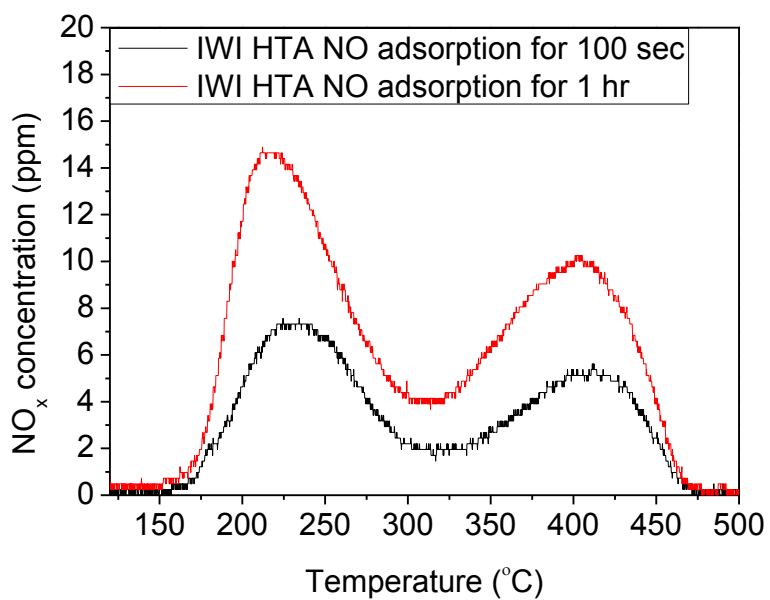


Figure 4-15. NO_x desorption curves of HTA Pd(2)/SSZ-13 IWI with different NO adsorption time: 100 sec for cold start NO adsorption (black) and 1 hr for Pd ion titration (red).

4.4.4. The effect of hydrothermal treatment on Pd/SSZ-13

In order to describe the effect of HTA treatment on Pd/SSZ-13, we propose the model for the nature of Pd species before and after HTA treatment as shown in Figure 4-16. In the case of Cu-SSZ-13, there are two ion exchange sites for Cu ion in SSZ-13 such as 6-member ring and large cages associated with 8-member ring in SSZ-13 according to the previous literature [146-148]. However, we do not have enough information to determine the position of Pd ion in SSZ-13, therefore, Pd ion in Figure 4-16b is randomly located in the possible ion exchange site. In the case of fresh Pd/SSZ-13, since Pd is not readily located into the ion exchange in SSZ-13 prepared even by ion exchange method, therefore, the principal Pd state in fresh catalysts is PdO. However, HTA treatment provides the mobility of PdO, resulting in the redistribution of Pd species within the zeolite. As a result, it is found that HTA Pd(0.5)/SSZ-13 possesses the monodispersed Pd²⁺ ion species on the basis of H₂-TPR and Pd EXAFS. When Pd loading increases from 1 to 3 wt%, the shortage of ion exchange sites in SSZ-13 arising from dealumination leads to the limited Pd ion exchange, resulting in the observation of small PdO particle compared to the fresh catalysts. Thus, small PdO particle exists together with Pd²⁺ ion species in SSZ-13. At higher Pd loading sample such as Pd(5)/SSZ-13, redispersion and sintering of Pd take place simultaneously. In the H₂-TPR result, HTA Pd(5)/SSZ-13 shows the decrease in the amount of H₂ consumed to reduce bulk PdO. Furthermore, it has NO adsorption ability at low temperature. On the

other hand, XRD and XAFS results clearly demonstrate the sintering of PdO during HTA treatment. Such contradictory results can be explained by the co-existence of Pd²⁺ ion and large PdO particles in HTA Pd(5)/SSZ-13. Therefore, in the case of HTA Pd(5)/SSZ-13, there are three kinds of Pd species which are Pd²⁺ ion, small PdO, and large PdO. In addition, based on the fact that HTA Pd(5)/SSZ-13 exhibits relatively lower NO adsorption ability than that of HTA Pd(2)/SSZ-13, it is expected that the sintering of PdO occurs more dominantly than the activation in SSZ-13 during HTA. Such assumption could be one reason for the presence of optimum Pd content in HTA Pd/SSZ-13 for low temperature NO adsorption. It can be summarized that the relative distribution of three different Pd species is totally depending on the amount of Pd in HTA Pd/SSZ-13 IWI sample.

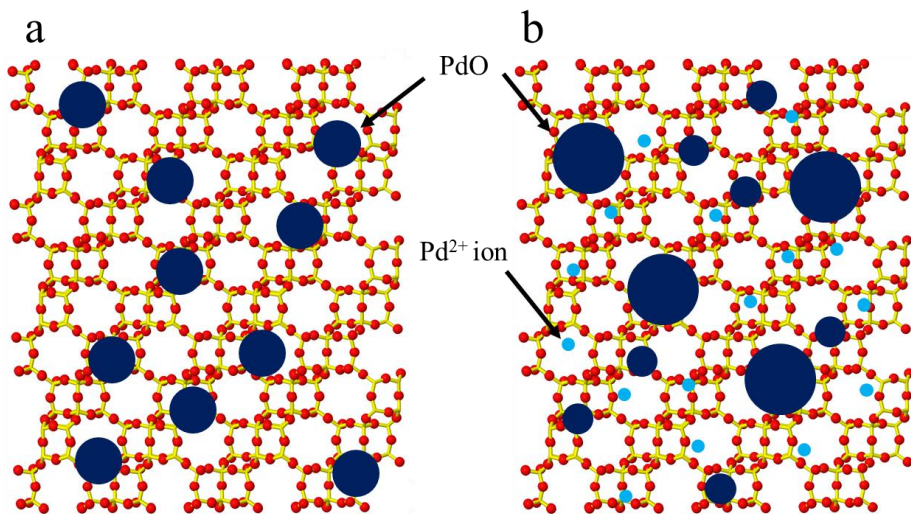


Figure 4-16. Schematic model to represent the change in the nature of Pd (a) before and (b) after HTA treatment.

Summary and Conclusions

Various materials were investigated to evaluate the potential for the cold start NO_x adsorption catalyst. In addition, by applying hydrothermal and sulfur aging conditions, durability of catalyst under real diesel exhaust were studied.

The effect of active metals (Pt and Pd) and supports (CeO₂ and Al₂O₃) on low temperature NO adsorption has been extensively investigated after HTA treatment. From the NO adsorption/desorption test, it is verified that the NO adsorption/desorption properties of catalyst relies considerably on the loaded PGM. In the NO adsorption experiment, Pd/CeO₂ displays two NO_x desorption peaks at 300 and 450 °C, while Pt catalysts such as Pt and Pt-Pd/CeO₂ mainly exhibits high temperature NO_x peak (at 450 °C). In the case of Al₂O₃-based catalyst, only Pd containing catalysts have NO adsorption sites which desorb NO_x at below 200 °C with smaller adsorption capacity than Ce-based catalysts. Based on the DRIFT and NO adsorption/desorption results, it is revealed that the addition of Pd on CeO₂ promotes the oxidation of NO_x species, giving rise to the improvement of the NO adsorption sites which desorb NO and NO₂ at 450 °C. In particular, the interface between Pd and CeO₂ provides new adsorbed site for NO_x species (nitro-nitrito) desorbing NO at around 300 °C. Among the all studied catalysts using CeO₂ and Al₂O₃, Pd/CeO₂ has the largest NO adsorption capacity and desirable desorption temperature.

Next, the effects of sulfur aging (SA) and regeneration on the low temperature NO adsorption over Pd/CeO₂ are extensively investigated. In

addition, for comparison, Pd/Ce_{0.58}Zr_{0.42}O₂ (Ce58) which has high sulfur resistance is also studied. Affinity test (between CeO₂ and SO₂/NO) and SO₂-TPD clearly demonstrate that the strong chemisorption of SO₂ on ceria interrupt the adsorption of NO on Pd/CeO₂ and Pd/Ce58. As a result, the sulfur aging on both catalysts gives rise to the complete deactivation of NO adsorption ability. Textural characterizations and CO-chemisorption results indicate that the structural collapse on Pd/CeO₂ during regeneration leads to the inaccessible Pd species, whereas Pd/Ce58 maintains its structure and recovers Pd dispersion and surface area. However, despite the presence of clear difference in the Pd dispersion and textural properties between two regenerated catalysts, both catalysts show similar partial restoration of NO adsorption ability. Those results are due to the weakness of interaction between PdO and ceria in both Pd/CeO₂ and Pd/Ce58 after sulfur aging and regeneration, as verified by H₂-TPR analysis. To sum up, although the Ce(SO₄)₂ formed during SA treatment is almost removed during regeneration process, the NO adsorption ability of catalysts partially recovers due to the weakened interaction between PdO and CeO₂. Therefore, it can be concluded that the application of Ce-based catalyst to cold start NO adsorption is difficult.

To overcome the deactivation by sulfur, zeolite-based catalyst was employed. It is found that the Pd ion exchange in SSZ-13 is rather difficult with conventional methods, presumably due to the hydrolysis of Pd ion and the small pore structure of SSZ-13. The major state of Pd in fresh catalyst is PdO, on which NO hardly adsorb, resulting in the negligible NO adsorption ability of

fresh catalyst. After HTA treatment at 750 °C for 25 hr, Pd/SSZ-13 has the improved NO adsorption ability. Furthermore, SA aging on HTA Pd/SSZ-13 leads to the negligible activity change in NO adsorption ability. Such HTA catalysts exhibit two NO desorption features at around 250 and 400 °C, which is suitable for the cold start application. XRD patterns show the unchanged zeolite structure during HTA, indicating the hydrothermal stability of Pd/SSZ-13. On the other hand, H₂-TPR and XAFS results clearly demonstrate that the HTA treatment induced the transformation of bulk PdO into Pd²⁺ ion in SSZ-13. Moreover, DRIFT spectra also show the presence of two kinds of ionic Pd-NO species in HTA Pd/SSZ-13 after NO adsorption. In summary, HTA treatment on Pd/SSZ-13 provides the mobility of PdO leading to the redistribution to generate the Pd²⁺ ion species in SSZ-13 zeolite, which play as an active site for NO adsorption at low temperature. In conclusion, since HTA Pd/SSZ-13 has high hydrothermal stability and sulfur resistance in addition to catalytic activity, it can be mentioned that it has a potential for the cold start NO_x adsorption catalyst.

Bibliography

- [1] A. Russell and W. S. Epling; *Catalysis Reviews-Science and Engineering*, *53*, (2011), *337*.
- [2] F. A. Amanda Sauer; *journal*, (2004),
- [3] P. G. Chen and J. M. Wang; *Journal of Dynamic Systems Measurement and Control-Transactions of the Asme*, *134*, (2012),
- [4] S. R. Katare, J. E. Patterson and P. M. Laing; *Industrial & Engineering Chemistry Research*, *46*, (2007), *2445*.
- [5] G. Corro; *Reaction Kinetics and Catalysis Letters*, *75*, (2002), *89*.
- [6] L. Guzzella and A. Amstutz; *Ieee Control Systems Magazine*, *18*, (1998), *53*.
- [7] M. Zheng, G. T. Reader and J. G. Hawley; *Energy Conversion and Management*, *45*, (2004), *883*.
- [8] T. V. Johnson; *International Journal of Engine Research*, *10*, (2009), *275*.
- [9] S. S. Gill, J. M. Herreros, A. Tsolakis, D. M. Turner, E. Miller and A. P. E. York; *Rsc Advances*, *2*, (2012), *10400*.
- [10] F. J. P. Schott, S. Steigert, S. Zuercher, M. Endisch and S. Kureti; *Chemical Engineering and Processing*, *62*, (2012), *54*.
- [11] J. Y. Chin, S. A. Batterman, W. F. Northrop, S. V. Bohac and D. N. Assanis; *Energy & Fuels*, *26*, (2012), *6737*.
- [12] P. I. Jalava, P. Aakko-Saksa, T. Murtonen, M. S. Happonen, A. Markkanen, P. Yli-Pirila, P. Hakulinen, R. Hillamo, J. Maki-Paakkanen, R. O. Salonen, J. Jokiniemi and M. R. Hirvonen; *Particle and Fibre Toxicology*, *9*, (2012),
- [13] L. Lizarraga, S. Souentie, A. Boreave, C. George, B. D'Anna and P. Vernoux; *Environmental Science and Technology*, *45*, (2011), *10591*.
- [14] P. Geng, C. D. Yao, L. J. Wei, J. H. Liu, Q. G. Wang, W. Pan and J. Y. Wang; *Fuel*, *123*, (2014), *1*.
- [15] G. A. Westphal, J. Krahl, A. Munack, Y. Rusche, O. Schroder, E. Hallier, T. Bruning and J. Bunger; *Environmental Science and Technology*, *46*, (2012), *6417*.
- [16] M. R. Ward, T. Hyde, E. D. Boyes and P. L. Gai; *Chemcatchem*, *4*, (2012),

1622.

- [17] T. V. Johnson; journal,
- [18] I. Lefort, J. M. Herreros and A. Tsolakis; *Environmental Science and Technology*, *48*, (2014), *2361*.
- [19] L. Zhu, C. S. Cheung, W. G. Zhang, J. H. Fang and Z. Huang; *Fuel*, *113*, (2013), *690*.
- [20] P. G. Chen and J. M. Wang; *Journal of the Franklin Institute-Engineering and Applied Mathematics*, *350*, (2013), *1992*.
- [21] P. Rounce, A. Tsolakis and A. P. E. York; *Fuel*, *96*, (2012), *90*.
- [22] D. Bounechada, G. Groppi, P. Forzatti, K. Kallinen and T. Kinnunen; *Topics in Catalysis*, *56*, (2013), *372*.
- [23] Q. Y. Wang, B. Zhao, G. F. Li and R. X. Zhou; *Environmental Science and Technology*, *44*, (2010), *3870*.
- [24] E. P. Brandt, Y. Y. Wang and J. W. Grizzle; *Ieee Transactions on Control Systems Technology*, *8*, (2000), *767*.
- [25] R. M. Heck and R. J. Farrauto; *Applied Catalysis a-General*, *221*, (2001), *443*.
- [26] D. K. Zhang, Y. Ma and M. M. Zhu; *Proceedings of the Combustion Institute*, *34*, (2013), *1869*.
- [27] P. G. Chen and J. M. Wang; *Control Engineering Practice*, *22*, (2014), *81*.
- [28] S. F. Ye, Y. H. Yap, S. T. Kolaczkowski, K. Robinson and D. Lukyanov; *Chemical Engineering Research and Design*, *90*, (2012), *834*.
- [29] S. Kolaczkowski, S. Ye, Y. Yap, K. Robinson and D. Lukyanov; *Catalysis Today*, *188*, (2012), *53*.
- [30] J. Kim, C. Kim and S. J. Choung; *Catalysis Today*, *185*, (2012), *296*.
- [31] S. Raux, A. Frobert and E. Jeudy; *Topics in Catalysis*, *52*, (2009), *1903*.
- [32] M. V. Twigg; *Catalysis Today*, *117*, (2006), *407*.
- [33] A. Morlang, U. Neuhausen, K. V. Klementiev, F. W. Schutze, G. Miehe, H. Fuess and E. S. Lox; *Applied Catalysis B-Environmental*, *60*, (2005), *191*.
- [34] M. Kaneeda, H. Iizuka, T. Hiratsuka, N. Shinotsuka and M. Arai; *Applied Catalysis B-Environmental*, *90*, (2009), *564*.
- [35] P. Gelin, L. Urfels, M. Primet and E. Tena; *Catalysis Today*, *83*, (2003),

45.

- [36] M. Chen and L. D. Schmidt; *Journal of Catalysis*, *56*, (1979), *198*.
- [37] A. M. Venezia, L. F. Liotta, G. Pantaleo, V. La Parola, G. Deganello, A. Beck, Z. Koppány, K. Frey, D. Horvath and L. Guzzi; *Applied Catalysis a-General*, *251*, (2003), *359*.
- [38] B. Maik, U. Kirchner, R. Vogt and T. Benter; *Atmospheric Environment*, *43*, (2009), *1908*.
- [39] S. Youn, S. Jeong and D. H. Kim; *Catalysis Today*, *232*, (2014), *185*.
- [40] I. Song, S. Youn, H. Lee, S. G. Lee, S. J. Cho and D. H. Kim; *Applied Catalysis B-Environmental*, *210*, (2017), *421*.
- [41] J. H. Kwak, R. G. Tonkyn, D. H. Kim, J. Szanyi and C. H. F. Peden; *Journal of Catalysis*, *275*, (2010), *187*.
- [42] F. Gao, Y. L. Wang, N. M. Washton, M. Kollar, J. Szanyi and C. H. F. Peden; *Acs Catalysis*, *5*, (2015), *6780*.
- [43] <https://www.deere.com/en_US/services_and_support/engine-information/understanding-emission-regulations/understanding-emission-regulations.page>
- [44] H. Chen, S. Mulla, E. Weigert, K. Camm, T. Ballinger, J. Cox and P. Blakeman; *SAE Int. J. Fuels Lubr.*, *6*, (2013), *372*.
- [45] Y. Y. Ji, S. L. Bai and M. Crocker; *Applied Catalysis B-Environmental*, *170*, (2015), *283*.
- [46] S. Jones, Y. Y. Ji and M. Crocker; *Catalysis Letters*, *146*, (2016), *909*.
- [47] T. M. Yuichiro Murata, Katsuji Wada, Hiroshi Ohno; *SAE Int. J. Fuels Lubr.*, *8*, (2015), *454*.
- [48] J. R. Theis; *Catalysis Today*, *267*, (2016), *93*.
- [49] H.-Y. Chen, J. E. Collier, D. Liu, L. Mantarosie, D. Durán-Martín, V. Novák, R. R. Rajaram and D. Thompsett; *Catalysis Letters*, (2016), *1*.
- [50] H. Chen and S. Mulla; *journal*, (2012),
- [51] F. Mckenna; *journal*, (2014),
- [52] R. Rajaram, F. Mckenna, H. Chen and D. Liu; *journal*,
- [53] J. a. J. McDonald, L; *SAE Technical Paper*, *1*, (2000), *1957*.
- [54] M. P. Gonzalez-Marcos, B. Pereda, U. De La Torre and J. R. Gonzalez-Velasco; *Topics in Catalysis*, *56*, (2013), *352*.

- [55] M. Khosravi, C. Sola, A. Abedi, R. E. Hayes, W. S. Epling and M. Votsmeier; *Applied Catalysis B-Environmental*, *147*, (2014), *264*.
- [56] V. Rico-Perez, A. Bueno-Lopez, D. J. Kim, Y. Y. Ji and M. Crocker; *Applied Catalysis B-Environmental*, *163*, (2015), *313*.
- [57] M. A. Hoque and K. Kim; *Korean Journal of Chemical Engineering*, *31*, (2014), *1316*.
- [58] R. F. Vanslooten and B. E. Nieuwenhuys; *Journal of Catalysis*, *122*, (1990), *429*.
- [59] C. Descorme, P. Gelin, M. Primet and C. Lecuyer; *Catalysis Letters*, *41*, (1996), *133*.
- [60] K. I. Hadjiivanov; *Catalysis Reviews-Science and Engineering*, *42*, (2000), *71*.
- [61] J. M. Watson and U. S. Ozkan; *Journal of Catalysis*, *210*, (2002), *295*.
- [62] M. Ogura, M. Hayashi, S. Kage, M. Matsukata and E. Kikuchi; *Applied Catalysis B-Environmental*, *23*, (1999), *247*.
- [63] A. S. Ivanova, E. M. Slavinskaya, R. V. Gulyaev, V. I. Zaikovskii, O. A. Stonkus, I. G. Danilova, L. M. Plyasova, I. A. Polukhina and A. I. Boronin; *Applied Catalysis B-Environmental*, *97*, (2010), *57*.
- [64] H. Lee, D. H. Lee, Y. H. Song, W. C. Choi, Y. K. Park and D. H. Kim; *Chem. Eng. J.*, *259*, (2015), *761*.
- [65] J. E. Park, B. B. Kim and E. D. Park; *Korean Journal of Chemical Engineering*, *32*, (2015), *2212*.
- [66] A. Trovarelli; *Catalysis Reviews-Science and Engineering*, *38*, (1996), *439*.
- [67] M. Boaro, C. de Leitenburg, G. Dolcetti and A. Trovarelli; *Journal of Catalysis*, *193*, (2000), *338*.
- [68] Y. Ryou, J. Lee, H. Lee, J. W. Chung, S. Yoo and D. H. Kim; *Catalysis Today*, *258*, (2015), *518*.
- [69] S. Philipp, A. Drochner, J. Kunert, H. Vogel, J. Theis and E. S. Lox; *Topics in Catalysis*, *30-1*, (2004), *235*.
- [70] B. Azambre, L. Zenboury, F. Delacroix and J. V. Weber; *Catalysis Today*, *137*, (2008), *278*.
- [71] Z. Say, E. I. Vovk, V. I. Bukhtiyarov and E. Ozensoy; *Applied Catalysis*

B-Environmental, *142*, (2013), *89*.

[72] K. J. Lee, P. A. Kumar, M. S. Maqbool, K. N. Rao, K. H. Song and H. P. Ha; Applied Catalysis B-Environmental, *142*, (2013), *705*.

[73] Z. R. Ma, D. Weng, X. D. Wu, Z. C. Si and B. Wang; Catalysis Communications, *27*, (2012), *97*.

[74] S. E. Wanke and P. C. Flynn; Catalysis Reviews-Science and Engineering, *12*, (1975), *92*.

[75] N. Radic, B. Grbic and A. Terlecki-Baricevic; Applied Catalysis B-Environmental, *50*, (2004), *153*.

[76] I. Atribak, B. Azambre, A. B. Lopez and A. Garcia-Garcia; Applied Catalysis B-Environmental, *92*, (2009), *126*.

[77] Y. Nagai, T. Hirabayashi, K. Dohmae, N. Takagi, T. Minami, H. Shinjoh and S. Matsumoto; Journal of Catalysis, *242*, (2006), *103*.

[78] G. W. Graham, H. W. Jen, O. Ezekoye, R. J. Kudla, W. Chun, X. Q. Pan and R. W. McCabe; Catalysis Letters, *116*, (2007), *1*.

[79] H. H. Kan, R. J. Colmyer, A. Asthagiri and J. F. Weaver; Journal of Physical Chemistry C, *113*, (2009), *1495*.

[80] D. R. Mullins, P. M. Albrecht, T. L. Chen, F. C. Calaza, M. D. Biegalski, H. M. Christen and S. H. Overbury; Journal of Physical Chemistry C, *116*, (2012), *19419*.

[81] J. A. Hinojosa, A. Antony, C. Hakanoglu, A. Asthagiri and J. F. Weaver; Journal of Physical Chemistry C, *116*, (2012), *3007*.

[82] P. M. Albrecht, D. E. Jiang and D. R. Mullins; Journal of Physical Chemistry C, *118*, (2014), *9042*.

[83] A. Martinezarias, J. Soria, J. C. Conesa, X. L. Seoane, A. Arcoya and R. Cataluna; Journal of the Chemical Society-Faraday Transactions, *91*, (1995), *1679*.

[84] B. Azambre, L. Zenboury, A. Koch and J. V. Weber; Journal of Physical Chemistry C, *113*, (2009), *13287*.

[85] Y. D. Cao, R. Ran, X. D. Wu and D. Weng; Applied Catalysis a-General, *501*, (2015), *17*.

[86] J. Y. Luo, W. S. Epling, G. S. Qi and W. Li; Catalysis Letters, *142*, (2012), *946*.

- [87] Y. Y. Ji, T. J. Toops, U. M. Graham, G. Jacobs and M. Crocker; *Catalysis Letters*, *110*, (2006), *29*.
- [88] A. M. Hernandez-Gimenez, D. Lozano-Castello and A. Bueno-Lopez; *Applied Catalysis B-Environmental*, *148*, (2014), *406*.
- [89] T. Kolli, T. Kanerva, P. Lappalainen, M. Huuhtanen, M. Vippola, T. Kinnunen, K. Kallinen, T. Lepisto, J. Lahtinen and R. L. Keiski; *Topics in Catalysis*, *52*, (2009), *2025*.
- [90] M. Boaro, C. de Leitenburg, G. Dolcetti, A. Trovarelli and M. Graziani; *Topics in Catalysis*, *16*, (2001), *299*.
- [91] G. Liu, J. A. Rodriguez, Z. P. Chang, J. Hrbek and C. H. F. Peden; *Journal of Physical Chemistry B*, *108*, (2004), *2931*.
- [92] T. Luo and R. J. Gorte; *Applied Catalysis B-Environmental*, *53*, (2004), *77*.
- [93] M. Monai, T. Montini, M. Melchionna, T. Duchon, P. Kus, C. Chen, N. Tsud, L. Nasi, K. C. Prince, K. Veltruska, V. Matolin, M. M. Khader, R. J. Gorte and P. Fornasiero; *Applied Catalysis B-Environmental*, *202*, (2017), *72*.
- [94] P. Bazin, O. Saur, F. C. Meunier, M. Daturi, J. C. Lavalley, A. M. Le Govic, V. Harle and G. Blanchard; *Applied Catalysis B-Environmental*, *90*, (2009), *368*.
- [95] A. Holmgren and B. Andersson; *Journal of Catalysis*, *178*, (1998), *14*.
- [96] A. Holmgren, B. Andersson and D. Duprez; *Applied Catalysis B-Environmental*, *22*, (1999), *215*.
- [97] T. Tanabe, Y. Nagai, T. Hirabayashi, N. Takagi, K. Dohmae, N. Takahashi, S. Matsumoto, H. Shinjoh, J. N. Kondo, J. C. Schouten and H. H. Brongersma; *Applied Catalysis a-General*, *370*, (2009), *108*.
- [98] Y. Ryou, J. Lee, H. Lee, C. H. Kim and D. H. Kim; *Catalysis Today*, *307*, (2018), *93*.
- [99] J. A. Rodriguez, T. Jirsak, A. Freitag, J. C. Hanson, J. Z. Larese and S. Chaturvedi; *Catalysis Letters*, *62*, (1999), *113*.
- [100] H. M. Yang, G. X. Wei, X. Q. Wang, F. Lin, J. Wang and M. Q. Shen; *Catalysis Communications*, *36*, (2013), *5*.
- [101] M. Waqif, P. Bazin, O. Saur, J. C. Lavalley, G. Blanchard and O. Touret; *Applied Catalysis B-Environmental*, *11*, (1997), *193*.
- [102] S. S. Deshmukh, M. H. Zhang, V. I. Kovalchuk and J. L. d'Itri; *Applied*

Catalysis B-Environmental, *45*, (2003), *135*.

[103] P. Sudarsanam, B. Mallesham, P. S. Reddy, D. Grossmann, W. Grunert and B. M. Reddy; Applied Catalysis B-Environmental, *144*, (2014), *900*.

[104] J. R. Gonzalez-Velasco, M. A. Gutierrez-Ortiz, J. L. Marc, J. A. Botas, M. P. Gonzalez-Marcos and G. Blanchard; Applied Catalysis B-Environmental, *22*, (1999), *167*.

[105] M. Bensitel, O. Saur, J. C. Lavalley and B. A. Morrow; Materials Chemistry and Physics, *19*, (1988), *147*.

[106] H. W. Jen, G. W. Graham, W. Chun, R. W. McCabe, J. P. Cuif, S. E. Deutsch and O. Touret; Catalysis Today, *50*, (1999), *309*.

[107] J. Y. Luo, M. Meng, H. Xian, Y. B. Tu, X. G. Li and T. Ding; Catalysis Letters, *133*, (2009), *328*.

[108] Q. Y. Wang, G. F. Li, B. Zhao, M. Q. Shen and R. X. Zhou; Applied Catalysis B-Environmental, *101*, (2010), *150*.

[109] R. A. Daley, S. Y. Christou, A. M. Efstathiou and J. A. Anderson; Applied Catalysis B-Environmental, *60*, (2005), *117*.

[110] L. F. Chen, G. Gonzalez, J. A. Wang, L. E. Norena, A. Toledo, S. Castillo and M. Moran-Pineda; Applied Surface Science, *243*, (2005), *319*.

[111] H. Q. Zhu, Z. F. Qin, W. J. Shan, W. J. Shen and J. G. Wang; Journal of Catalysis, *225*, (2004), *267*.

[112] G. Balducci, J. Kaspar, P. Fornasiero, M. Graziani and M. S. Islam; Journal of Physical Chemistry B, *102*, (1998), *557*.

[113] P. Fornasiero, G. Balducci, R. DiMonte, J. Kaspar, V. Sergo, G. Gubitosa, A. Ferrero and M. Graziani; Journal of Catalysis, *164*, (1996), *173*.

[114] H. Y. Chen, J. E. Collier, D. X. Liu, L. Mantarosie, D. Duran-Martin, V. Novak, R. R. Rajaram and D. Thompsett; Catalysis Letters, *146*, (2016), *1706*.

[115] Y. Ryou, J. Lee, H. Lee, C. H. Kim and D. H. Kim; Catalysis Today, *297*, (2017), *53*.

[116] G. Koyano, S. Yokoyama and M. Misono; Applied Catalysis a-General, *188*, (1999), *301*.

[117] B. Pommier and P. Gelin; Physical Chemistry Chemical Physics, *3*, (2001), *1138*.

[118] K. Okumura, J. Amano, N. Yasunobu and M. Niwa; Journal of Physical

Chemistry B, *104*, (2000), *1050*.

[119] M. Che, J. F. Dutel, P. Gallezot and M. Primet; *Journal of Physical Chemistry*, *80*, (1976), *2371*.

[120] C. Descorme, P. Gelin, C. Lecuyer and M. Primet; *Journal of Catalysis*, *177*, (1998), *352*.

[121] H. Ohtsuka and T. Tabata; *Applied Catalysis B-Environmental*, *21*, (1999), *133*.

[122] A. Vu, J. Y. Luo, J. H. Li and W. S. Epling; *Catalysis Letters*, *147*, (2017), *745*.

[123] Y. Zheng, L. Kovarik, M. H. Engelhard, Y. Wang, Y. Wang, F. Gao and J. Szanyi; *The Journal of Physical Chemistry C*, *121*, (2017), *15793*.

[124] Y. Ryou, J. Lee, S. J. Cho, H. Lee, C. H. Kim and D. H. Kim; *Applied Catalysis B-Environmental*, *212*, (2017), *140*.

[125] J. Rasko and F. Solymosi; *Journal of the Chemical Society-Faraday Transactions I*, *80*, (1984), *1841*.

[126] K. Chakarova, E. Ivanova, K. Hadjiivanov, D. Klissurski and H. Knozinger; *Physical Chemistry Chemical Physics*, *6*, (2004), *3702*.

[127] B. J. Adelman and W. M. H. Sachtler; *Applied Catalysis B-Environmental*, *14*, (1997), *1*.

[128] S. B. C. Pergher, R. M. Dallago, R. C. Veses, C. E. Gigola and I. M. Baibich; *Journal of Molecular Catalysis a-Chemical*, *209*, (2004), *107*.

[129] H. Matsumoto and S. Tanabe; *Journal of Materials Science Letters*, *11*, (1992), *623*.

[130] C. Stolz, A. Sauvage, P. Massiani and R. Kramer; *Applied Catalysis a-General*, *167*, (1998), *113*.

[131] O. C. Feeley and W. M. H. Sachtler; *Applied Catalysis*, *75*, (1991), *93*.

[132] S. T. Homeyer and W. M. H. Sachtler; *Applied Catalysis*, *54*, (1989), *189*.

[133] F. Lonyi, H. E. Solt, J. Valyon, H. Decolatti, L. B. Gutierrez and E. Miro; *Applied Catalysis B-Environmental*, *100*, (2010), *133*.

[134] K. Shimizu, F. Okada, Y. Nakamura, A. Satsuma and T. Hattori; *Journal of Catalysis*, *195*, (2000), *151*.

[135] Y. Zheng, L. Kovarik, M. H. Engelhard, Y. L. Wang, Y. Wang, F. Gao

- and J. Szanyi; *Journal of Physical Chemistry C*, *121*, (2017), *15793*.
- [136] L. Wang, J. R. Gaudet, W. Li and D. Weng; *Journal of Catalysis*, *306*, (2013), *68*.
- [137] S. Shwan, M. Skoglundh, L. F. Lundegaard, R. R. Tiruvalam, T. V. W. Janssens, A. Carlsson and P. N. R. Vennestrom; *Acs Catalysis*, *5*, (2015), *16*.
- [138] L. Gucci and I. Kiricsi; *Applied Catalysis a-General*, *186*, (1999), *375*.
- [139] L. A. Koroleva, N. D. Shikina, P. G. Kolodina, A. V. Zotov, B. R. Tagirov, Y. V. Shvarov, V. A. Volchenkova and Y. K. Shazzo; *Geochemistry International*, *50*, (2012), *853*.
- [140] C. F. Baes; *journal*, (1986), *264*.
- [141] L. Becker and H. Forster; *Applied Catalysis B-Environmental*, *17*, (1998), *43*.
- [142] Z. Karpinski, S. N. Gandhi and W. M. H. Sachtler; *Journal of Catalysis*, *141*, (1993), *337*.
- [143] P. Gallezot; *Catalysis Reviews-Science and Engineering*, *20*, (1979), *121*.
- [144] B. Pommier and P. Gelin; *Physical Chemistry Chemical Physics*, *1*, (1999), *1665*.
- [145] Y. J. Kim, J. K. Lee, K. M. Min, S. B. Hong, I. S. Nam and B. K. Cho; *Journal of Catalysis*, *311*, (2014), *447*.
- [146] D. W. Fickel, J. M. Fedeyko and R. F. Lobo; *Journal of Physical Chemistry C*, *114*, (2010), *1633*.
- [147] U. Deka, A. Juhin, E. A. Eilertsen, H. Emerich, M. A. Green, S. T. Korhonen, B. M. Weckhuysen and A. M. Beale; *Journal of Physical Chemistry C*, *116*, (2012), *4809*.
- [148] J. H. Kwak, T. Varga, C. H. F. Peden, F. Gao, J. C. Hanson and J. Szanyi; *Journal of Catalysis*, *314*, (2014), *83*.

국 문 초 록

자동차에서 발생하는 NOx는 인간의 건강과 환경에 악영향을 미치기 때문에 이를 저감하는 것은 중요한 사회적 문제이다. 따라서 NOx 배출을 줄이기 위해 이에 대한 규제가 전 세계적으로 강화되고 있는 추세이다. 이러한 규제를 만족하기 위하여 three-way catalysis (TWC), selective catalytic reduction (SCR), and NOx storage reduction (NSR) 등의 NOx 저감 기술들이 성공적으로 개발되고 적용되어 쓰이고 있다. 그 중 SCR과 NSR은 디젤 엔진에서 NOx배출을 처리하기 위해 사용되고 있다. 하지만 이 두 시스템이 적절한 NOx 저감 효율을 얻기 위해선 고온 (200 ° C 이상)이 필요하기 때문에 이보다 낮은 온도 즉 냉시동 구간에서 발생하는 NOx를 제거하기 위한 연구가 진행되고 있다. 최근 냉시동 구간에서 발생하는 NOx를 제어하기 위해 저온에서 NO를 흡장 할 수 있는 촉매 흔히 cold start catalysts (CSC) or passive NOx adsorbers (PNA)가 많은 관심을 받고 있다. 이 촉매의 기능은 저온에서 (냉시동 구간) NO를 흡장하여 SCR이나 NSR이 적절히 작동할 수 있는 고온에서 탈착하는 것이다. 저온 NO 흡장 촉매가 적절한 기능을 하기 위해서는 높은 NO 저장 능력과 적절한 NOx 탈착 온도 같은 촉매 기능뿐만 아니라 디젤 배기 조건에 대한 내구성도 가져야한다. 이 연구에서는 PGM등의 활성 금속과 금속산화물 및 제올라이트 같은 물질을 조합하여 다양한 물질들의 저온 NO흡장 촉매 가능성을 확인하였다. 특히 촉매의 실용화 가능성을 평가하기 위해 촉매 비활성화를 일으키는 열수 노화 및 황 노화 같은 디젤 배기가스 조건이 적용 되었다.

처음에 수열 처리된 Pd/CeO₂를 저온 NO흡장 촉매로 사용하였다. 비교를 위하여 Pt 및 Pt-Pd가 담지된 CeO₂ 및 Al₂O₃촉매도 평가 되

었다. 소열 노화된 촉매의 분석은 CeO_2 가 Al_2O_3 보다 담지 금속의 소결을 방지하는데 높은 효과가 있음을 보여주었다. NO흡착/탈착 결과는 CeO_2 기반 촉매가 Al_2O_3 기반 촉매보다 우수한 NO 흡착 능력을 가지고 있음을 나타내었다. 또한 PGM/ CeO_2 촉매는 냉시동 적용을 위한 바람직한 NO_x 탈착온도를 나타내었다. NO 흡착/탈착 동안 분석한 DRIFT분석결과를 통해 Pd/ CeO_2 에서 관찰된 250, 300, 그리고 450 ° C에서 발생한 NO_x 탈착 피크 각각 촉매에 흡착한 아질산, 니트로 니트리토, 및 질산 종임을 확인할 수 있었다. 촉매의 활성 결과와 특성 분석을 통해 Pd와 CeO_2 의 상호작용으로 인해 촉매의 추가 NO흡착 사이트를 생성하고 흡착된 아질산 종을 질산으로 산화하는데 중요한 역할을 하는 것을 알 수 있었다. 따라서, Pd / CeO_2 는 냉시동 적용을 위한 저온 NO 흡착 촉매로서 좋은 후보가 될 수 있다.

다음으로 촉매의 NO흡착 능력과 물리 화학적 특성 변화를 연구하기 위해 Pd/ CeO_2 와 Pd/ $\text{Ce}_{0.58}\text{Zr}_{0.42}\text{O}_2$ (Pd/Ce58)촉매에 황 노화와 재생 처리를 적용하였다. 황 노화 후 두 촉매에서는 흡착된 NO_x 종보다 열역학적으로 더 안정한 $\text{Ce}(\text{SO}_4)_2$ 가 형성 되어 NO흡착 능력이 거의 완전히 사라졌다. 재생 처리 후 Pd/Ce58는 비슷한 세공 크기를 유지하며 담체의 소결이 일어나지 않고 Pd의 분산이 회복되는 반면 Pd/ CeO_2 는 그렇지 않았다. 그러나 재생 과정 이후에 두 촉매 모두 예전 수준 까지 NO흡착 능력을 회복하지 못한다는 사실은 구조적 특성과 Pd분산으로 NO흡착 능력 감소를 설명할 수 없다는 것을 의미한다. 대신, 두 샘플에 대한 H_2 -TPR 분석은 PdO와 CeO_2 의 동시 환원피크의 사라짐을 통해 Pd와 CeO_2 의 상호작용(interaction)이 줄어들었음을 보였다. 따라서 황 노화와 재생은 Ce 기반 촉매의 NO흡착 능력을 비가역적으로 감소시킨다는 결론을 내릴 수 있다. 이 결과는

Ce기반 촉매가 실용화가 어렵다는 것을 의미한다.

수열 안정성과 내황성을 지닌 촉매를 얻기 위해 제올라이트 기반 담체를 적용하여 촉매를 개발하였다. Fresh Pd/SSZ-13의 경우 제조 방법에 관계없이 우수한 NO흡장 능력을 갖지 못했다. 하지만 수열 노화 (HTA) 처리 후 Pd/SSZ-13은 냉시동 촉매에 적합한 향상된 NO 흡장 능력을 얻을 수 있었다. H₂-TPR 및 XAFS 결과를 통하여 fresh 촉매의 경우 PdO가 주로 존재하고 HTA 처리된 시료의 경우 Pd ion 이 형성 됨을 알 수 있었으며, 이를 통해 HTA처리가 PdO를 Pd ion 으로 재분산 시킴을 확인 할 수 있었다. DRIFT결과는 Pd²⁺ 이온에 흡착된 두 가지 니트로실 복합체 형성을 보이며, 이 두가지 복합체는 HTA Pd/SSZ-13에서 나타난 250 및 400 °C 두가지 탈착 피크와 직접적으로 관련됨을 확인 할 수 있었다. 모든 결과를 종합해본 결과 HTA에 의해 Pd ion의 형성됨을 확인 할 수 있었으며, 이는 저온 NO흡장에 활성점으로 작용한다고 결론 내릴 수 있다.

주요어 : 저온 NO 흡장, 팔라듐, 세리아, SSZ-13, 수열 노화,

황 노화, 냉시동

학 번 : 2014-31091